

Application of Reactive Fluid Transport Modeling to Hydrothermal Systems

Dissertation
zur Erlangung des Grades
Doktor der Naturwissenschaften

am Fachbereich Geowissenschaften
der Johannes Gutenberg-Universität Mainz

NISHANTHA ATTANAYAKE
geboren am 23.08.1967 in Kandy, Sri Lanka

Mainz, 2005

All views and results presented in this thesis are those of the author, unless stated otherwise.

Ich versichere, daß die vorliegende Arbeit selbständig und nur unter Verwendung der angegebenen Quellen und Hilfsmittel verfaßt habe.

Mainz, den 21. Januar 2005

Tag der mündlichen Prüfung: 4. 2. 2005

Zusammenfassung

Zur Untersuchung verschiedener Wechselwirkungssysteme von Fluid und Gestein wurde ein eindimensionaler Transportalgorithmus für reaktive Fluide mehrerer Komponenten, 1DREACT (Steeffel, 1993), benutzt. Eine große Schwachstelle bei Berechnungen des Massentransports, der die Reaktionen von Mineralen berücksichtigt, ist die nicht adäquate Behandlung von festen Lösungen, wie sie in vielen Mineralen vorkommen. Da viele thermodynamische Modelle fester Lösungen hoch nichtlinear sind, kann sich dies ernsthaft auf die Stabilität und Effizienz von Lösungsalgorithmen auswirken. Um die Leistung und Zuverlässigkeit der Algorithmen zu verbessern, wurden Pseudokomponenten bei Berechnungen des Phasengleichgewichts benutzt. Der gleiche Ansatz wird auch hier vorerst verwandt und am Beispiel der komplexen festen Lösungen von Plagioklas dargestellt. Mit ideal molekularen, Al-vermeidenden und nichtidealen Mischungsmodellen wurden thermodynamische Eigenschaften einer variierenden Anzahl von Plagioklas-Zwischenphasen berechnet. Diese unterschiedlichen Mischungsmodelle können ohne Modifikation des Transportcodes leicht in Simulationen eingebaut werden. Simulationsergebnisse zeigen, dass schon neun Zwischenverbindungen ausreichen, um das Diffusionsprofil von Albit nach Anorthit zu charakterisieren. Somit ist diese Näherung sehr effizient und kann mit geringem Aufwand eingesetzt werden.

In einem weiteren Kapitel wird über die Ergebnisse der Modellierung des reaktiven Fluidtransportes berichtet, die zur Beschränkung der hydrothermalen Alteration Paläozoischer Sedimente in der Region des südlichen Oberer Sees entworfen wurden. Feldbeobachtungen zeigen offensichtlich, dass aufgrund der Aktivität von Fluiden, die in permeablen Fließkanälen migrieren, Quarz-Pyrophyllit (oder Kaolinit) enthaltende Verbindungen in Zusammensetzungen mit Muskovit-Pyrophyllit-Diaspor umgewandelt wurden. Die Modellierung von Fluid-Gesteinswechselwirkung mit einer initialen Qtz-PrL Verbindung und einem K-reichen Fluid simuliert die Bildung einer mineralogischen Umwandlung, wie sie beobachtet wird. Die Gesamtzusammensetzung des Systems entwickelt sich von einer SiO₂-reichen zu einer Al₂O₃+K₂O-reichen. Simulationen zeigen, dass der Fluidfluss steigenden Temperaturen folgt und dass das Fluid K-reich war.

Der Ansatz mittels Pseudoverbindungen feste Lösungen in reaktive Transportmodellen einzubeziehen, wurde durch Modellierung hydrothermalen Alteration von isländischen Basalten überprüft. Feste Lösungen von Chloriden, Amphibolen und Plagioklasen wurden als sekundäre Mineralphasen einbezogen. Um die Wirkung des Salzgehalts auf die Alteration zu untersuchen, wurden saline und Frischwasser-Zusammensetzungen

geothermaler Fluide benutzt. Simulationen der Fluid-Gesteinswechselwirkung erzeugen die beobachteten Mineralumwandlungen. In Übereinstimmung mit Feldbeobachtungen zeigen sie, dass durch die Reaktionen mit beiden Fluidtypen grob die gleichen Alterationsminerale gebildet werden.

Zum Schluss wird die Modellierung auf die Sanierung von nitratreichem Grundwasser angewandt. Mit dem reaktiven Fluidtransport-Algorithmus wurde die Beseitigung von überschüssigem Nitrat aus dem Grundwasser durch Pyritoxidation modelliert. Die meisten Modellergebnisse zeigen, dass die Nitratkonzentration im infiltrierenden Wasser signifikant erniedrigt werden kann, wenn ein pyrithaltiger, permeabler Bereich unterhalb der Fließwege platziert wird. Dies ist in guter Übereinstimmung mit Vorschlägen aus der Literatur und auf die Reduktion von Stickstoff zurückzuführen. Einige Simulationen untersuchen die Wirksamkeit von Systemen mit unterschiedlichen mineralisch reaktiven Oberflächenbereichen, reaktiven Grenzsichtdicken und Fließraten, um den optimalen Aufbau zu identifizieren.

ABSTRACT

A one-dimensional multi-component reactive fluid transport algorithm, 1DREACT (Steeffel, 1993) was used to investigate different fluid-rock interaction systems. A major short coming of mass transport calculations which include mineral reactions is that solid solutions occurring in many minerals are not treated adequately. Since many thermodynamic models of solid solutions are highly non-linear, this can seriously impact on the stability and efficiency of the solution algorithms used. Phase petrology community saw itself faced with a similar predicament 10 years ago. To improve performance and reliability, phase equilibrium calculations have been using pseudo compounds. The same approach is used here in the first, using the complex plagioclase solid solution as an example. Thermodynamic properties of a varying number of intermediate plagioclase phases were calculated using ideal molecular, Al-avoidance, and non-ideal mixing models. These different mixing models can easily be incorporated into the simulations without modification of the transport code. Simulation results show that as few as nine intermediate compositions are sufficient to characterize the diffusional profile between albite and anorthite. Hence this approach is very efficient, and can be used with little effort.

A subsequent chapter reports the results of reactive fluid transport modeling designed to constrain the hydrothermal alteration of Paleoproterozoic sediments of the Southern Lake Superior region. Field observations reveal that quartz-pyrophyllite (or kaolinite) bearing assemblages have been transformed into muscovite-pyrophyllite-diaspore bearing assemblages due to action of fluids migrating along permeable flow channels. Fluid-rock interaction modeling with an initial qtz-prl assemblage and a K-rich fluid simulates the formation of observed mineralogical transformation. The bulk composition of the system evolves from an SiO₂-rich one to an Al₂O₃+K₂O-rich one. Simulations show that the fluid flow was up-temperature (e.g. recharge) and that fluid was K-rich.

Pseudo compound approach to include solid solutions in reactive transport models was tested in modeling hydrothermal alteration of Icelandic basalts. Solid solutions of chlorites, amphiboles and plagioclase were included as the secondary mineral phases. Saline and fresh water compositions of geothermal fluids were used to investigate the effect of salinity on alteration. Fluid-rock interaction simulations produce the observed mineral transformations. They show that roughly the same alteration minerals are formed due to reactions with both types of fluid which is in agreement with the field observations.

A final application is directed towards the remediation of nitrate rich groundwaters. Removal of excess nitrate from groundwater by pyrite oxidation was modeled using the reactive fluid transport algorithm. Model results show that, when a pyrite-bearing, permeable zone is placed in the flow path, nitrate concentration in infiltrating water can be significantly lowered, in agreement with proposals from the literature. This is due to nitrogen reduction. Several simulations investigate the efficiency of systems with different mineral reactive surface areas, reactive barrier zone widths, and flow rates to identify the optimum setup.

CONTENT

Zusammenfassung

Abstract

CHAPTER 1. Introduction

1.1 Fluid-rock interaction systems	1
1.2 Modeling the processes	2
1.3 Outline of the thesis	3

CHAPTER 2. Approaches in reactive transport modeling

2.1 Introduction	5
2.2 Reactions in geochemical systems	5
2.2.1 Homogeneous reactions in the aqueous phase	6
2.2.2 Heterogeneous reactions between fluid and minerals	7
2.2.3 Mass balance	8
2.2.4 Electroneutrality	8
2.3 Fluid flow and transport of solutes	9
2.4 Numerical method	10
2.5 Speciation calculation	12
2.6 Thermodynamic database	13

CHAPTER 3. Using pseudo compounds to model solid solutions in reactive fluid transport models

Abstract	17
3.1 Introduction	18
3.2 Pseudo compounds	18
3.3 Mixing models for plagioclase	19
3.4 Thermodynamic databases	21
3.5 Reactive fluid flow	25
3.6 The test case	25
3.7 Results and discussion	27
3.8 Conclusion	36

CHAPTER 4. Reactive fluid transport modeling of metasomatism of Late Paleoproterozoic sedimentary rocks in the Southern Lake Superior region

Abstract	39
4.1 Introduction	39
4.2 Geological setting	40

4.3	Reactive fluid transport modeling	42
4.4	Results and discussion	51
4.5	Conclusion	59
CHAPTER 5. Modeling hydrothermal alteration of basalts in high-temperature geothermal systems in Iceland		
	Abstract	62
5.1	Introduction	62
5.2	Icelandic geothermal systems and their hydrothermal alteration	63
5.3	Reactive fluid transport modeling	65
5.4	Solid solutions in reactive flow models	66
5.5	Model parameters	67
5.6	Results and discussion	72
5.7	Conclusion	80
CHAPTER 6. Application of reactive fluid transport modeling to groundwater contaminant treatment: Excess nitrate removal by pyrite oxidation		
	Abstract	83
6.1	Introduction	83
6.2	Reactive fluid transport modeling	85
6.3	Model parameters	85
6.4	Results and discussion	87
6.5	Conclusion	92

CHAPTER 1

Introduction

1.1 Fluid-rock interaction systems

The intense chemical and physical interaction of rock and water in the uppermost regions of the earth's crust has strong influence on its composition and evolution. Homogeneous reactions among aqueous species and heterogeneous reactions between aqueous and solid phases cause new minerals to precipitate, existing minerals to dissolve or to transform into other minerals. Dissolution of the minerals results in progressive weakening of the rock matrix leading to ductile or brittle deformation depending on the rheological properties of the rock. Similarly, mineral precipitation obstructs flow paths in the porous medium increasing the fluid pressure which at a certain point overcomes the lithostatic pressure resulting in fracturing of the rock. These processes modify the porosity and permeability of rocks which in turn affect the flow patterns. A number of factors govern these complex processes among which temperature, pressure, fluid composition, and rheological properties of the rock are the most significant. Redox state of the system is also an important parameter affecting the chemical reactions. Aqueous fluids are highly reactive at high temperatures, reaction rates are fast, and hence porosity changes will be rapid. Equilibrium among reacting phases is achieved within a comparatively short time period. On the contrary chemical interaction between fluid and rock at low temperatures are generally slow and the time span of such processes to reach equilibrium could be of several orders of magnitude higher than as it would be under high temperature conditions. However the rate of fluid flow has a greater influence on the heterogeneous reaction kinetics. In a system where reaction rates are faster than solute transport rates, equilibrium among phases is achieved whereas when higher flow rates exceed reaction rates, equilibrium between solute and mineral phases is restrained.

Weathering, diagenesis, metasomatism, metamorphism and hydrothermal alteration are the major fluid-rock interaction systems of geological interest. A better understanding of fluid-rock interactions both at microscopic and crustal scales can be obtained when they are accurately modeled in time and space. Of numerous fluid-rock interaction systems, hydrothermal environments are a significant category due to its relevance to ore formation, geothermal energy and crustal evolution. Extensive experimental works carried out in the past few decades to determine thermodynamic properties of materials of geologic significance for a wide range of pressures and temperatures have yielded a vast collection of data that enables modeling hydrothermal systems. In this work reactive fluid transport modeling will be applied to characterize different hydrothermal settings using a one-dimensional multi-component reactive fluid transport code, 1DREACT (Steeffel, 1993). In addition, reactive transport modeling has been applied to model groundwater contaminant removal taking nitrate as an example. Rationale of each test case is briefly given in section 1.3.

1.2 Modeling the processes

In order to merge and understand the different geophysical, petrological and geochemical processes taking place during fluid-rock interaction, transport and reaction of elements and fluid flow are coupled in models. Quantifying fluid-rock interaction and fluid flow has been a widely addressed research area for last three decades due to its importance in understanding many natural phenomena such as weathering, ore deposit formation, diagenetic processes, metamorphism, metasomatic and hydrothermal alteration. In addition to these natural processes a new line of research has focused on fluid-rock interactions induced by anthropogenic activities such as installation of subsurface nuclear waste repositories and solid waste disposal sites. Contaminant transport and groundwater quality have been extensively studied using reactive fluid transport models especially for predictive modeling and remediation.

Quantitative models of fluid circulation and mineral-fluid reactions require that the coupled partial differential equations of element transport (mass conservation equations) are solved simultaneously with the partial differential equations governing fluid flow. The mass conservation equations are linked to each other through the homogeneous reactions occurring in the fluid phase as well as the heterogeneous reactions between fluid and rock. Flow of the fluid phase, a viscous and possibly compressible liquid, is driven by pressure and/or temperature gradients or caused by deformation of the matrix, and follows the Darcy's Law. The processes taking place in natural geochemical systems are numerous and varied, and hence devising simple straight forward models to describe the interaction between fluid and rock coupled with mass transport becomes a difficult task. Due to the complex nature of the fluid-rock interaction systems, finding analytical solutions for the systems of equations that describe the processes becomes tedious and unpractical when, as a rule of thumb, the number of reacting species exceeds ten. More complexity to the problem is added when spatial variations in permeability, individual transport properties of species and kinetic constraints on different reactions have to be addressed.

To this end numerical models of chemical reactions and fluid flow have drawn much attention from a number of researchers due to their flexibility and better approximating capabilities. However it is worth to note that devising an exact model for a fluid-rock interaction system is rather an impossible task considering the complex nature of the natural systems and the number of interrelated factors that are to be considered. One has to be satisfied with the model that best approximates the system without violating laws of physics and chemistry together with a valid geological concept. The numerical approach to model the reactive fluid transport involves formulating the governing equations of the process into numerical algorithms. With ever advancing computer technology a large number of computer codes are being developed and tested for numerous applications and case studies. The principal difference in approach to address the problem by various authors has been on the chemical state of the system. Most have

described the systems that are assumed to be in chemical equilibrium while some have preferred far from equilibrium state where a kinetic formulation of the reactions is employed. Another group of researchers employ a combination of these reasoning out that the equilibrium is the final state of a kinetic system. Furthermore the method of solving the equations describing fluid flow and chemical reactions falls into two main categories namely, global implicit or one-step method where equations of chemical reactions and transport are coupled and solved simultaneously, and two-step method where reaction and transport terms are solved sequentially. The code IDREACT which is used throughout this work is based on a mixed equilibrium-kinetic formulation and global implicit method.

1.3 Outline of the thesis

- Chapter 1: The background of the research is explained in this introductory chapter.
- Chapter 2: A summary of the principles of reactive fluid transport modeling is given together with methods used for geochemical speciation calculation and derivation of thermodynamic data.
- Chapter 3: Treatment of solid solutions in reactive transport models requires specific codes which are computationally expensive and sometimes numerically unstable. This hinders the readily use of solid solutions in transport calculations despite their abundance in nature, especially in hydrothermal systems. An alternative approach to incorporate solid solutions in fluid-rock interaction modeling using pseudo compounds will be tested and the results will be compared with a natural example.
- Chapter 4: This chapter is on modeling K-metasomatism of Paleoproterozoic sedimentary rocks belonging to the Baraboo Interval (~1450-1750 Ma) of the southern Lake Superior Region, USA. Studies on the paleoproterozoic quartzites have revealed mineralogical transformation from an initially SiO₂-rich system to an Al₂O₃-K₂O rich one due to the action of hydrothermal fluids associated with later igneous activity. An attempt is made here to characterize the nature of fluids and flow regimes responsible for this alteration using reactive fluid transport modeling.
- Chapter 5: Higher temperature gradients found in mid-ocean ridge environments generate intense hydrothermal activity that leads to alteration of the oceanic crust. Application of reactive fluid transport models to quantify these processes has been a great challenge due to the complex interplay of affecting parameters. This chapter elaborates an attempt to model the hydrothermal alteration of Icelandic basalts with reactive fluid transport calculations. Solid solutions are incorporated into the models using the approach described in Chapter 3. Iceland being the sub

aerial exposure of the Mid-Atlantic Ridge provides an ideal site to investigate the fluid-rock interaction processes of hydrothermal systems. As thermodynamic properties of aqueous species are best known in pressure/temperature conditions prevalent in these systems, the associated fluids provide themselves for quantitative treatment. Moreover the presence of two types of reservoirs for fluids namely sea water and glaciers in Iceland enables investigating the effect of salinity on fluid-rock interaction.

Chapter 6: Reactive fluid transport models are extensively used to assess the physical, geochemical and biological processes involved in contaminated groundwater transport and treatment. Among many groundwater contaminants nitrate (NO_3^-) is a common solute whose excess concentrations in drinking water can pose health threats. This chapter describes the numerical simulation of nitrate removal by pyrite oxidation.

Approaches in Reactive Fluid Transport Modeling

2.1 Introduction

Quantifying the dynamics of natural fluid-rock interaction systems is the fundamental objective of reactive fluid flow modeling. As such the system has to be defined in terms of physical variables whose interplay is responsible for the evolution of the system. Multi-component, multi-species systems characteristic of natural fluid-rock interactions need special treatment due to multiple unknowns and their associated non-linearity. Thermodynamics of geochemical reactions, physical parameters of the medium and fluid flow characteristics of the system have to be treated accordingly for better approximating the processes. Having all these control parameters properly defined they must be incorporated into an appropriate numerical algorithm for calculations. Sections 2.2 through 2.4 of this chapter give a summary on fundamentals of multi-component reactive fluid transport models based on one dimensional multi-component reactive fluid transport code, 1DREACT[©] (Steefel, 1993). For detailed accounts the reader is referred to the excellent literature on the subject (Lichtner, 1985, 1996; Phillips, 1991; Steefel and Lasaga, 1994; Steefel and MacQuarrie, 1996; Lasaga, 1998).

2.2 Reactions in geochemical systems

A natural heterogeneous chemical system consists of an aqueous phase with dissolved ions, complexes, uncharged species and solid and/or gas phases. The fundamental concern about such a system would be to find out the concentrations, activities and fugacities of different species. This can be accomplished by solving a set of equations that describes the thermodynamic and kinetic characteristics of the system. Sections 2.2.1 through 2.2.4 elaborate the principles based on which these relations are derived. The composition of various chemical species in natural chemical systems can be described in terms of a number of independent chemical entities, defined as primary or basis species. These chemical components are of rather algebraic form than real physical entities, which are used to represent the chemical composition of the system thermodynamically and stoichiometrically. An M number of chemical reactions among N_{tot} number of species occurring in aqueous, gaseous and solid phases of the system can be expressed in general symbolic form as (Lichtner, 1985)

$$0 = \sum_{i=1}^{N_{tot}} \nu_{ir} A_i \quad (r = 1, \dots, M) \quad (2.1)$$

where v_{ir} denotes the stoichiometric matrix of the i^{th} species in the reaction. By convention v_{ir} is positive for product and negative for reactant species. A_i is the chemical formula of the i^{th} species.

2.2.1 Homogeneous reactions in the aqueous phase

The processes occurring in the aqueous phase are the reactions among species to form secondary species namely, ions, complexes and uncharged species, and the task is to solve for the unknown concentrations of these N_{tot} species. Assuming equilibrium among aqueous species in the system, the total number of independent concentrations (N_c) to be solved for is reduced from N_{tot} by N_x linearly independent reactions among the species. This leads to the partitioning of the system into N_c primary species and N_x secondary species (Lichtner, 1988; Steefel and Lasaga, 1994). Hence the reversible reactions taking place in the aqueous phase can be represented as

$$A_i = \sum_{j=1}^{N_c} v_{ij} A_j \quad (i = 1, \dots, N_x) \quad (2.2)$$

where A_j and A_i are the chemical formulae of the j^{th} and i^{th} primary and secondary species respectively. v_{ij} is the stoichiometric coefficient of the j^{th} species in the reaction. Denoting the concentration of primary species as C_j and that of secondary species as X_i following the notation of Steefel and Lasaga (1994), the law of mass action for each homogeneous reaction at equilibrium when written as dissociation of one mole of secondary species into constituent primary species takes the form

$$K_i = \frac{\prod_{j=1}^{N_c} (\gamma_j C_j)^{v_{ij}}}{X_i \gamma_i} \quad (i = 1, \dots, N_x) \quad (2.3)$$

where K_i is the equilibrium constant for the reaction in Eqn. 2.1, and γ_j and γ_i are the activity coefficients of the j^{th} and i^{th} primary and secondary species respectively. Eqn. 2.3 provides the link between primary and secondary species where the concentrations of secondary species are expressed in terms of primary species that are to be used in mass balance equations, and it reduces the number of unknowns to be solved for.

Activity coefficients of ionic species are calculated using the extended Debye-Hückel formulation which is valid for high ionic strength solutions upto sea water. When the ionic strength of the solution I is defined as

$$I = \frac{1}{2} \sum_{k=1}^{N_{tot}} C_k z_k^2 \quad (2.4)$$

where z_k and C_k are the charge and concentration of the k^{th} aqueous species respectively, and k sums up for all primary and secondary species, the activity coefficient of the k^{th} species γ_k is given by

$$\log \gamma_k = \frac{-Az_k^2 \sqrt{I}}{1 + Ba_0 \sqrt{I}} + CI \quad (2.5)$$

where A,B and C are constants depending only on temperature and pressure, and a_0 is the hydrated radius of the particular ion.

2.2.2 Heterogeneous reactions between fluid and minerals

When a fluid is brought into contact with a rock, chemical reactions will occur between the aqueous species and the minerals. Ions, molecules and complexes in the solution are adsorbed onto the mineral surfaces, chemical reactions take place, and the product species are released to the solution causing the minerals to dissolve. To continue the dissolution, it is necessary for the product species to be transported into the solution from the mineral surface, and mostly this is accomplished by diffusion. Dissolution reactions can be characterized as either diffusion-controlled or surface-controlled. If the kinetics of the reactions on the mineral surfaces is faster than the diffusion rate, the dissolution is said to be diffusion-controlled. Diffusion is faster than surface reactions in surface-controlled dissolution (Berner, 1978; Lasaga, 1984).

The total rate of change of concentration of the i^{th} species in solution R_i^{min} (in moles per unit volume of rock per unit time) is related to the rate of dissolution (or precipitation) of minerals stoichiometrically as given by (Steeffel, 1993; Steeffel and Lasaga, 1994)

$$R_i^{min} = - \sum_{m=1}^{N_m} \nu_{im} r_m \quad (i = 1, \dots, N_{tot}) \quad (2.6)$$

where r_m is the rate of dissolution or precipitation of mineral m per unit volume of rock, ν_{im} is the stoichiometric coefficient in mineral dissolution/precipitation reaction and N_m is the number of reacting minerals. The negative sign indicates that the total number of moles of i increases as the mineral dissolves when r_m is taken to be negative for dissolution reactions.

The individual mineral dissolution/precipitation rate of minerals r_m can be expressed as (Lasaga, 1981, 1998).

$$r_m = \text{sgn}(\log[Q_m / K_m]) A_m k_m \left(\prod_{i=1}^{N_c + N_x} a_i^p \right) \left| (Q_m / K_m)^M - 1 \right|^n \quad (2.7)$$

where $\log(Q_m/K_m)$ gives the saturation index for the m^{th} mineral, k_m is the dissolution/growth rate constant, A_m is the reactive surface area, a_i is the activity of the species i . M and n are experimentally determined positive numbers, and p is an empirical value. $\text{sgn}(\log[Q_m/K_m])$ gives the sign of r_m that indicates whether the mineral is dissolved or precipitated.

2.2.3 Mass balance

The total concentration of an element in the solution can be given in a mass balance equation as

$$U_j = C_j + \sum_{i=1}^{N_x} \nu_{ij} X_i \quad (j = 1, \dots, N_c) \quad (2.8)$$

where U_j is the total elemental concentration of j in the solution, C_j is the concentration of species j , X_i is the concentration of secondary species i containing ν_{ij} moles of j . Rearranging Eqn. 2.3 to get X_i and substituting in Eqn. 2.5 yields

$$U_j = C_j + \sum_{i=1}^{N_x} \nu_{ij} \frac{\prod_{j=1}^{N_c} (\gamma_j C_j)^{\nu_{ij}}}{K_i \gamma_i} \quad (j = 1, \dots, N_c) \quad (2.9)$$

which is the general expression to represent concentrations of chemical species in the system that are to be included in the chemical reaction term in the governing equation of the reactive transport.

2.2.4 Electroneutrality

The sum of the equivalents of anions and cations must be zero for electroneutrality of the solution. Then the charge balance of the species can be given as

$$0 = \sum_{k=1}^{N_{tot}} z_k C_k \quad (2.10)$$

where z_k and C_k have the same meaning as in Eqn. 2.4.

2.3 Fluid flow and transport of solutes

Solute transport in porous media is accomplished by three principal mechanisms; advection, molecular diffusion and hydrodynamic dispersion. Advective transport takes place as a result of the bodily translation of the fluid in space. Molecular diffusion occurs due to the random motion of molecules in the fluid and generally the transport scale is several orders of magnitude less than that under advection. Hydrodynamic dispersion is resulted from different velocities of adjacent fluid flow paths. The motion of a fluid through a rock is facilitated by a network of interconnected pores or fractures, and fluid elements have to move through a convoluted passage in most cases. The mean flow velocity \bar{v} of the fluid is defined as its linear displacement per unit time averaged over a representative volume of the rock. The volume of fluid that flows across a unit area per unit time through the porous medium u , known as Darcy velocity, is then related to \bar{v} by

$$u = \phi \bar{v} \quad (2.11)$$

where ϕ is the porosity. Multiplication of the mean flow velocity by porosity accounts for the effective volume through which the fluid flows.

Chemical reactions between species in the fluid phase and minerals of the matrix take place when the fluid is brought into contact with the rock. In many geological situations, the controlling factor of patterns of dissolution, precipitation and fabric alteration - in addition to temperature, pressure and reaction kinetics - is the rate at which reactants in solution can be delivered to reaction site (Phillips, 1991). The total flux of a species through a unit volume of the rock has two components; advective flux due to the bulk movement of the fluid -resulted by the Darcian flux- and diffusive flux due to molecular dispersion of the species. In addition, the concentration of the species changes as a result of dissolution/precipitation reactions between minerals and fluid in its passage through the said volume. When the concentration of species i is defined as the mass of that species in a unit volume of fluid, c_i , the overall material balance in terms of its rate of change can be expressed, for the case of one-dimensional flow, as (Krauskopf and Bird, 1995)

$$\left(\frac{\partial c_i}{\partial t} \right)_{fluid} = - \left(\frac{\partial J_i}{\partial x} \right)_{advection} - \left(\frac{\partial J_i}{\partial x} \right)_{diffusion} + \left(\frac{\partial c_i}{\partial t} \right)_{reaction} \quad (2.12)$$

The advective flux $J_{i,advection}$ is related to the volume flow rate (Darcy velocity) of the fluid u according to

$$J_{i,advection} = u c_i \quad (2.13)$$

Diffusive flux of species in a stationary fluid is proportional to the concentration gradient, a relationship described by Fick's first law,

$$J_{i,diffusion} = -D_i \left(\frac{\partial c_i}{\partial x} \right) \quad (2.14)$$

where D_i is the diffusion coefficient of i^{th} species. The last term in Eqn. 2.12 corresponds to the reaction rate of species given by R_i^{min} in Eqn. 2.6. The generalized form of Eqn. 2.12 when calculated for the active void fraction ϕ and with substitution from Eqns. 2.6, 2.13 and 2.14 yields an expression for the solute mass conservation,

$$\left(\frac{\partial \phi U_j}{\partial t} \right) + \nabla \cdot (u U_j - D \nabla U_j) = R_j^{min} \quad (2.15)$$

where c_i has been replaced by U_j to represent the total concentrations given by Eqn. 2.9. Diffusion coefficient has been assumed to be the same for both primary and secondary species. Eqn. 2.15 is the principal governing equation of coupled multi-component reactive transport and when formulated into a suitable numerical algorithm it provides with a smart tool to model the processes involving fluid flow and chemical reactions between fluid and rock.

2.4 Numerical method

The mathematical model governing fluid flow and chemical reactions consists of a set of partial differential equations and boundary conditions which are embedded in Eqn. 2.15, and the goal is to solve it to predict the values of the unknown variables in time and space throughout the problem domain, which in this case are concentrations, activities and fugacities of the constituent species. Solving such an equation for an analytical solution for every point of interest has practical limitations. Thus numerical methods are employed where the solution yields values for a pre-determined finite number of points. The two widely used numerical methods are finite element method and finite difference method. The former discretizes the problem domain into a finite number of triangular elements while the latter into a rectangular grid. Given the boundary and initial conditions the task is to find out the value of the unknown variable at each point in terms of those values at its neighbouring points.

Basically algorithms of reactive fluid transport fall within two major categories based on the approach used to solve Eqn. 2.15. Sequential or two step method solves for chemical reactions first and then the fluid transport is calculated. Hence the new species concentrations obtained from the solution of chemical reaction part is transported in time and space iteratively until the convergence is achieved. In contrast global implicit or one step method solves for chemical reactions and fluid transport simultaneously. A more descriptive account on the latter method

using finite difference formulation is given here as reactive transport modeling in subsequent chapters will be based on it.

In the integrated finite difference formulation, the problem domain is discretized into a finite number of nodal points and the governing partial differential equations are expressed as a set of algebraic equations in terms of spatial and time coordinates. Figure 1.1 illustrates this concept for a one-dimensional case.

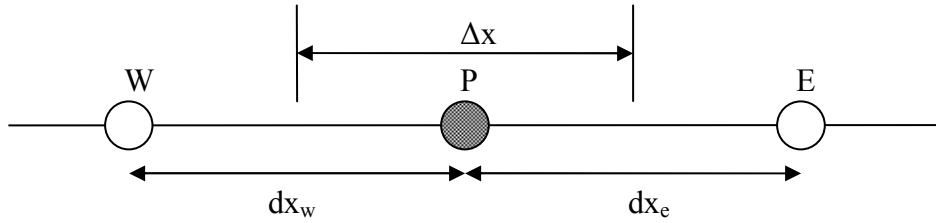


Figure 1.1: One-dimensional finite difference grid indicating the nodal point P where the solution for the set of equations has to be found in terms of the values at its neighbours W and E.

When Eqn. 2.15 is discretized in a one-dimensional finite difference grid it can be stated in the form described by Steefel (1993) for a diffusion dominated system as;

$$\frac{\Delta x}{\Delta t} (U_j^P(t + \Delta t) - U_j^P(t)) + a_P U_j^P(t + \Delta t) - a_E U_j^E(t + \Delta t) - a_W U_j^W(t + \Delta t) - R_j^{\min}(t + \Delta t) \Delta x = 0 \quad (2.16)$$

where

$$a_E = \frac{D_e}{(dx)_e}, \quad a_W = \frac{D_w}{(dx)_w} \quad \text{and} \quad a_P = a_E + a_W.$$

Subscripts e and w denote the variable at the boundaries of the control volume. For simplicity diffusion coefficient (D) will be taken as constant. Eqn 2.16 is a non-linear function of primary species concentrations at the nodal point concerned and those of its neighbours. Hence it must be solved with an iterative scheme. Its Taylor series expansion takes the form,

$$\sum_{j'=1}^{N_c} \frac{\partial f_j^P}{\partial \ln C_{j'}^P} \delta \ln C_{j'}^P + \sum_{j'=1}^{N_c} \frac{\partial f_j^P}{\partial \ln C_{j'}^E} \delta \ln C_{j'}^E + \sum_{j'=1}^{N_c} \frac{\partial f_j^P}{\partial \ln C_{j'}^W} \delta \ln C_{j'}^W = -f_j^P \quad (2.17)$$

where j' accounts for all solute species. Eqn. 2.17 can be solved with Newton-Raphson iteration. Once $\delta \ln C_{j'}$ values are calculated they are used to update the concentrations of primary species at the new time step according to Eqn. 2.18.

$$\ln C_{j'}^{new} = \ln C_{j'}^{old} + \delta \ln C_{j'} \quad (2.18)$$

The convergence criterion of the iterative procedure is set to a desired value, mostly where the function residuals do not significantly change between subsequent time steps. 1DREACT accommodates the advective transport in Eqn. 2.16 using a power law scheme to define a_E and a_W coefficients where,

$$a_E = D_e \left\| 0, \left(1 - \frac{0.1 \delta x_e |u_e|}{D_e} \right)^5 \right\| + \|0, -u_e\| \quad (2.19)$$

$$a_W = D_w \left\| 0, \left(1 - \frac{0.1 \delta x_w |u_w|}{D_w} \right)^5 \right\| + \|0, u_w\|. \quad (2.20)$$

The operator $\|A, B\|$ imposes that the algorithm uses the greater value from A and B.

2.5 Speciation calculation

The chemical form in which an element is present is one of the most important factors in understanding a geochemical system. Adsorption, desorption and complexation reactions depending on the pressure/temperature conditions determine the nature and abundance of chemical species of the system. Therefore it is necessary for reactive transport models to incorporate right chemical species in them. Generally at high pressures/temperatures fluids are chloride-rich brines and alkali chlorides are dominant under these conditions (Eugster and Baumgartner, 1987). Silica solubility in neutral to acidic solutions is dominated by uncharged

hydroxide species (Walther, 1986; Manning, 1994). Experimental studies by Pak et al., (2003) postulate alkali-aluminum complexes to be the dominant aluminum species at higher pressures and temperatures. Hence due care must be taken to choose the correct set of expected species in a fluid-rock interaction system. For calculation of initial speciation and aqueous species concentrations at relevant pressures and temperatures an equilibrium geochemical model SOLUB (Roselle and Baumgartner, 1995) will be used. It calculates the speciation and total concentrations of the fluid phase in equilibrium with a given mineral assemblage by solving the non-linear equations that describe the equilibrium between minerals and aqueous species together with charge balance and total concentration equations (Eugster and Baumgartner, 1987). These initial concentrations are used as input values for reactive transport calculations.

2.6 Thermodynamic database

1DREACT reads a thermodynamic database for fluid-rock interaction calculations. The thermodynamic database contains logarithmic equilibrium constants ($\log K$'s) of reactions of aqueous species and minerals at different temperatures. They are written as hydrolysis reactions of one mole of mineral phase. To complete this data, a series of dissociation reactions is included for each additional aqueous ionic species. The only comprehensive dataset available for aqueous ions at the higher P-T conditions is the one associated with SUPCRT92 computer program (Johnson et al., 1993). Following the recommendations of Pak et al., (2003) and Hauzenberger et al., (2001) the data set of Oelkers et al., (1995) will be used to calculate the $\log K$'s of aqueous species reactions. The most extensive thermodynamic dataset for minerals is that of Holland and Powell (1991, 1998). A restricted data set for aqueous species is available in this database, but the quality of the thermodynamic data for aqueous species has been questioned (eg: Pak et al., 2003; Hauzenberger et al., 2001). Therefore the thermodynamic aqueous species data of Oelkers et al., (1995) will be combined with the mineral database of Holland and Powell (1991, 1998) to obtain more accurate $\log K$'s for mineral-fluid reactions. Gibb's free energies of formation of aqueous species are calculated using SUPCRT92 for the P-T ranges of interest in each test case. Similarly those of minerals and H₂O are calculated using the program FrenDly from the Perplex program suite (Connolly and Petrini, 2002). The Gibb's free energy of a dissolution reaction for a mineral m is

$$\Delta G_r^{P,T} = \sum_i^{N_c} \nu_i \Delta G_{f,i}^{P,T} - (\Delta G_{f,m}^{P,T} + \Delta G_{f,H_2O}^{P,T}) \quad (i = 1, \dots, N_c) \quad (2.21)$$

where $\Delta G_{f,i}^{P,T}$ is the Gibb's free energy of formation of the i^{th} species in m at the pressure and temperature of interest, $\Delta G_{f,m}^{P,T}$ is that of the mineral, ν_i is the stoichiometric coefficient of the i^{th} species in the reaction and N_c is the number of aqueous species in the reaction. The first term on

the right hand side of Eqn. 2.21 is obtained from SUPCRT92 calculations and the second term from Frenly. The $\log K$ of the reaction can then be computed from

$$\log K = \frac{-\Delta G_r^{P,T}}{2.303RT} \quad (2.22)$$

where R is the gas constant and T is the absolute temperature. The thermodynamic databases generated for each model contain $\log K$ values at several temperatures corresponding to the relevant pressure conditions of the models. 1DREACT interpolates the $\log K$'s using a simple polynomial function. P-T dependent parameters for the Debye-Huckel equation are calculated following Helgeson and Kirkham (1974), and fitted to the relevant pressure and temperature range of the models using a third order polynomial fit. As a result of the applicable P-T range of CORK equation, this approach of calculating $\log K$'s of hydrolysis reactions will be limited to the temperatures above 100 °C. In other cases SUPCRT92 as described above will be used. Water densities corresponding to the P-T conditions along the model grids are calculated using a third order polynomial introduced to the code.

References

- Berner, R.A., 1978. Rate control of mineral dissolution under earth surface conditions. *Am. J. Sci.* 278, 1235-1252.
- Connolly, J.A.D., 1990. Multivariable phase diagrams: An algorithm based on generalized thermodynamics. *Am. J. Sci.*, 290, 666-718.
- Connolly, J.A.D. and Petrini, K., 2002. An automated strategy for calculation of phase diagram sections and retrieval of rock properties as a function of physical conditions. *J. Met. Geol.* 20, 697-708.
- Eugster, H.P. and Baumgartner, L.P., 1987. Mineral solubilities and speciation in supercritical metamorphic fluids. In: Carmichaels, I.S.E. and Eugster, H.P. (Eds), *Thermodynamic modeling of geological materials: Minerals, fluids and melts*. Mineralogical Society of America: *Reviews in Mineralogy*. 17, 367-403.
- Haar, L., Gallagher, J.S. and Kell, G.S., 1984. *NBS/NRC steam tables*. Hemisphere, Washington D.C., 320p.
- Hauzenberger, C.A., Baumgartner, L.P. and Pak, T. M., 2001. Experimental study on the solubility of the "model"-pelite mineral assemblage albite + K-feldspar + andalusite + quartz in supercritical chloride-rich aqueous solutions at 0.2 GPa and 600 degrees C. *Geochim. Cosmochim. Acta.* 65(24), 4493-4507.
- Helgeson, H.C., Kirkham, D.H. and Flowers, G.C., 1981. Theoretical prediction of the thermodynamic behaviour of aqueous electrolytes at high pressures and temperatures: IV.

- Calculation of activity coefficients and osmotic coefficients and apparent molal and standard and relative molal properties to 600°C and 5kb. *Am. J. Sci.*, 281, 1249-1493.
- Holland, T. and Powell, R., 1991. A compensated-Reidlich-Kwong (CORK) equation for volumes and fugacities of CO₂ and H₂O in the range 1 bar to 50 kbar and 100-1600°C. *Contrib. Mineral. Petrol.* 109, 265-273.
- Holland, T.J.B. and Powell, R., 1998. An internally consistent thermodynamic data set for phases of petrological interest. *J. Met. Geol.* 16, 309-343.
- Johnson, J.W. and Norton, D., 1991. Critical phenomena in hydrothermal systems: state, thermodynamic, electrostatic, and transport properties of H₂O in the critical region. *Am. J. Sci.*, 291(6), 541-648.
- Johnson, J.W., Oelkers, E.H. and Helgeson, H.C., 1992. SUPCRT92: A software package for calculating the standard molal thermodynamic properties of minerals, gases, aqueous species, and reactions from 1 to 5000 bars and 0 to 1000 degrees C. *Computers & Geosciences*, 18(7), 899-947.
- Krauskopf, K.B. and Bird, D.K., 1995. *Introduction to Geochemistry*. Third Edition. McGraw-Hill, Inc., 647p.
- Lasaga, A.C., 1981. Rate laws in chemical reactions. In: Lasaga, A.C. and Krikpatrick, R.J. (Eds) *Kinetics of geochemical processes*. Mineralogical Society of America: *Reviews in Mineralogy* 8, 135-169.
- Lasaga, A.C., 1984. Chemical kinetics of water-rock interactions. *J. Geophys. Res.* 89, 4009-4025.
- Lasaga, A.C., 1998. *Kinetic theory in the earth sciences*. Princeton University Press, p728.
- Lichtner, P.C., 1985. Continuum model for simultaneous chemical reactions and mass transport in hydrothermal systems. *Geochim. Cosmochim. Acta* 49, 779-800.
- Lichtner, P.C., 1988. The quasi-stationary state approximation to coupled mass transport and fluid-rock interaction in a porous medium. *Geochim. Cosmochim. Acta* 52, 143-165.
- Lichtner, P.C., 1996. Continuum formulation of multicomponent-multiphase reactive transport. In: Lichtner, P.C., Steefel, C.I., and Oelkers, E.H. (Eds), *Reactive transport in porous media*. Mineralogical Society of America: *Reviews in Mineralogy*, 34, 1-79.
- Manning, C.E., 1994. The solubility of quartz in H₂O in the lower crust and upper mantle. *Geochim. Cosmochim. Acta* 58, 4831-4839.
- Oelkers, E.H., Helgeson, H.C., Shock, E.L., Sverjensky, D.A., Johnson, J.W., and Pokrovskii, V.A., (1995). Summary of the apparent partial standard partial molal Gibbs free energies of formation of aqueous species, minerals and gases at pressures 1 to 5000 bars and temperatures 25 to 1000 degrees C. *J. Phys. Chem. Ref. Data* 24, 1401-1560.
- Pak, T.M., Hauenberger, C.A. and Baumgartner, L.P., 2003. Solubility of the assemblage albite+K-feldspar+andalusite+quartz in supercritical aqueous chloride solutions at 650 °C and 2 kbar. *Chemical Geology* 200, 377-393.
- Phillips, O.M., 1991. *Flow and reactions in permeable rocks*. Cambridge University Press, 285p.

- Roselle, G.T. and Baumgartner, L.P., 1995. Experimental determination of anorthite solubility and calcium speciation in supercritical chloride solutions at 2 kb from 400 to 600°C. *Geochim. Cosmochim. Acta* 59, 1539-1549.
- Shock, E.L., Oelkers, E.H., Johnson, J.W., Sverjensky, D.A. and Helgeson, H.C., 1992. Calculation of the thermodynamic properties of aqueous species at high pressures and temperatures: effective electrostatic radii, dissociation constants, and standard partial molal properties to 10000C and 5kb. *J. Chem. Soc. Lond. Faraday Trans.* 88(6), 803-826.
- Steefel, C.I., 1993. 1DREACT User Manual.
- Steefel, C.I. and Lasaga, A.C., 1994. A coupled model for transport of multiple chemical species and kinetic precipitation/dissolution reactions with applications to reactive flow in single phase hydrothermal system. *Am. J. Sci.* 294, 529-592.
- Steefel, C.I. and MacQuarrie, K.T.B., 1996. Approaches to modeling of reactive transport in porous media. In: Lichtner, P.C., Steefel, C.I. and Oelkers, E.H. (Eds), *Reactive transport in porous media. Mineralogical Society of America: Reviews in Mineralogy*, 34, 83-129.
- Sverjensky, D.A., Shock, E.L. and Helgeson, H.C., 1997. Prediction of the thermodynamic properties of aqueous metal complexes to 1000 °C and 5 kb. *Geochim. Cosmochim. Acta* 61, 1359-1412.
- Tanger IV, J.C. and Helgeson, H.C., 1988. Calculation of thermodynamic and transport properties of aqueous species at high pressures and temperatures. Revised equations of state for the standard partial molal properties of ions and electrolytes. *Am. J. Sci.* 288, 19-88.
- Walther, J.V., 1986. Mineral solubilities in supercritical H₂O solutions. *Pure Appl. Chem.* 58, 1585-1598.

Using Pseudo-Compounds to Model Solid Solutions in Reactive Fluid Transport Models

ABSTRACT

Treatment of solid solutions in reactive fluid transport models requires that the composition of the solid is treated as a variable. Since many thermodynamic models of solid solutions are highly non-linear, this can seriously impact the stability of the numerical algorithm. In addition, this can require an unreasonable amount of computational time. To improve performance and stability, phase equilibrium calculations can be performed using pseudo compounds. Thermodynamic properties of a varying number of intermediate composition phases are calculated for a solid solution mixing model and included in the mineral thermodynamic database for the transport calculation. The one dimensional reactive fluid transport code, 1DREACT (Steeffel, 1993) was used to test this approach. We used the solid solution of plagioclase as a test case, by calculating a diffusion profile that develops between an anorthite- and an albite-rich zone at hydrothermal temperatures. Several different mixing models were tested. No modification of the transport code is required. Initial speciation and concentrations of aqueous species were calculated using a geochemical speciation model (Roselle and Baumgartner, 1995). The thermodynamic properties of aqueous species were calculated using the SUPCRT92 program (and corresponding thermodata) while those of minerals were calculated using the Perplex software with the Holland and Powel (1998) thermodata of minerals. Fluid-rock interaction simulations result in precipitation of intermediate plagioclase compositions, as expected. Asymmetric diffusional profiles develop between the anorthite and albite zones due to the difference in solubility of highly charged, small aluminum and silica ions, as well as that of Na (faster) and Ca (slower). Mixing gaps are readily produced where predicted by the non-ideal mixing model used. Relative aluminum immobility results in porosity reduction in the zones where anorthite is replaced, and in porosity increase, where albite is replaced by the intermediate plagioclase compositions. These observations are in agreement with observations from experiments (Schliestedt, 1989, personal comm.). As few as nine intermediate compositions are sufficient to characterize the diffusional profile between albite and anorthite.

3.1 Introduction

Solid solutions are abundant in natural fluid-rock interaction systems, especially at high temperatures. Incorporating them into reactive fluid transport models is essential to better approximate the processes taking place in hydrothermal environments. However use of solid solutions in these models requires that specialized codes are added to the transport algorithm. Composition of solid solutions in transport systems depends on the fluid composition. Hence their composition has to be treated as a variable to be solved for. Many thermodynamic models of solid solutions are highly non-linear and their use in a reactive transport model can greatly affect the stability of the transport algorithm. The mathematical formalism of non-ideal mixing is quite complex. Indeed, up to recent times a single full minimization of the Gibbs free energy has required up to a few seconds for a fixed composition. Since reactive flow modeling requires minimization of the free energy at any given nodal point within the domain for every time step this results in prohibitive computational efforts.

A method to simplify the mathematics of solid solutions and to increase the performance of the algorithms used to calculate phase equilibria pseudo compounds approach was introduced (see. e.g. Connolly, 1990) whose thermodynamic properties are used in reactive transport calculations. The major advantage of this approach is that any desired mixing model of a given solid solution can be tested without modifying the transport code. A crucial aspect is the number of solid solution phases (pseudo-compounds) that need to be included to accurately model the system behaviour. If many are needed, this will once again slow down significantly the calculations. In this paper we test the feasibility of incorporating solid solution into a diffusion controlled reactive transport system, taking plagioclase as an example. We use a one-dimensional coupled multi-component reactive transport code, 1DREACT (Steefel, 1993) to test this approach.

3.2 Pseudo compounds

Nonlinear Free energy – composition surfaces of phases with variable compositions can be approximated by a series of arbitrarily defined compounds, typically taken to be regularly spaced in between the end member compositions. They are called here pseudo compounds following Connolly, (1990). This leads to discretization of the continuous range of composition into a finite number of intermediate phases. The thermodynamic properties of the intermediate phases are calculated using a mixing model for the end member compositions.

The Gibb's free energy of a mixture of A and B (denoted G_{AB}) in a binary solid solution between components A and B can be split into two parts representing the free energy of the mechanical mixture and that of mixing.

$$G_{AB} = \Delta G^{mechanical} + \Delta G^{mixing} \quad (3.1)$$

The Gibb's free energy of the mechanical mixture between the end members A and B of the binary solid solution can be expressed as

$$\Delta G^{mechanical} = X_A \Delta G_A + X_B \Delta G_B \quad (3.2)$$

where X_A and X_B are mole fractions of A and B in AB , and ΔG_A and ΔG_B are the Gibb's free energy of formation of pure A and B phases at the pressure and temperature of interest. The free energy of non ideal mixing is given by

$$\Delta G^{mixing} = RT(X_A \ln a_A + X_B \ln a_B) \quad (3.3)$$

where R is the gas constant, T is the absolute temperature, and a_A and a_B are activities of A and B . Figure 3.1 shows the derivation of free energies of three intermediate phases having mole fractions of x , y and z of end member B . The non linearity of the free energy curve is the result of the free energy of mixing. A myriad of solid solution models exists in the literature. For ideal solutions the activities are equal to the mole fractions of the corresponding components. While solid solutions are often adequate for transport calculations, more elaborate formulations are required for many solid solutions, for example for minerals with solid solution gaps, multiple mixing sites, or solutions in which linear dependant end members are present. Additionally, structural transformation, as seen in the case of plagioclase, can add complexity to the solid solution model. For a review of this topic the reader is referred to Spear (1993).

3.3 Mixing models for plagioclase

Although compositionally simple, plagioclases form a complex solid solution due to Al-Si order-disorder and the coupled CaAl – NaSi exchange which changes the geometry of its framework structure. Plagioclase solid solutions received a lot of attention, as is evident by the number of experimental (e.g. Orville, 1972; Carpenter and McConnell, 1984; Schliestedt and Johannes, 1990; Carpenter, 1994) and theoretical (Kerrick and Darken, 1975; Newton et al., 1980; Holland and Powell, 1992, 2003) studies, since it is one of the most abundant minerals in the earth's crust. Several models based on ideal,

non-ideal, Al-avoidance, ordered and disordered mixing have been proposed (Kerrick and Darken, 1975; Newton et al., 1980; Holland and Powell, 1992, 2003). Since the free energy of any pseudo compound depends on the selected mixing model (Fig. 3.2) a separate thermodynamic database was created for each mixing model.

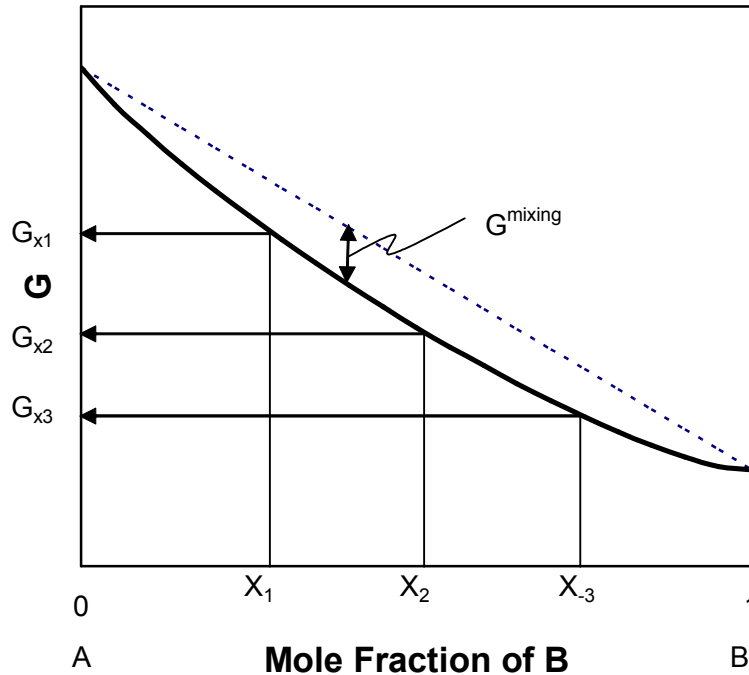


Figure 3.1. Gibb’s free energy curve for a binary solid solution with end members A and B. X_1 , X_2 and X_3 are intermediate compositions, called here pseudo compounds, and G_{X1} , G_{X2} and G_{X3} are the Gibb’s free energies of these pseudo compounds, respectively.

We use three mixing models for plagioclase solid solution – (a) ideal molecular mixing model; (b) the Al-avoidance model of Kerrick and Darken (1975); and (c) a non-ideal, Al-avoidance model for high-structural state plagioclase (Newton et al., 1980). However Carpenter and McConnell (1984), and Carpenter and Ferry (1984) pointed out, that it does not consider any structural transformations, which are encountered in plagioclase solid solution. They suggest that Newton et al.’s experimental results may not represent equilibrium structural states. Nevertheless in the absence of a convenient non-ideal mixing model for plagioclase solid solution, we used it to test the validity of our approach, since it predicts mixing gaps at the conditions considered.

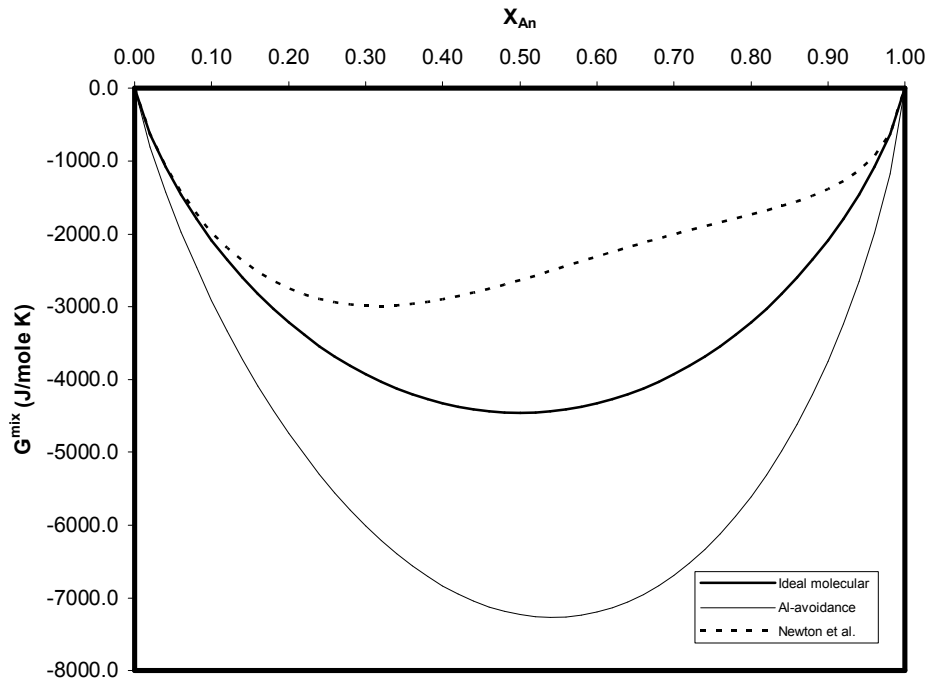


Figure 3.2. Gibb's free energy of mixing in plagioclase solid solution for three mixing models at 500 °C and 2.5 kbar. There is a mixing gap in non-ideal mixing model of Newton *et al.*, (1980).

3.4 Thermodynamic databases

The thermodynamic databases used contain the logarithmic equilibrium constants ($\log K$'s) of reactions of aqueous species and minerals at different temperatures. They are written as the hydrolysis of one mole of species into its components. Dissociation reactions are included for aqueous ionic species. There are two datasets that provide thermodynamic properties of aqueous ions at supercritical conditions: (a) the one associated with SUPCRT92 (Johnson *et al.*, 1993); and (b) that associated with Thermocalc (Holland and Powell, 1991, 1998). The thermodynamics of aqueous species of the latter group was criticized by Pak *et al.*, (2003) and Hauzenberger *et al.*, (2001) who found that it does not well represent their experimentally determined concentrations of alkalis and aluminum in chlorine-rich solutions in equilibrium with aluminosilicates, feldspars, muscovite, and quartz under supercritical conditions. They recommend the use of the SUPCRT92 database provided by Oelkers *et al.*, (1995). Following their suggestions for aqueous species, we nevertheless used the thermodynamic dataset for minerals given by Holland and Powell (1991, 1998). Gibb's free energies of formation of aqueous species were calculated using SUPCRT92 at 2.5 kbar and 400 °C - 700 °C.

Those of minerals and H₂O were calculated using the Perplex programs (Connolly and Petrini, 2002) with the database of Holland and Powell (1991, 1998), and the modified CORK equation of state for water. The Gibb's free energy of the dissolution reaction of a mineral m is

$$\Delta G_r^{P,T} = \sum_i^{N_c} \nu_i \Delta G_{f,i}^{P,T} - (\Delta G_{f,m}^{P,T} + \Delta G_{f,H_2O}^{P,T}) \quad (i = 1, \dots, N_c) \quad (3.4)$$

where $\Delta G_{f,i}^{P,T}$ is the Gibb's free energy of formation of the i^{th} species in m at the pressure and temperature of interest, $\Delta G_{f,m}^{P,T}$ is that of the mineral, ν_i is the stoichiometric coefficient of the i^{th} species in the reaction and N_c is the number of component species. The first term on the right hand side of Equation 3.4 is obtained from SUPCRT92 and the second term from Perplex. The $\log K$ of the reaction can then be computed from $\Delta G_r^{P,T} = -2.303RT \log K$ where R is the gas constant and T is the absolute temperature. Once the $\log K$'s of reactions of end member components are calculated they can be used to calculate those of the intermediate phases. $\log K$ of the dissolution reaction of an intermediate composition of the plagioclase solid solution can be obtained from

$$\log K_{plag} = X_{ab} \log K_{an} + X_{an} \log K_{an} + X_{ab} \log a_{ab} + X_{an} \log a_{an} \quad (3.5)$$

where K_{plag} , K_{ab} and K_{an} are the equilibrium constants of the reactions of pseudo compound, albite, and anorthite respectively. Each mixing model yields different $\log K_{plag}$'s as activities of albite and anorthite in Equation 3.5 change depending on the model used. The thermodynamic database is complemented with all necessary dissociation reactions for aqueous species. Table 3.1 lists the mineral hydrolysis and aqueous species dissociation reactions, along with the obtained $\log K$ values used in the models. P-T dependent parameters for the Debye-Huckle equation were calculated following Helgeson and Kirkham (1974), and were fitted to the relevant pressure and temperature range of the model using a third order polynomial fit. Density of water was calculated using Perple_X program for a range of pressures and temperatures using the CORK equation of state of Holland and Powell (1991, 1998).

Table 3.1. Mineral and aqueous species reactions and their $\log K$'s used in simulations. Plagioclase pseudo compound reactions calculated using different mixing models were included in different databases. *Id*: ideal molecular model, *Aa*: Al-avoidance model, *Nw*: Newton et al.'s model.

Reaction	LogK				
	400 °C	500 °C	600 °C	700 °C	
<i>Aqueous species</i>					
$\text{Al(OH)}_2^+ + 2\text{H}^+ = \text{Al}^{+3} + 2\text{H}_2\text{O}$	-0.1188	-1.5573	-2.7573	-3.8169	
$\text{CaCl}_2(\text{aq}) = \text{Ca}^{+2} + 2\text{Cl}^-$	-2.6170	-4.1145	-5.7500	-7.4898	
$\text{CaCl}^+ = \text{Ca}^{+2} + \text{Cl}^-$	-1.8148	-2.7167	-3.6703	-4.6633	
$\text{HSiO}_3^- + \text{H}^+ = \text{SiO}_2(\text{aq}) + \text{H}_2\text{O}$	8.8705	9.5861	10.4197	11.3242	
$\text{HCl}(\text{aq}) = \text{H}^+ + \text{Cl}^-$	-1.2249	-2.0739	-3.0558	-4.1247	
$\text{NaCl}(\text{aq}) = \text{Na}^+ + \text{Cl}^-$	-0.5587	-1.0447	-1.5978	-2.2037	
$\text{NaAlO}_2(\text{aq}) + 4\text{H}^+ = \text{Na}^+ + \text{Al}^{+3} + 2\text{H}_2\text{O}$	5.0659	2.9664	1.2802	-0.1658	
$\text{NaHSiO}_3(\text{aq}) + \text{H}^+ = \text{Na}^+ + \text{SiO}_2(\text{aq}) + \text{H}_2\text{O}$	8.0575	8.5880	9.1232	9.6417	
$\text{H}^+ + \text{OH}^- = \text{H}_2\text{O}$	9.9909	10.1715	10.5209	10.9881	
<i>Minerals</i>					
$\text{Albite} + 4\text{H}^+ = \text{Na}^+ + \text{Al}^{+3} + 3\text{SiO}_2(\text{aq}) + 2\text{H}_2\text{O}$	-3.1379	-3.9187	-4.3775	-4.8260	
$\text{Andalusite} + 6\text{H}^+ = 2\text{Al}^{+3} + \text{SiO}_2(\text{aq}) + 3\text{H}_2\text{O}$	-7.9164	-10.6003	-11.2291	-14.6522	
$\text{Anorthite} + 8\text{H}^+ = \text{Ca}^{+2} + 2\text{Al}^{+3} + 2\text{SiO}_2(\text{aq}) + 4\text{H}_2\text{O}$	-4.1151	-7.5209	-10.2531	-12.6242	
$\text{Quartz} = \text{SiO}_2(\text{aq})$	-1.3793	-1.1079	-0.8856	-0.7027	
<i>Plagioclase pseudo compounds</i>					
$\text{Ab}_{95}\text{An}_{05} + 4.2\text{H}^+ = 0.95\text{Na}^+ + 0.05\text{Ca}^{+2} + 1.05\text{Al}^{+3}$ + $2.95\text{SiO}_2(\text{aq}) + 2.1\text{H}_2\text{O}$	<i>Id.</i>	-3.2730	-4.1850	-4.7575	-5.3021
	<i>Aa.</i>	-3.3021	-4.2141	-4.7865	-5.3311
	<i>Nw.</i>	-3.2671	-4.1836	-4.7596	-5.3070
$\text{Ab}_{90}\text{An}_{10} + 4.4\text{H}^+ = 0.90\text{Na}^+ + 0.10\text{Ca}^{+2} + 1.10\text{Al}^{+3}$ + $2.90\text{SiO}_2(\text{aq}) + 2.2\text{H}_2\text{O}$	<i>Id.</i>	-3.3769	-4.4201	-5.1062	-5.7470
	<i>Aa.</i>	-3.4327	-4.4760	-5.1621	-5.8029
	<i>Nw.</i>	-3.3597	-4.4124	-5.1058	-5.7523
$\text{Ab}_{85}\text{An}_{15} + 4.6\text{H}^+ = 0.85\text{Na}^+ + 0.15\text{Ca}^{+2} + 1.15\text{Al}^{+3}$ + $2.85\text{SiO}_2(\text{aq}) + 2.3\text{H}_2\text{O}$	<i>Id.</i>	-3.4681	-4.6426	-5.4424	-6.1793
	<i>Aa.</i>	-3.5486	-4.7231	-5.5229	-6.2598
	<i>Nw.</i>	-3.4354	-4.6246	-5.4357	-6.1815
$\text{Ab}_{80}\text{An}_{20} + 4.8\text{H}^+ = 0.80\text{Na}^+ + 0.20\text{Ca}^{+2} + 1.20\text{Al}^{+3}$ + $2.80\text{SiO}_2(\text{aq}) + 2.4\text{H}_2\text{O}$	<i>Id.</i>	-3.5507	-4.8565	-5.7700	-6.6030
	<i>Aa.</i>	-3.6537	-4.9594	-5.8729	-6.7059
	<i>Nw.</i>	-3.4994	-4.8251	-5.7539	-6.5992
$\text{Ab}_{75}\text{An}_{25} + 5.0\text{H}^+ = 0.75\text{Na}^+ + 0.25\text{Ca}^{+2} + 1.25\text{Al}^{+3}$ + $2.75\text{SiO}_2(\text{aq}) + 2.5\text{H}_2\text{O}$	<i>Id.</i>	-3.6265	-5.0635	-6.0906	-7.0198
	<i>Aa.</i>	-3.7496	-5.1866	-6.2137	-7.1429
	<i>Nw.</i>	-3.5544	-5.0166	-6.0632	-7.0078
$\text{Ab}_{70}\text{An}_{30} + 5.2\text{H}^+ = 0.70\text{Na}^+ + 0.30\text{Ca}^{+2} + 1.30\text{Al}^{+3}$ + $2.70\text{SiO}_2(\text{aq}) + 2.6\text{H}_2\text{O}$	<i>Id.</i>	-3.6964	-5.2647	-6.4055	-7.4308
	<i>Aa.</i>	-3.8374	-5.4056	-6.5464	-7.5717
	<i>Nw.</i>	-3.6027	-5.2013	-6.3655	-7.4093
$\text{Ab}_{65}\text{An}_{35} + 5.4\text{H}^+ = 0.65\text{Na}^+ + 0.35\text{Ca}^{+2} + 1.35\text{Al}^{+3}$ + $2.65\text{SiO}_2(\text{aq}) + 2.7\text{H}_2\text{O}$	<i>Id.</i>	-3.7612	-5.4607	-6.7152	-7.8366
	<i>Aa.</i>	-3.9176	-5.6171	-6.8715	-7.9929
	<i>Nw.</i>	-3.6459	-5.3805	-6.6621	-7.8050

Reaction		LogK			
		400 °C	500 °C	600 °C	700 °C
Ab60An40 + 5.6H ⁺ = 0.60Na ⁺ + 0.40Ca ⁺² + 1.40Al ⁺³ + 2.60SiO ₂ (aq) + 2.8H ₂ O	<i>Id.</i>	-3.8211	-5.6519	-7.0200	-8.2376
	<i>Aa.</i>	-3.9905	-5.8212	-7.1894	-8.4069
	<i>Nw.</i>	-3.6855	-5.5557	-6.9542	-8.1960
Ab55An45 + 5.8H ⁺ = 0.55Na ⁺ + 0.45Ca ⁺² + 1.45Al ⁺³ + 2.55SiO ₂ (aq) + 2.9H ₂ O	<i>Id.</i>	-3.8766	-5.8386	-7.3204	-8.6341
	<i>Aa.</i>	-4.0563	-6.0183	-7.5001	-8.8138
	<i>Nw.</i>	-3.7228	-5.7280	-7.2430	-8.5831
Ab50An50 + 6.0H ⁺ = 0.50Na ⁺ + 0.50Ca ⁺² + 1.50Al ⁺³ + 2.50SiO ₂ (aq) + 3.0H ₂ O	<i>Id.</i>	-3.9276	-6.0209	-7.6163	-9.0262
	<i>Aa.</i>	-4.1150	-6.2083	-7.8038	-9.2136
	<i>Nw.</i>	-3.7590	-5.8983	-7.5293	-8.9673
Ab45An55 + 6.2H ⁺ = 0.45Na ⁺ + 0.55Ca ⁺² + 1.55Al ⁺³ + 2.45SiO ₂ (aq) + 3.1H ₂ O	<i>Id.</i>	-3.9743	-6.1988	-7.9079	-9.4139
	<i>Aa.</i>	-4.1665	-6.3910	-8.1001	-9.6061
	<i>Nw.</i>	-3.7950	-6.0676	-7.8138	-9.3491
Ab40An60 + 6.4H ⁺ = 0.40Na ⁺ + 0.60Ca ⁺² + 1.60Al ⁺³ + 2.40SiO ₂ (aq) + 3.2H ₂ O	<i>Id.</i>	-4.0166	-6.3723	-8.1952	-9.7972
	<i>Aa.</i>	-4.2104	-6.5662	-8.3890	-9.9911
	<i>Nw.</i>	-3.8318	-6.2365	-8.0971	-9.7292
Ab35An65 + 6.6H ⁺ = 0.35Na ⁺ + 0.65Ca ⁺² + 1.65Al ⁺³ + 2.35SiO ₂ (aq) + 3.3H ₂ O	<i>Id.</i>	-4.0543	-6.5414	-8.4778	-10.1760
	<i>Aa.</i>	-4.2464	-6.7334	-8.6699	-10.3681
	<i>Nw.</i>	-3.8701	-6.4058	-8.3798	-10.1078
Ab30An70 + 6.8H ⁺ = 0.30Na ⁺ + 0.70Ca ⁺² + 1.70Al ⁺³ + 2.30SiO ₂ (aq) + 3.4H ₂ O	<i>Id.</i>	-4.0873	-6.7056	-8.7557	-10.5501
	<i>Aa.</i>	-4.2739	-6.8921	-8.9423	-10.7366
	<i>Nw.</i>	-3.9104	-6.5757	-8.6621	-10.4852
Ab25An75 + 7.0H ⁺ = 0.25Na ⁺ + 0.75Ca ⁺² + 1.75Al ⁺³ + 2.25SiO ₂ (aq) + 3.5H ₂ O	<i>Id.</i>	-4.1151	-6.8646	-9.0284	-10.9189
	<i>Aa.</i>	-4.2918	-7.0414	-9.2052	-11.0956
	<i>Nw.</i>	-3.9530	-6.7463	-8.9439	-10.8612
Ab20An80 + 7.2H ⁺ = 0.20Na ⁺ + 0.80Ca ⁺² + 1.80Al ⁺³ + 2.20SiO ₂ (aq) + 3.6H ₂ O	<i>Id.</i>	-4.1371	-7.0178	-9.2953	-11.2819
	<i>Aa.</i>	-4.2990	-7.1798	-9.4573	-11.4439
	<i>Nw.</i>	-3.9976	-6.9173	-9.2249	-11.2353
Ab15An85 + 7.4H ⁺ = 0.15Na ⁺ + 0.85Ca ⁺² + 1.85Al ⁺³ + 2.15SiO ₂ (aq) + 3.7H ₂ O	<i>Id.</i>	-4.1522	-7.1642	-9.5554	-11.6381
	<i>Aa.</i>	-4.2933	-7.3053	-9.6964	-11.7792
	<i>Nw.</i>	-4.0432	-7.0876	-9.5037	-11.6062
Ab10An90 + 7.6H ⁺ = 0.10Na ⁺ + 0.90Ca ⁺² + 1.90Al ⁺³ + 2.10SiO ₂ (aq) + 3.8H ₂ O	<i>Id.</i>	-4.1586	-7.3019	-9.8067	-11.9856
	<i>Aa.</i>	-4.2709	-7.4141	-9.9190	-12.0978
	<i>Nw.</i>	-4.0875	-7.2545	-9.7776	-11.9710
Ab05An95 + 7.8H ⁺ = 0.05Na ⁺ + 0.95Ca ⁺² + 1.95Al ⁺³ + 2.05SiO ₂ (aq) + 3.9H ₂ O	<i>Id.</i>	-4.1525	-7.4271	-10.2531	-12.3205
	<i>Aa.</i>	-4.2240	-7.4985	-10.1170	-12.3920
	<i>Nw.</i>	-4.1235	-7.4110	-10.0395	-12.3225

3.5 Reactive fluid flow

The coupled reaction and transport equation for the conservation of mass of a solute species can be expressed as (Steefel, 1993)

$$\frac{\partial(\phi C_j)}{\partial t} + \nabla \cdot (u C_j - D \nabla C_j) = R_j \quad (j = 1, \dots, N_c) \quad (3.6)$$

where ϕ is the porosity, C_j is the total concentration of the j^{th} species, u is the Darcian fluid flux, D is the combined dispersion/diffusion coefficient and R_j is the total amount of the heterogeneous mineral-fluid reactions affecting the concentration of j^{th} species in solution. One such partial differential equation has to be written for each thermodynamic component. N_c is the total number of components. The total concentration is the sum of concentrations of species in the fluid phase multiplied by the stoichiometry of component j . Equation 6, when implemented with a suitable numerical algorithm, provides a tool to model the processes that involve chemical reactions and fluid transport in geologic media. The Darcian flux has to be defined at any given point within the modeling domain.

For the fluid-rock interaction simulations we used the one dimensional multicomponent reactive fluid transport code 1DREACT (Steefel, 1993; Steefel and Lasaga, 1994) which is based on an integrated finite difference formulation of Equation 3.6 that solves for aqueous species concentrations, calculates mineral precipitation/dissolution rates, saturation states and mineral volumes. A thermodynamic database as well as initial and boundary conditions are required to obtain a closure of the equation systems.

3.6 The test case

The modeling domain consists of a porous column of 5mm length with two zones: zone A contains 70% albite and zone B 70% anorthite, each with a total porosity of 30% to prevent the system from clogging (Fig. 3.3). The artificially high porosity was found to be necessary, since at this point we are not able to model expansion or constriction of our modeling domain, a feature to be included in future calculations. The pore spaces were filled with a fluid and the system was kept at 2.5 kbar and 500 °C. A very fine discretization of the grid was needed in the contact zone, to prevent numerical instability and artifacts at the contact of the two mineral zones due to intense mineral-fluid reactions in its vicinity. The initial fluid composition in the albite zone was taken to be in equilibrium with the pelitic assemblage of quartz-andalusite-albite. Similarly the fluid composition in anorthite zone was assumed to be in equilibrium with the quartz-

andalusite-anorthite assemblage. Generally fluids at these metamorphic temperatures and pressures are chloride-rich brines (Eugster and Baumgartner, 1987), and hence the chemical speciation of the system was calculated with a 1 molar chlorine solution using the geochemical speciation model SOLUB (Roselle and Baumgartner, 1995). Experimental studies by Hauenberger et al., (2001) and Pak et al., (2003) provide examples for the speciation in supercritical fluids in equilibrium with pelitic mineral assemblages. They suggest that depending on the chloride concentration, associated alkali metal chloride species to dominate at these supercritical conditions. Aluminum has a great tendency to form hydroxide complexes such as $\text{Al}(\text{OH})_4^-$ and $\text{Al}(\text{OH})_2^+$ at high temperatures and pressures (Eugster and Baumgartner, 1987; Walther, 1997) and can be considered as the dominant Al species. Table 3.2 gives the initial aqueous species concentrations obtained for the model grid together with the thermodynamic constraints used.

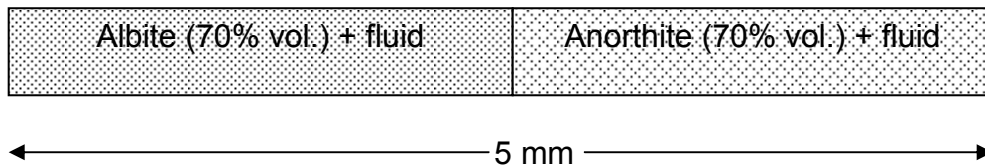


Figure 3.3. Schematic diagram of the one-dimensional model grid used in the test case. Pressure was kept at 2.5 kbar and temperature at 500 °C.

Table 3.2. Initial aqueous species concentrations distributed in mineral zones at 500 °C and 2.5 kbar, and the constraints used to buffer them.

Component	Concentration (mol/kg w)			
	Albite zone	Constraint	Anorthite zone	Constraint
H^+	3.881×10^{-5}	Charge balance	7.148×10^{-4}	Charge balance
Cl^-	5.584×10^{-1}	Total chlorine concentration	3.031×10^{-1}	Total chlorine concentration
Al^{+3}	5.305×10^{-16}	Andalusite equilibrium	1.633×10^{-12}	Andalusite equilibrium
Ca^{+2}	7.091×10^{-5}	Total calcium concentration	4.988×10^{-2}	Anorthite equilibrium
Na^+	5.578×10^{-1}	Albite equilibrium	6.501×10^{-4}	Total sodium concentration
$\text{SiO}_2(\text{aq})$	7.800×10^{-2}	Quartz equilibrium	7.800×10^{-2}	Quartz equilibrium

The transport of solutes was assumed to be only due to diffusion. A diffusion coefficient of $1 \times 10^{-12} \text{ m}^2 \text{ s}^{-1}$ was assigned for all solute species. We used this low value to maintain the equilibrium between minerals and the fluid during simulation time. Fast reaction rates were necessary to keep the system at equilibrium. A value of $1 \times 10^{-2} \text{ mole/m}^2 \text{ s}$, was found to be fast enough to maintain equilibrium. Hence this rate was used for all mineral phases. For the reactive surface areas of primary minerals a value of $5000 \text{ m}^2 / \text{m}^3$ (rock) was assigned while $1000 \text{ m}^2 / \text{m}^3$ (rock) was used for secondary minerals, to account for initial small grain size.

3.7 Results and discussion

Ideal, molecular mixing model

Ideal molecular mixing model for a solid solution assumes that the activity of a pure end member phase is equal to its mole fraction. Hence for an intermediate composition of the plagioclase solid solution, Equation 3.5 takes the form

$$\log K_{plag} = X_{ab} \log K_{an} + X_{an} \log K_{an} + X_{ab} \log X_{ab} + X_{an} \log X_{an} \quad (3.7).$$

A thermodynamic database containing the $\log K$'s calculated using Equation. 3.7 for dissolution reactions of plagioclase pseudo compounds, together with other minerals and aqueous species is given for the pseudo compounds in Table 3.1. Results show that albite and anorthite dissolve at the boundary, while all intermediate compositions start to precipitate in the contact zone. The phases precipitate in order of increasing anorthite mole fraction forming a smooth compositional change between the albite and anorthite zones (Fig. 3.4). Albite and anorthite migrate in opposite directions giving way to precipitating intermediate phases. The new phases occur in different proportions on either side of the contact zone with positive and negative solid volume changes. Relatively slow diffusion of aluminum is the result of low Al-concentrations, resulting in a smaller Al-flux. Hence aluminum is relatively immobile, leading to a larger precipitation of intermediate phases in the original anorthite zone. This increases the solid amount, decreasing the porosity (Fig. 3.5). Solid volume is lost in the original albite zone. Overall, the solid volume in the diffusion zone decreases.

Solubility differences in the highly charged, small aluminum and silica ions result in different migration rates of solute species which in turn affect the spatial distribution of precipitating intermediate plagioclase phases. Higher Na fluxes, compared to that of Ca, as well as higher Si fluxes as compared to Al lead to an asymmetric distribution of diffusion profiles around the initial contact of albite and anorthite. A minor amount of

quartz forms in the albite zone restricted to a narrow region. This is the result of increased diffusional fluxes of sodium and plagioclase stoichiometry. Any increase in Ca in plagioclase requires that aluminum is added, while silica concentration in plagioclase is reduced.

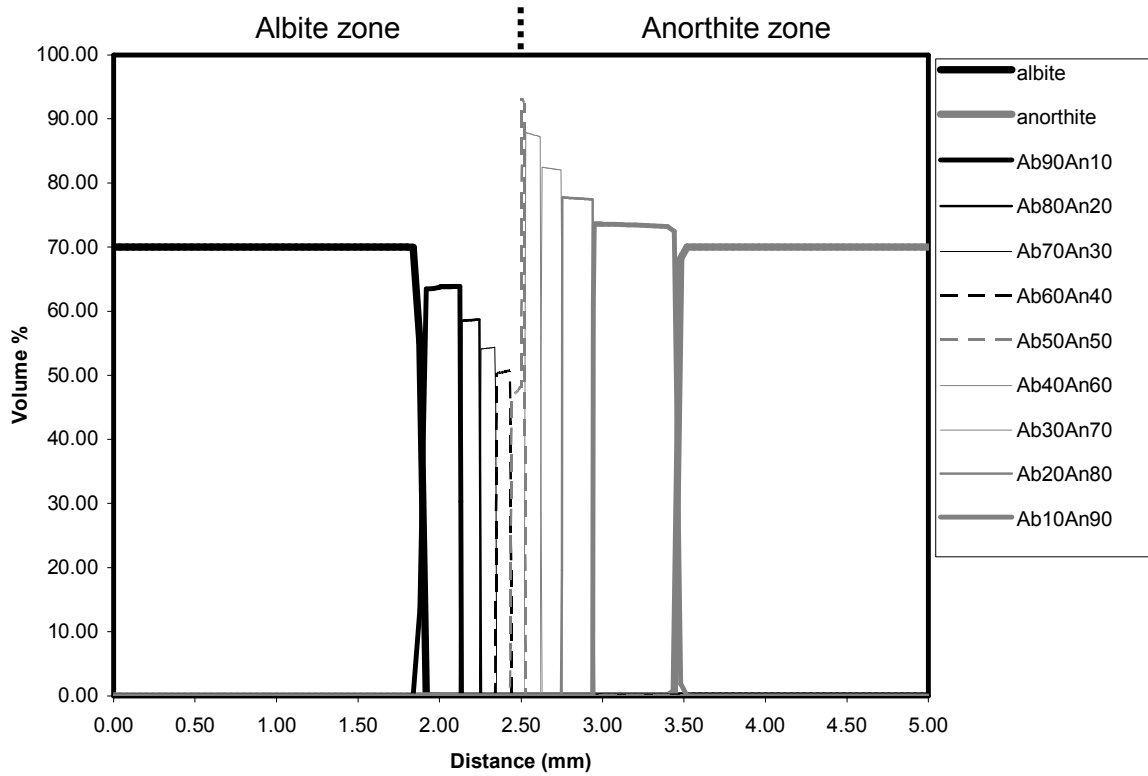


Figure 3.4. Diffusional profiles of intermediate plagioclase phases develop in between initial albite and anorthite zones. Anorthite is replaced faster than albite by intermediate compositions indicating faster diffusion of Na into anorthite zone. Nine pseudo compounds have been used in the simulation.

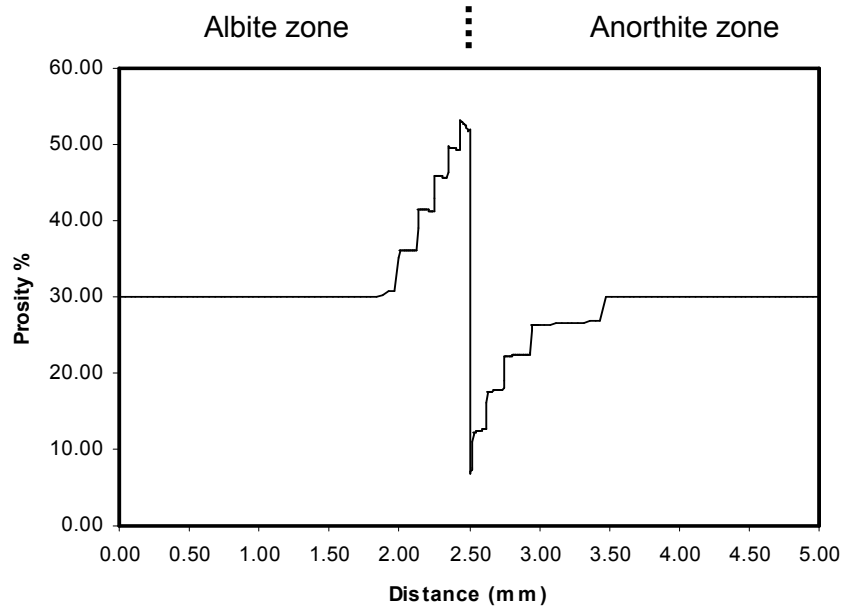


Figure 3.5. Change of porosity along the model grid.

The width of this alteration zone, however, is not solely a result of the extent of diffusion of solutes, but depends also on the reaction rate (Lichtner (1988), Steefel and Lichtner, 1998). According to their formulation, the equilibration length scale, λ , takes the form

$$\lambda = \sqrt{\frac{\phi D}{k'}} \quad (3.8)$$

where k' represent the product of intrinsic rate constant and reactive surface area. If this value is significantly larger than the crystal size, disequilibrium is present. The parameters used in our simulations yield a value of $1.73 \mu\text{m}$ for λ , which is fairly small compared to the diffusion distance in Fig. 3.4. This affects the shape of the dissolution fronts: all zone boundaries between phases are sharp. Only minor overlap of the phases at the zone boundaries occurs as is expected for simulations which maintain (approximately) local equilibrium. A single phase occupies a given segment of the domain as required by thermodynamic equilibrium constraints in this system.

Several calculations with varying numbers of pseudo compounds yield a similar distribution for the reaction zone. In each case all the included intermediate compositions of the plagioclase solid solution precipitate. More pseudo compounds lead to a smoother variation of the anorthite mole fraction along the column. To compare the results, we

assigned the middle of each zone the composition of the pseudo compound that precipitated, and plotted the resulting profiles in Fig. 3.6. The largest difference is the perceived width of the reaction zone as a function of the number of pseudo compounds, as can be seen by the tails of the curves in Figure 3.6. With as few as 9 intermediate phases the same curve is obtained as for 39 intermediate phases. This illustrates that pseudo compounds can be a very efficient approach to modeling solid solution in transport systems.

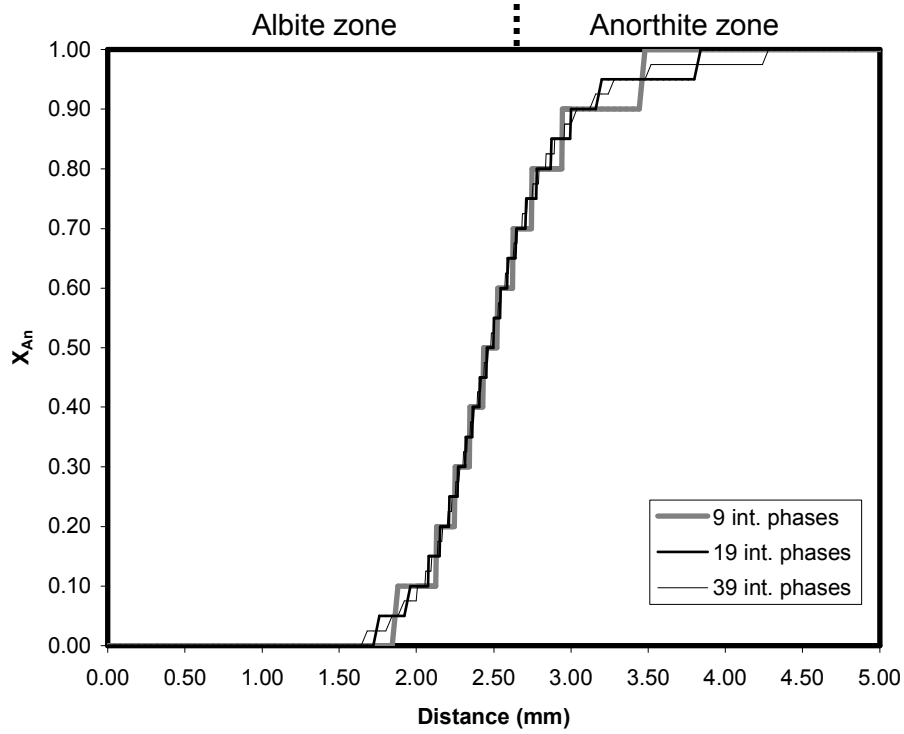


Figure 3.6. Variation of anorthite mole fraction along the model grid for three simulations using 9, 19 and 39 intermediate phases of plagioclase using ideal, molecular model.

Al-avoidance plagioclase mixing model

The Gibb's free energy of mixing in plagioclase solid solution using the Al-avoidance model of Kerrick and Darken (1975; Fig. 3.2) can be calculated from:

$$\Delta G_{plag}^{mixing} = RT \left\{ X_{ab} \ln [X_{ab}^2 (2 - X_{ab})] + X_{an} \ln \left[\frac{X_{an} (1 + X_{an})^2}{4} \right] \right\} \quad (3.9)$$

where the $[X_{ab}^2(2-X_{ab})]$ and $[^{1/4}X_{an}(1+X_{an})^2]$ terms are the activities of albite and anorthite in the pseudo compound of interest. $\text{Log}K$'s of dissolution reactions of plagioclase pseudo compounds using the Al-avoidance model were obtained by substituting these activity values into Equation 3.5. Similar to the ideal model case, a database was generated for transport calculations (Table 3.1). All intermediate phases precipitate, and the generalizations discussed for the ideal model are not significantly changed (Fig. 3.7). The number of intermediate phases does not significantly affect the solution obtained. Figure 3.8 shows the change of anorthite mole fraction for the Al avoidance model in comparison with that of the ideal molecular mixing model. The thermodynamically more complex model is not significantly different.

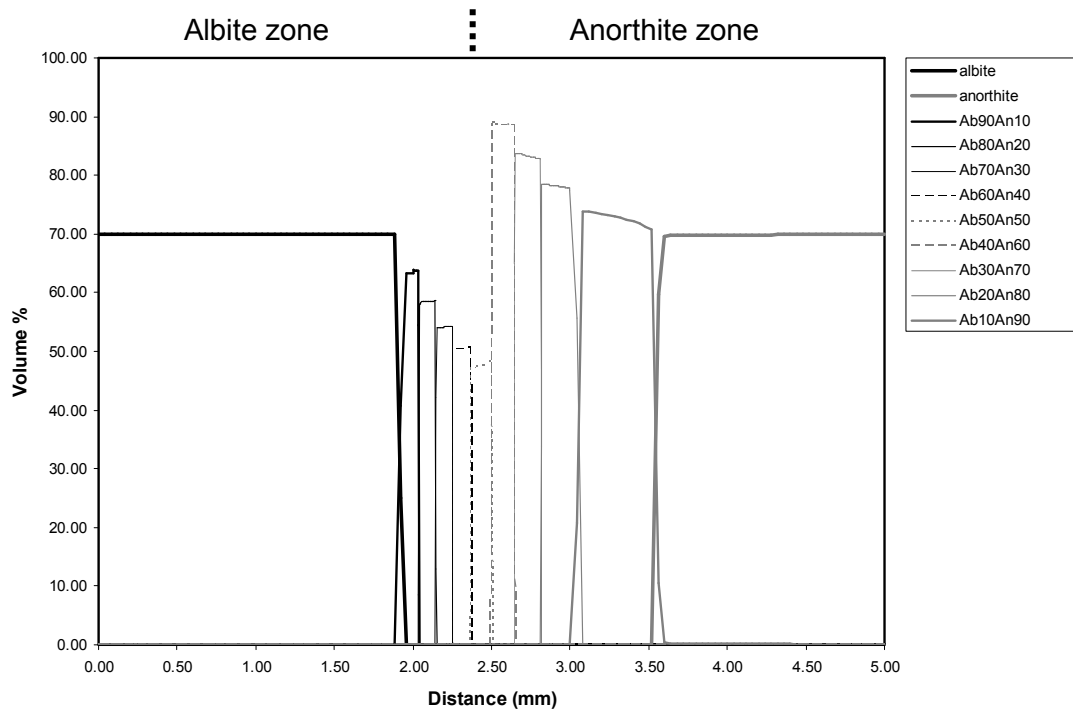


Figure 3.7. Pseudo compound distribution along the model grid as calculated using Al-avoidance model.

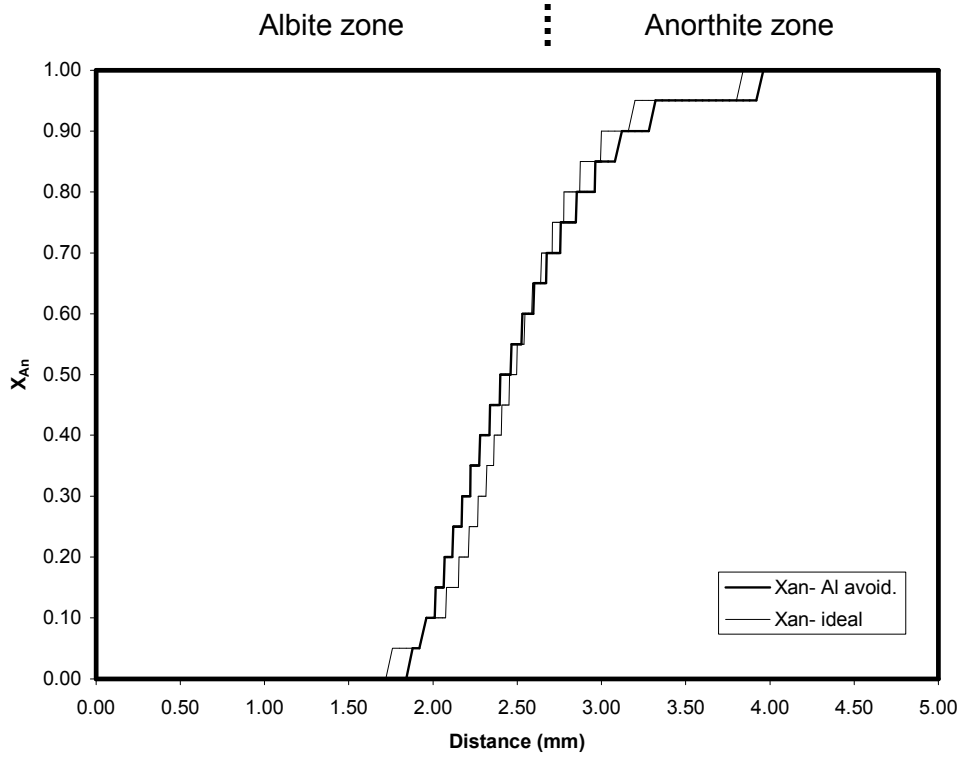


Figure 3.8. Comparison of the distribution of anorthite mole fraction between ideal, molecular model and Al-avoidance model.

Non-ideal, Al-avoidance mixing model

Newton et al., (1980) presented a non-ideal plagioclase mixing model based on experiments on the enthalpies of solution of high-structural state plagioclase. They derived a relationship for the excess enthalpy of mixing at 970 K which is:

$$\Delta H^{ex} (\pm 0.16 \text{kcal}) = 6.7461 X_{ab} X_{an}^2 + 2.0247 X_{an} X_{ab}^2 \quad (3.10)$$

Combining this excess enthalpy of mixing together with the free energy of mixing of the Al-avoidance model (Eqn. 3.11) yields an expression for a non-ideal mixing model for high structural state plagioclase:

$$\Delta G_{plag}^{nonid.mx} = 6.7461 X_{ab} X_{an}^2 + 2.0247 X_{an} X_{ab}^2 + RT \left\{ X_{ab} \ln [X_{ab}^2 (2 - X_{ab})] + X_{an} \ln \left[\frac{X_{an} (1 + X_{an})^2}{4} \right] \right\} \quad (3.11)$$

They postulate the entropy and enthalpy of mixing to be nearly independent of temperature. Therefore we used the same expression to derive the free energy of mixing at temperatures from 400 °C to 700 °C. Figure 3.9 shows the free energy curves calculated using Equation 3.11 at different temperatures. A mixing gap appears at 500 °C and it widens with decreasing temperature. Log K of the dissolution reaction of an intermediate plagioclase composition using the non-ideal mixing model of Newton et al., (1980) can be calculated from:

$$\log K_{plag} = X_{ab} \log K_{an} + X_{an} \log K_{ab} + (6.7461X_{ab}X_{an}^2 + 2.0247X_{an}X_{ab}^2) + RT \left\{ X_{ab} \ln [X_{ab}^2 (2 - X_{ab})] + X_{an} \ln \left[\frac{X_{an} (1 + X_{an})^2}{4} \right] \right\} \quad (3.12)$$

A thermodynamic database containing $\log K$'s of mineral and aqueous species reactions, as before, was generated for fluid-rock interaction calculations. Simulations were carried out at 2.5 kbar for temperatures from 400 °C to 700 °C at 100 °C intervals. The calculated diffusion profiles using 19 plagioclase pseudo compounds are shown in Figure 3.10 for a simulation at 500 °C. The mixing gap is clearly shown in Figure 3.11 for calculations at temperatures at and below 500°C. The non-ideality has a strong influence on the shape of the plagioclase composition profile (Fig. 3.11).

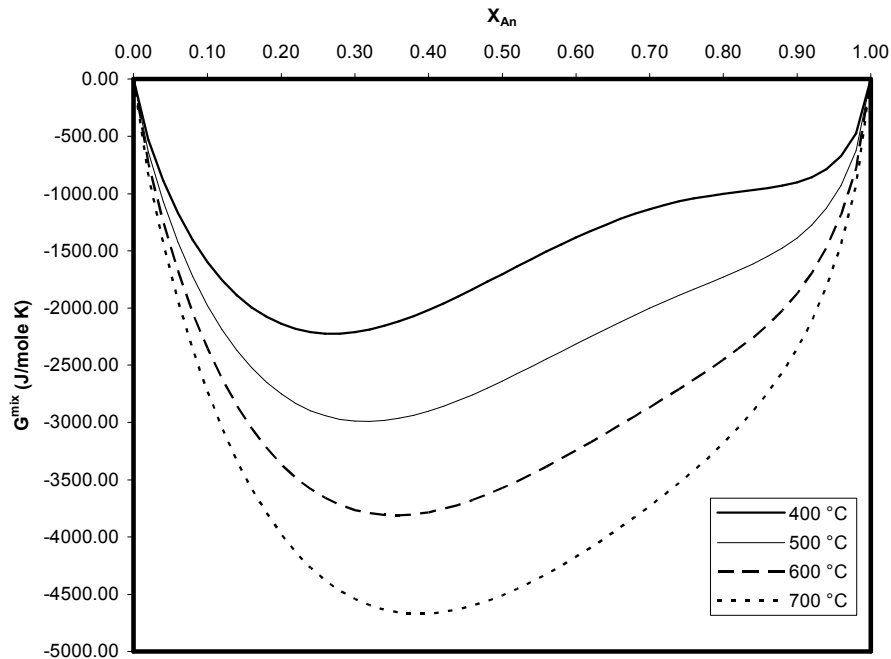


Figure 3.9. Gibb's free energy of mixing of high structural plagioclases at 400, 500, 600 and 700 °C using the non-ideal mixing model of Newton et al., (1980).

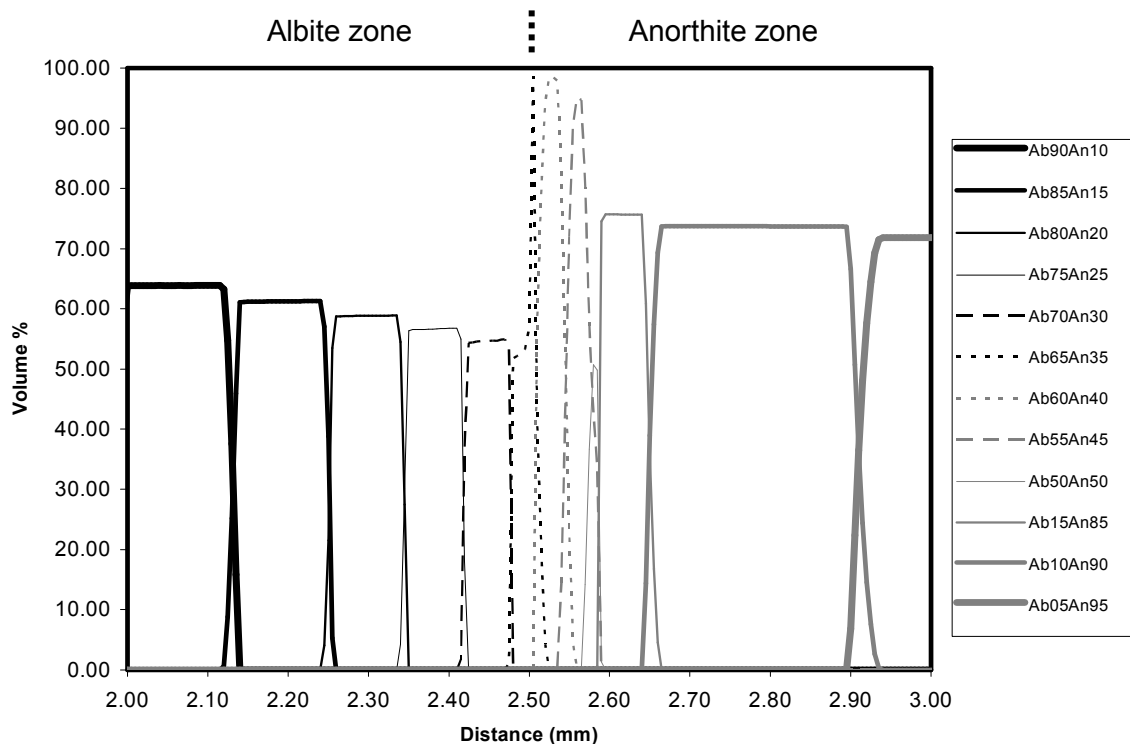


Figure 3.10. Diffusional profiles for plagioclase solid solution developed between albite and anorthite when Newton et al.'s model is used. Note the mixing gap between $0.50 < X_{An} < 0.85$. The diagram shows only a 1 mm long segment of the model domain at the initial contact zone between albite and anorthite.

A natural example

A plagioclase compositional profile from a metasomatic zone from the Ademello contact aureole, northern Italy, is included here to show the systematic variation of anorthite mole fraction in plagioclase across a marl layer in a carbonate rock of the Calcare di Angelo formation (Fig. 3.12). The compositional profile formed due to diffusion of sodium and silica into the marly layer (Baumgartner et al., 1989). Silica and sodium in turn were derived from igneous fluids which percolate along the surface of the carbonate-marl contact. The profile displays three compositional jumps, indicating at least three mixing gaps. While the principle features of the natural diffusion profile are modeled by non-ideal case (Fig. 3.11), it is clear that the thermodynamic model of Newton et al., (1980) is too simple to adequately describe the observed data. A model including the structural changes in the plagioclase series is needed here, as was discussed by Carpenter (1994).

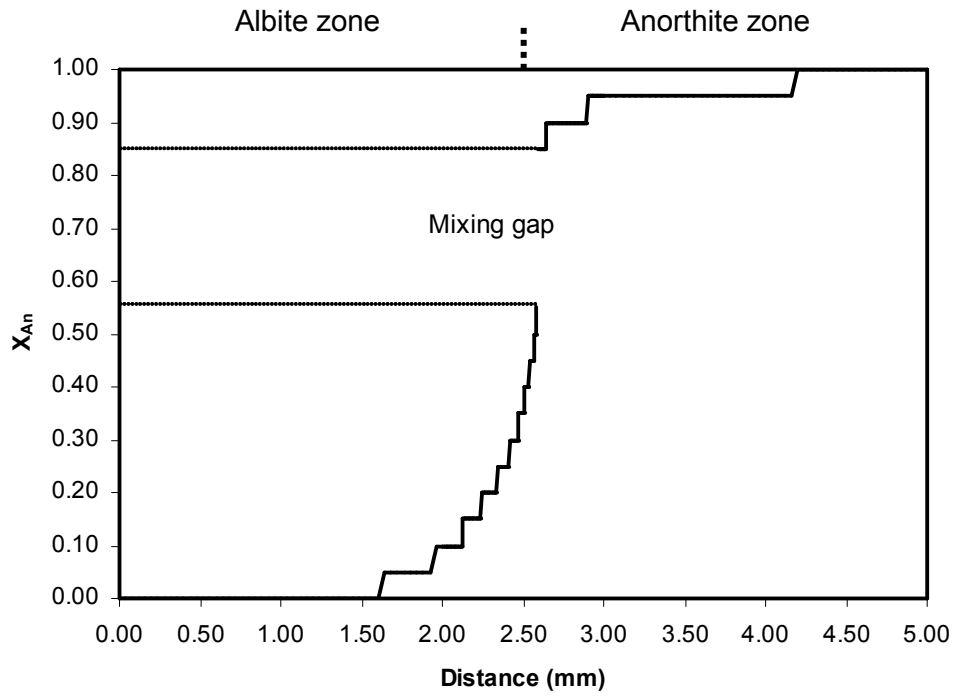


Figure 3.11. Anorthite mole fraction along the model grid obtained using non-ideal mixing model of Newton et al., (1980). A mixing gap is produced between $0.50 < X_{An} < 0.85$ at 500 °C.

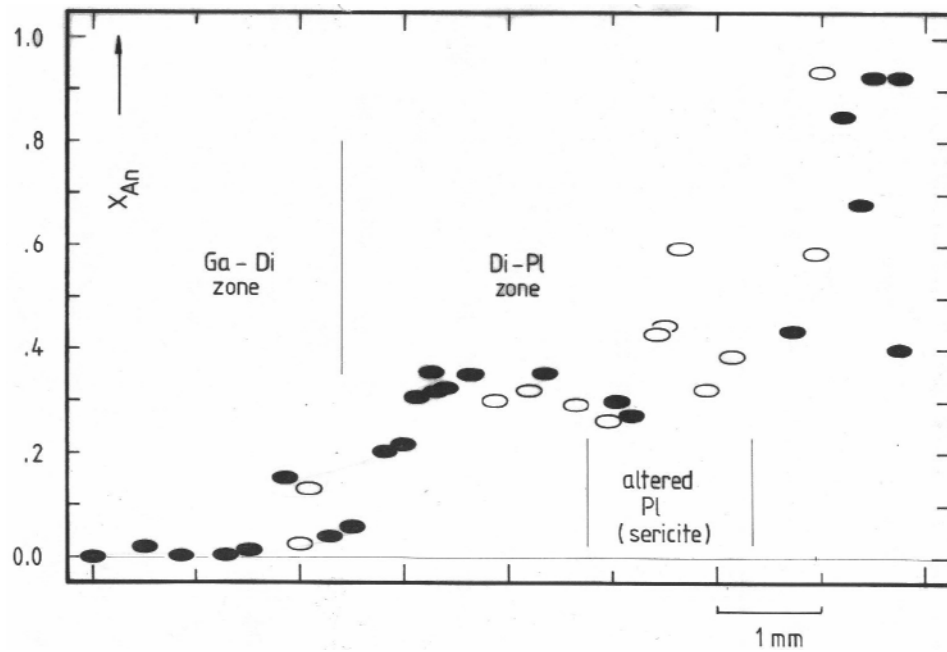


Figure 3.12. Two compositional profiles (filled and blank ovals) across a vein in a metasomatic zone of Adamello Contact Aureole.

3.8 Conclusion

The use of pseudo compounds in reactive transport modeling is very promising. It was possible to model with as little as 9 additional phases binary solid solutions. Several different mixing models can be tested easily, without any modification of the transport code. Modifications are on the level of the thermodynamic input data only. Our calculations illustrate the sensitivity of the obtained mineralogical profiles to the mixing models used. Since most mineral phases actually do form solid solutions at high temperatures, including such important phases as mica, feldspars, amphiboles, garnet and pyroxenes, it is crucial to include these solid solution phases in any mass transport calculation.

References

- Baumgartner, L.P., Gieré, R., Trommsdorff, V. and Ulmer, P., 1989. Field guide for the southern Adamello. In: Trommsdorff, V., Gieré, R., Baumgartner, L.P., (eds), Rock-fluid interaction in crystalline basements. III Summer School di Geologia e Petrologia dei basamenti cristallini, Siena. 91-115.
- Baumgartner, L.P., and Ferry, J.M., 1991. A model for coupled fluid-flow and mixed-volatile mineral reactions with applications to regional metamorphism. *Contrib. Mineral. Petrol.* 106, 273-285.
- Carpenter, M.A., 1994. Subsolidus phase relations of the plagioclase feldspar solid solution. In: Parson, I. (ed), *Feldspars and their reactions*. NATO ASI Series, 221-269.
- Carpenter, M.A., and Ferry, J.M., 1984. Constraints on the thermodynamic mixing properties of plagioclase feldspars. *Contrib. Mineral. Petrol.* 87, 138-148.
- Carpenter, M.A., and McConnell, J.D.C., 1984. Experimental delineation of the $C1 = I1$ transformation in intermediate plagioclase feldspars. *American Mineralogist* 69, 112-121.
- Connolly, J.A.D., 1990. Multivariable phase diagrams: An algorithm based on generalized thermodynamics. *Am. J. Sci.*, 290, 666-718.
- Connolly, J.A.D. and Petrini, K., 2002. An automated strategy for calculation of phase diagram sections and retrieval of rock properties as a function of physical conditions. *J. Met. Geol.* 20, 697-708.
- Eugster, HP and Baumgartner, LP (1989). Mineral solubilities and speciation in supercritical metamorphic fluids. In: Carmichaels, I.S.E., Eugster, H.P. (Eds), *Thermodynamic modeling of geological materials: Minerals, fluids and melts*. Mineralogical Society of America. *Reviews in Mineralogy.* 17, 367-403.

- Hauzenberger, C.A., Pak, T.M., and Baumgartner, L.P., 2001. Experimental study on the “model”-pelite mineral assemblage albite+K-feldspar+andalusite+quartz in supercritical chloride rich aqueous solutions at 0.2 GPa and 600 °C. *Geochim. Cosmochim. Acta* 65, 4493-4507.
- Helgeson, H.C., Lichtner, P.C., 1987. Fluid flow and mineral reactions at high temperatures and pressures. *J. Geol. Soc. Lond.* 144, 313-326.
- Holland, T., and Powell, R., 1992. Plagioclase feldspars: Activity-composition relations based upon Darken’s quadratic formalism and Landau theory. *American Mineralogist* 77, 53-61.
- Holland, T., and Powell, R., 2003. Activity-composition relations for phases in petrological calculations: an asymmetric multicomponent formulation. *Contrib. Mineral. Petrol.* 145, 492-501.
- Johnson, JW, Oelkers, EH, and Helgeson, HC (1992). *Computers & Geosciences*, 18(7), 899-947.
- Kerrick, D.M., and Darken, L.S., 1975. Statistical thermodynamic models for ideal oxide and silicate solid solutions, with application to plagioclase. *Geochim. Cosmochim. Acta* 39, 1431-1442.
- Lasaga, A.C., 1984. Chemical kinetics of water-rock interactions. *J. Geophys. Res.* 89, 4009-4025.
- Lichtner, P.C., 1985. Continuum model for simultaneous chemical reactions and mass transport in hydrothermal systems. *Geochim. Cosmochim. Acta* 49, 779-800.
- Lichtner, P.C., 1988. The quasi-stationary state approximation to coupled mass transport and fluid-rock interaction in a porous medium. *Geochim. Cosmochim. Acta* 52, 143-165.
- Lichtner, P.C., 1996. Continuum formulation of multicomponent-multiphase reactive transport. *Reviews in Mineralogy*, 34, 1-79.
- Newton, R.C., Charlu, T.V., and Kleppa, O.J., 1980. Thermochemistry of the high structural state plagioclase. *Geochim. Cosmochim. Acta* 44, 933-941.
- Oelkers, E.H., Helgeson, H.C., Shock, E.L., Sverjensky, D.A., Johnson, J.W., and Pokrovskii, V.A., (1995). Summary of the apparent partial standard partial molal Gibbs free energies of formation of aqueous species, minerals and gases at pressures 1 to 5000 bars and temperatures 25 to 1000 degrees C. *J. Phys. Chem. Ref. Data* 24, 1401-1560.
- Orville, P.M., 1972. Plagioclase cation exchange equilibria with aqueous chloride solution. Results at 700 °C and 200 bars in the presence of quartz. *Am. J. Sci.* 272, 234-272.
- Pak, T.M., Hauzenberger, C.A., and Baumgartner, 2003. Solubility of the assemblage albite+K-feldspar+andalusite+quartz in supercritical aqueous chloride solutions at 650 °C and 2 kbar. *Chemical Geology* (in press).

- Reed, M.H., 1982. Calculation of multicomponent chemical equilibria and reaction processes in systems involving minerals, gases and an aqueous phase. *Geochim. Cosmochim. Acta* 46, 513-528.
- Roselle, G.T. and Baumgartner, L.P., 1995. Experimental determination of anorthite solubility and calcium speciation in supercritical chloride solutions at 2 kb from 400 to 600°C. *Geochim. Cosmochim. Acta* 59, 1539-1549.
- Schliestedt, M., and Johannes, W., 1990. Cation exchange equilibria between plagioclase and aqueous chloride solution at 600 to 700°C and 2 to 5 kbar. *Eur. J. Mineral.* 2, 283-295.
- Steeffel, C.I., 1993. 1DREACT User Manual.
- Steeffel, C.I., Lasaga, A.C., 1994. A coupled model for transport of multiple chemical species and kinetic precipitation/dissolution reactions with applications to reactive flow in single phase hydrothermal system. *Am. J. Sci.* 294, 529-592.
- Steeffel, C.I., Lichtner, P.C., 1998. Multicomponent reactive transport in discrete fractures, I. Controls on reaction front geometry. *J. Hydrol.* 209, 186-199.
- Walther, J.V., 1997. Experimental determination and interpretation of the solubility of corundum in H₂O between 350° and 600 °C from 0.5 to 2.2 kbar. *Geochim. Cosmochim. Acta* 61, 4955-4964.

Reactive Fluid Transport Modeling of Metasomatism of Late Paleoproterozoic Sedimentary Rocks in the Southern Lake Superior Region

ABSTRACT

Field observations reveal that quartz-pyrophyllite (or kaolinite) bearing assemblages have been transformed into muscovite-pyrophyllite-diaspore bearing assemblages due to action of fluids migrating along permeable flow channels. Such hydrothermal alteration of Paleoproterozoic sedimentary rocks in the Southern Lake Superior region was modeled with a reactive fluid transport code. Fluid-rock interaction modeling with an initial qtz-prl assemblage and a K-rich fluid simulates the formation of observed mineralogical transformation within 1 Ma. Simulations show that reactions due to only up-temperature fluid flow are responsible for this alteration. The bulk composition of the system evolved from an SiO₂-rich to SiO₂-undersaturated and Al₂O₃+K₂O-rich. The compositional evolution of the system predicted by flow along a negative temperature gradient is inconsistent with the observed mineral paragenesis, which is SiO₂-poor. Tests with several different fluid compositions show that interaction of K-rich hydrothermal fluids with qtz-klm sedimentary rocks is the most likely cause for metasomatism. It is postulated that fluid circulation took place under convection as a result of the thermal flux provided by regional scale granitic magmatism. Muscovite formation, which has been dated at ca. 1465 Ma, is attributed to the K-metasomatism.

4.1 Introduction

Well developed paleosol (saprolite) is present at several localities beneath the supermature quartzites of the Baraboo Interval (1630-1750Ma; Dott, 1983; Medaris et al., 2003). They have been important elements in unraveling the Proterozoic evolution of the Lake Superior region. Recent investigations of the Baraboo quartzites have demonstrated K-metasomatism of the saprolites and certain stratigraphic units in the quartzites due to fluids, which were probably migrating on a continental scale. Quartz-pyrophyllite or quartz-kaolinite bearing assemblages have been transformed in saprolite into quartz-muscovite bearing assemblages and in pelite and siltstone into muscovite-pyrophyllite-diaspore bearing assemblages (Medaris et al., 2003; Fig. 4.1). The metasomatised sedimentary rocks in the Sioux Quartzite, which contain the assemblage ms-prl-dsp, have been quarried for centuries by Native Americans as pipestone, a.k.a catlinite, for the

production of ceremonial pipes and other artifacts. In this paper we use a one-dimensional multi-component reactive fluid transport model to constrain the alteration of the Sioux pipestone of the Baraboo Interval to identify the nature of fluids, flow directions, and to test the presence of a possible regional flow event.

4.2 Geological setting

Late Paleoproterozoic quartzites of the southern Lake Superior region rest unconformably on Archean basement, geon 18 Penokean basement and geon 17 granite and rhyolite. They represent a once southward thickening wedge of clastic strata deposited on a stable craton of subdued topography under a warm, humid climate. There is evidence for later marine transgression yielding deeper marine sediments. Supermaturity of these quartz arenites is reflected by the absence of feldspars, common occurrence of kaolinite or pyrophyllite, and rarity of detrital muscovite. A well developed paleosol, with a thickness of 10-20 m, is present beneath the quartzites. The saprolite protolith beneath the Sioux Quartzite is Archean granite and gneiss, beneath the Barron Quartzite, Penokean tonalite, and beneath the Baraboo quartzite, geon 17 granite and rhyolite. Deposition of the quartzites is constrained to be post- the underlying 1754 Ma Baxter Hallow granite, but before the 1630 Ma metamorphism which affected a large part of the area (Medaris et al., 2003).

Granitic magmas were emplaced on a continental scale in a belt across North America in Neoproterozoic time (Anderson, 1983), including the 1465 Ma Wolf River batholith in east-central Wisconsin (Anderson and Cullers, 1978). A tectonothermal event overprinted much of the area around 1630 Ma (Rb/Sr and $^{40}\text{Ar}/^{39}\text{Ar}$ cooling ages of amphiboles and micas; Holm et al., 1998). Medaris et al. (2003) have evaluated the metamorphic conditions for Baraboo Interval quartzites from phase petrology relations in the system $\text{K}_2\text{O}-\text{Al}_2\text{O}_3-\text{SiO}_2-\text{H}_2\text{O}$ (KASH; Fig. 4.2). Unmetasomatized quartzites north of the 1630 Ma tectonothermal front contain qtz-kln, and those south of the front contain qtz-prl, which is stable between 285°C and 350°C at 1 kbar pressure and unit activity of H_2O .

The Barron Quartzite and underlying saprolite (Fig. 4.1) lie outside the thermally affected area. They have retained their original mineralogies and compositions and thus provide the archetype for the late Paleoproterozoic sedimentary rocks and paleosols of the region. Rb/Sr whole-rock isochron yields apparent ages of 1336 ± 75 Ma for K-metasomatized saprolites within the 1630 Ma thermal front. Thus the K metasomatism has taken place later than the time of formation of saprolites, as well as 1630 Ma metamorphism. The regional hydrothermal metasomatism is most likely linked to the Neoproterozoic continental scale granitic magmatism, represented locally by the Wolf River batholith.

Hydrothermal fluids could have migrated along permeable flow channels along the basement - quartzite contact and stratigraphic levels within the quartzites, thereby introducing K to the paleosols and locally transforming the sedimentary rocks (qtz-kln or qtz-prl) to pipestone (ms-prl-dsp). Hence the muscovite-bearing assemblages could correspond to the age of presumed hydrothermal activity around 1460 Ma.

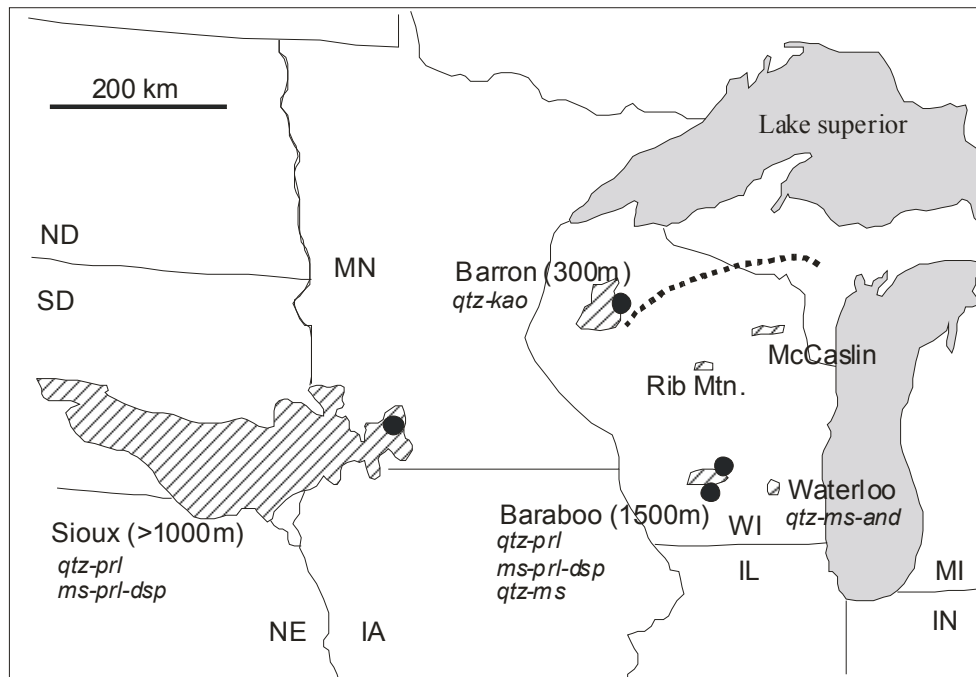


Figure 4.1. Distribution of Baraboo Interval quartzites in the Lake Superior region (hatched areas). Locality name of the quartzite occurrence is followed by average thickness given within brackets. Mineral assemblages are given in italicized letters. Dots indicate paleosol occurrences. 1630 Ma thermal and tectonic front is indicated with the thick broken line (from: Medaris et al., 2003).

We have performed a series of simulations using a coupled reactive transport code to investigate under which conditions a fluid circulating along permeable channels could change the chemistry of the quartz-bearing, potassium-deficient sedimentary rocks to the observed potassium-rich, SiO₂-undersaturated compositions of the pipestones. To this end we designed four models. Simulations were carried out for fluid recharge (up-temperature flow) and discharge (down-temperature flow) using different fluid compositions corresponding to basinal and hydrothermal fluids.

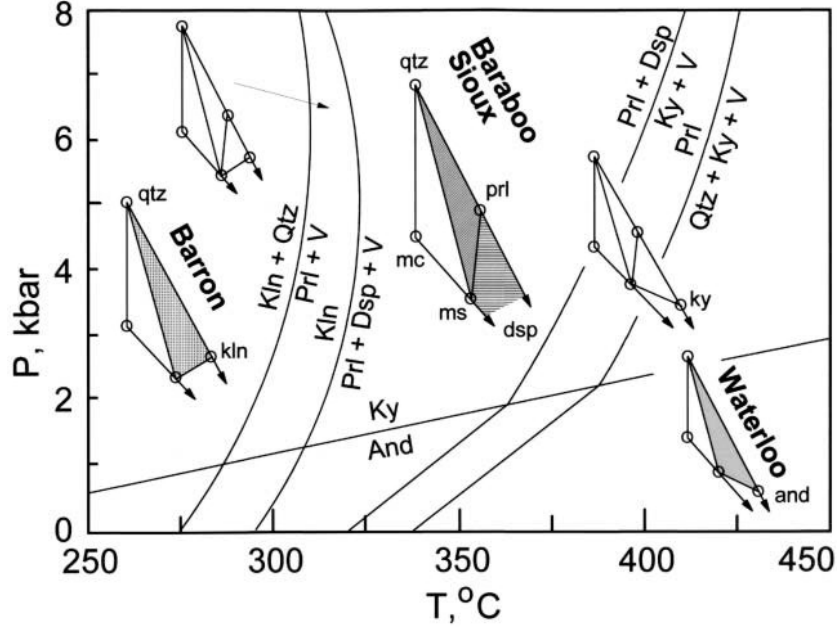


Figure 4.2. Stable mineral assemblages and reactions in the system KASH for Baraboo Interval quartzites (Medaris et al., 2003).

4.3 Reactive fluid transport modeling

Flow in porous media

The coupled reaction and transport equation for the conservation of mass of a solute species can be expressed as (Steefel, 1993).

$$\frac{\partial(\phi C_j)}{\partial t} + \nabla \cdot (u C_j - D \nabla C_j) = R_j \quad (j = 1, \dots, N_c) \quad (4.1)$$

where ϕ is the porosity, C_j is the total concentration of the j^{th} species, u is the Darcian fluid flux, D is the combined dispersion/diffusion coefficient and R_j is the total amount of the heterogeneous mineral-fluid reactions affecting the concentration of j^{th} species in solution. One such partial differential equation has to be written for each thermodynamic component. N_c is the total number of components. The total concentration is the sum of concentrations of species in the fluid phase multiplied by the stoichiometry of component j . Equation 4.1, when implemented with a suitable numerical algorithm, provides a tool to model the processes that involve chemical reactions and fluid transport in geologic

media. The Darcian flux has to be defined at any given point within the modeling domain.

For the fluid-rock interaction simulations we used the one dimensional multicomponent reactive fluid transport code 1DREACT (Steefel, 1993; Steefel and Lasaga, 1994) which is based on an integrated finite difference formulation of Eqn. 4.1 that solves for aqueous species concentrations, calculates mineral precipitation/dissolution rates, saturation states and mineral volumes. A thermodynamic database as well as initial and boundary conditions are required to obtain a closure of the equation systems.

Thermodynamic database

The thermodynamic database used in transport calculations contains logarithmic equilibrium constants ($\log K$'s) of reactions of aqueous species and minerals at different temperatures. They are written as hydrolysis reactions of one mole of mineral phase. To complete these data, a series of dissociation reactions is included for each additional aqueous ionic species. The only comprehensive dataset available for aqueous ions at the higher P-T conditions is the one associated with the SUPCRT92 computer program (Johnson et al., 1993). We used the data set of Oelkers et al., (1995), following the recommendations of Pak et al., (2003) and Hauzenberger et al., (2001). The most extensive thermodynamic dataset for minerals is that of Holland and Powell (1991, 1998). A restricted data set for aqueous species is available in this database, but the quality of the thermodynamic data for aqueous species has been questioned (eg: Pak et al., 2003; Hauzenberger et al., 2001). Therefore we choose the approach to combine the thermodynamic aqueous species data of Oelkers et al., (1995) with the mineral database of Holland and Powell (1991, 1998) to obtain more accurate $\log K$'s for mineral-fluid reactions. Gibb's free energies of formation of aqueous species were calculated using SUPCRT92 for a range of P-T conditions (450-1000 bar, 150 – 375 °C). Similarly those of minerals and H₂O were calculated using the program FrenDly from the Perplex program suite (Connolly and Petrini, 2002). The Gibb's free energy of a dissolution reaction for a mineral m is

$$\Delta G_r^{P,T} = \sum_i^{N_c} v_i \Delta G_{f,i}^{P,T} - (\Delta G_{f,m}^{P,T} + \Delta G_{f,H_2O}^{P,T}) \quad (i = 1, \dots, N_c) \quad (4.2)$$

where $\Delta G_{f,i}^{P,T}$ is the Gibb's free energy of formation of the i^{th} species in m at the pressure and temperature of interest, $\Delta G_{f,m}^{P,T}$ is that of the mineral, v_i is the stoichiometric coefficient of the i^{th} species in the reaction and N_c is the number of aqueous species in the reaction. The first term on the right hand side of Eqn. 4.2 is obtained from SUPCRT92 calculations and the second term from FrenDly. The $\log K$ of the reaction can then be

computed from $\Delta G_r^{P,T} = -2.303RT\log K$ where R is the gas constant and T is the absolute temperature. The thermodynamic database contains $\log K$ values at temperature intervals of 37.5 °C from 150 °C to 375 °C along a hydrostatic pressure gradient of 98 bar/km. 1DREACT interpolates the $\log K$'s using a simple polynomial function. Table 4.1 lists the mineral hydrolysis and aqueous species dissociation reactions, along with the obtained $\log K$ values used in the models. P-T dependent parameters for the Debye-Huckel equation were calculated following Helgeson and Kirkham (1974), and were fitted to the relevant pressure and temperature range of the model using a third order polynomial fit. Density of water was calculated using Perple_X program for a range of pressures and temperatures using the CORK equation of state of Holland and Powell (1991, 1998). A third order polynomial was introduced to the code to calculate water densities corresponding to the P-T conditions along the model grid.

The physical model

The saprolite zone occurs sandwiched between its protolith and the overlying quartzites at a basinal scale. It was assumed that the subsurface extension of the saprolite zone is inclined, and that it might have provided pathways for migrating fluids (Fig. 4.3). A 7500 m long section of the flow path was selected as the one-dimensional model domain. Temperatures at the two ends of the domain were set at 150 °C and 330 °C. They correspond to the temperatures at depths of 5 km and 11 km below the surface respectively, assuming a geothermal gradient of 30 °C/km. Fluid at the ends were kept at hydrostatic pressures of 490 bar and 980 bar respectively. The model grid has a uniform temperature gradient of 0.024 °C/m and a hydrostatic pressure gradient of 0.065 bar/m. It was discretized into 5 m segments for fluid transport calculations.

In groundwater environments fluids flow under pressure potential. Flow may also occur in convection cells due to density differences mainly caused by temperature gradients. Chemical reactions between fluid and rock changes the fluid composition leading to changes in its physical properties such as viscosity and density. This in turn affects the nature of flow. However, in a one-dimensional model the fluid flux-in has to correspond to the fluid flux-out, assuming the uptake or production of water to be negligible compared to the fluid flux. We used a constant fluid flux, with fluid flowing either down or up in 1DREACT.

Table 4.1. Mineral and aqueous species reactions and their log*K*'s used in simulations.

Reaction	Log <i>K</i>						
	150°C	187.5°C	225°C	262.5°C	300°C	337.5°C	375°C
<i>Aqueous species</i>							
$\text{Al(OH)}_2^+ + 2\text{H}^+ = \text{Al}^{+3} + 2\text{H}_2\text{O}$	5.2545	4.1082	3.1071	2.2155	1.4170	0.6968	0.0348
$\text{Al(OH)}^{+2} + \text{H}^+ = \text{Al}^{+3} + \text{H}_2\text{O}$	2.1120	1.4641	0.8854	0.3607	-0.1170	-0.5534	-0.9589
$\text{HSiO}_3^- + \text{H}^+ = \text{SiO}_2(\text{aq}) + \text{H}_2\text{O}$	8.6805	8.6014	8.6199	8.7100	8.8520	9.0308	9.2304
$\text{HCl}(\text{aq}) = \text{H}^+ + \text{Cl}^-$	0.4581	0.2296	-0.0390	-0.3398	-0.6653	-1.0121	-1.3750
$\text{KCl}(\text{aq}) = \text{K}^+ + \text{Cl}^-$	0.6745	0.4554	0.2417	0.0306	-0.1784	-0.3854	-0.5897
$\text{NaCl}(\text{aq}) = \text{Na}^+ + \text{Cl}^-$	0.2933	0.1162	-0.0688	-0.2615	-0.4583	-0.6585	-0.8594
$\text{NaAlO}_2(\text{aq}) + 4\text{H}^+ = \text{Na}^+ + \text{Al}^{+3} + 2\text{H}_2\text{O}$	13.7334	11.7513	10.0573	8.5848	7.2979	6.1664	5.1580
$\text{NaHSiO}_3(\text{aq}) + \text{H}^+ = \text{Na}^+ + \text{SiO}_2(\text{aq}) + \text{H}_2\text{O}$	7.5980	7.5648	7.5960	7.6704	7.7764	7.9024	8.0358
$\text{H}_2\text{O} = \text{H}^+ + \text{OH}^-$	11.4488	11.1026	10.8705	10.7219	10.6339	10.5901	10.5731
<i>Minerals</i>							
$\text{Albite} + 4\text{H}^+ = \text{Na}^+ + \text{Al}^{+3} + 3\text{SiO}_2(\text{aq}) + 2\text{H}_2\text{O}$	-1.2318	-1.9864	-2.6037	-3.1150	-3.5362	-3.8792	-4.1661
$\text{Andalusite} + 6\text{H}^+ = 2\text{Al}^{+3} + \text{SiO}_2(\text{aq}) + 3\text{H}_2\text{O}$	2.1095	-0.3127	-2.3914	-4.2009	-5.7804	-7.1607	-8.3809
$\text{Diaspore} + 3\text{H}^+ = \text{Al}^{+3} + 2\text{H}_2\text{O}$	1.5816	0.4528	-0.5097	-1.3469	-2.0786	-2.7202	-3.2938
$\text{Kaolinite} + 6\text{H}^+ = 2\text{Al}^{+3} + 2\text{SiO}_2(\text{aq}) + 5\text{H}_2\text{O}$	-3.0124	-4.5836	-5.8920	-7.0052	-7.9568	-8.7703	-9.4918
$\text{Microcline} + 4\text{H}^+ = \text{K}^+ + \text{Al}^{+3} + 3\text{SiO}_2(\text{aq}) + 2\text{H}_2\text{O}$	-2.9493	-3.4580	-3.8787	-4.2275	-4.5142	-4.7463	-4.9397
$\text{Muscovite} + 10\text{H}^+ = \text{K}^+ + 3\text{Al}^{+3} + 3\text{SiO}_2(\text{aq}) + 6\text{H}_2\text{O}$	-1.4144	-4.1032	-6.3866	-8.3613	-10.0729	-11.5573	-12.8734
$\text{Paragonite} + 10\text{H}^+ = \text{Na}^+ + 3\text{Al}^{+3} + 3\text{SiO}_2(\text{aq}) + 6\text{H}_2\text{O}$	0.5054	-2.3924	-4.8400	-6.9465	-8.7623	-10.3293	-11.7113
$\text{Pyrophyllite} + 6\text{H}^+ = 2\text{Al}^{+3} + 4\text{SiO}_2(\text{aq}) + 4\text{H}_2\text{O}$	-7.5404	-8.8907	-10.0279	-10.9980	-11.8262	-12.5288	-13.1427
$\text{Quartz} = \text{SiO}_2(\text{aq})$	-2.6790	-2.4467	-2.2446	-2.0641	-1.9015	-1.7532	-1.6174

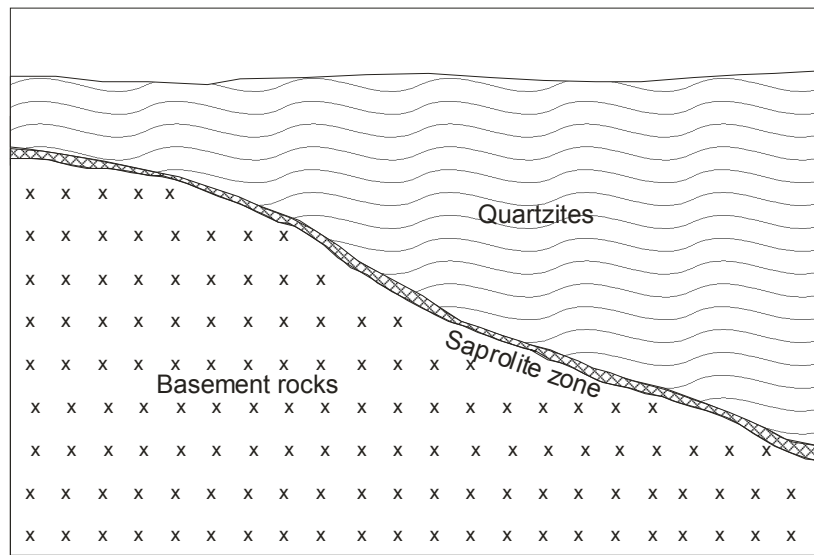


Figure 4.3. Schematic cross-section showing the occurrence of saprolite horizon beneath the quartzites in a basinal environment (not to scale). Fluid flow is assumed to be channelized along the permeable saprolite zone.

As discussed above, the Barron Quartzite and paleosol (Fig. 4.1) represent the archetypes for such late Paleoproterozoic rocks in the southern Lake Superior region because they are unaffected by 1630 Ma metamorphism or 1460 Ma metasomatism. The initial mineralogical composition of the model domain was selected to be equivalent to that of Barron pelite and siltstone. Table 4.2 shows the mean chemical compositions for Barron sediments and Sioux pipestone. Na, Ca, Mg and Mn occur in minor concentrations, indicating the high degree of its chemical maturity. We used the chemical composition of the Barron protolith to calculate the modal abundance of the stable phases by free energy minimization (Perplex, Connolly, 1990) along the model grid using the corresponding P-T conditions for the system KASH.

Stable mineral reactions in the system KASH for the P-T range of the model are shown in Figure 4.4a. Two mineral zones - a muscovite-kaolinite-quartz (mu-kao-qtz) and a muscovite-pyrophyllite-quartz (mu-prl-qtz) zone – are present in the modeling domain (Fig. 4.4b). Mu-kao-qtz assemblage was used along the grid at temperatures below 288 °C while mu-prl-qtz assemblages are predicted for higher temperatures (Fig. 4.4c). Mineral modes (volumetric ratios) in the mu-kao-qtz zone are 2 mu : 34 kao : 37 qtz. Similarly, 2 mu : 43 prl : 22 qtz were calculated for the mu-prl-qtz zone. Allocating different volume percentages for the same minerals in the two zones were done in order to equalize the bulk composition of the protolith in both zones. Equal amounts of albite

and microcline were also included (8 ab : 8 kfs). The porosity of the system was set at 12 percent. This value is relatively high, but it was chosen to prevent early clogging of the system due to initial hydration of feldspar assemblages. In nature it is assumed that the system can accommodate some expansion or compaction in response to fluid-rock interaction, an effect not modeled in our current contribution.

Table 4.2. Average chemical composition of Late Paleoproterozoic sedimentary rocks. Note the increase in Al₂O₃ and K₂O, and decrease in SiO₂ in pipestone compared to the unmetasomatized quartzite.

	Unmetasomatized quartzite from Barron	Pipestone from Sioux
SiO ₂	67.70	52.20
TiO ₂	0.81	0.40
Al ₂ O ₃	17.30	33.90
Fe ₂ O ₃	5.51	2.81
MnO	0.01	0.01
MgO	0.01	0.10
CaO	0.07	0.19
Na ₂ O	0.01	0.08
K ₂ O	0.39	4.47
P ₂ O ₅	0.08	0.08
LOI	6.15	5.85
Sum	98.04	100.08
<i>Modes (wt%)</i>		
Qtz	49.11	
Hem	5.47	2.80
Rt	0.59	0.30
Kao	43.49	
Prl		53.70
Mu	1.34	37.70
Dsp		5.50
Analysis by Medaris (2003)		

Initial reactive surface area of each mineral was assumed to be 1000 m² per m³ of rock. The flow rate of migrating fluids was set to 10.0 m³m⁻²yr⁻¹. Considering this flow-dominated system, longitudinal dispersivity was taken as 10 m making the combined dispersion/diffusion coefficient for all solute species 3.17 x 10⁻⁶ m² s⁻¹. These flow parameters yield a grid Peclet number which yields numerically stable simulations. Mineral dissolution/precipitation rates, including activation energies, used in the calculations are given in Table 4.3. For those minerals where experimental rate data are not available, a value of 1.0 x 10⁻¹⁰ mole m⁻² s⁻¹ was assigned for all temperatures of the model. This value was assumed to be in the average range of reaction rates for most of the rock forming minerals.

Table 4.3. Reaction rates and activation energies of minerals used in simulations.

Mineral	Reaction rate at 25°C (mol/m ² /s)	Activation energy (kcal/mol)	Comments
Albite	5.495×10^{-13}	13.0	
Andalusite	1.000×10^{-10}	0.0	Assumed rate at P,T
Diaspore	1.000×10^{-10}	0.0	Assumed rate at P,T
Kaolinite	5.248×10^{-14}	7.7	
Microcline	3.162×10^{-13}	12.5	
Muscovite	8.511×10^{-14}	15.0	Ea = average value
Paragonite	8.511×10^{-14}	15.0	Taken similar to mu
Pyrophyllite	5.248×10^{-14}	7.7	Taken similar to kao
Quartz	4.073×10^{-14}	17.0	

Data from Lasaga (1998).

Initial fluid composition

The initial fluid compositions in the pore spaces were considered to be in equilibrium with the mineral assemblage of each zone. Hence the chemical speciation of the initial solution at the pressures and temperatures of the two extremes of the model grid was calculated using the equilibrium geochemical speciation model SOLUB (Roselle and Baumgartner, 1986). They were used as initial estimates. Several fluid compositions to be used for different test cases were obtained by changing the total concentrations of Cl and K. 1DREACT calculates the aqueous species concentrations using mass and charge balance equations, and mineral equilibrium constraints. Table 4.4 gives a summary of the initial fluid compositions and the constraints for each aqueous species used in simulations. When flow is turned on equilibrated fluid is displaced along the one-dimensional domain, thereby disequilibrating the column, which in turn causes mineral-fluid reactions to occur.

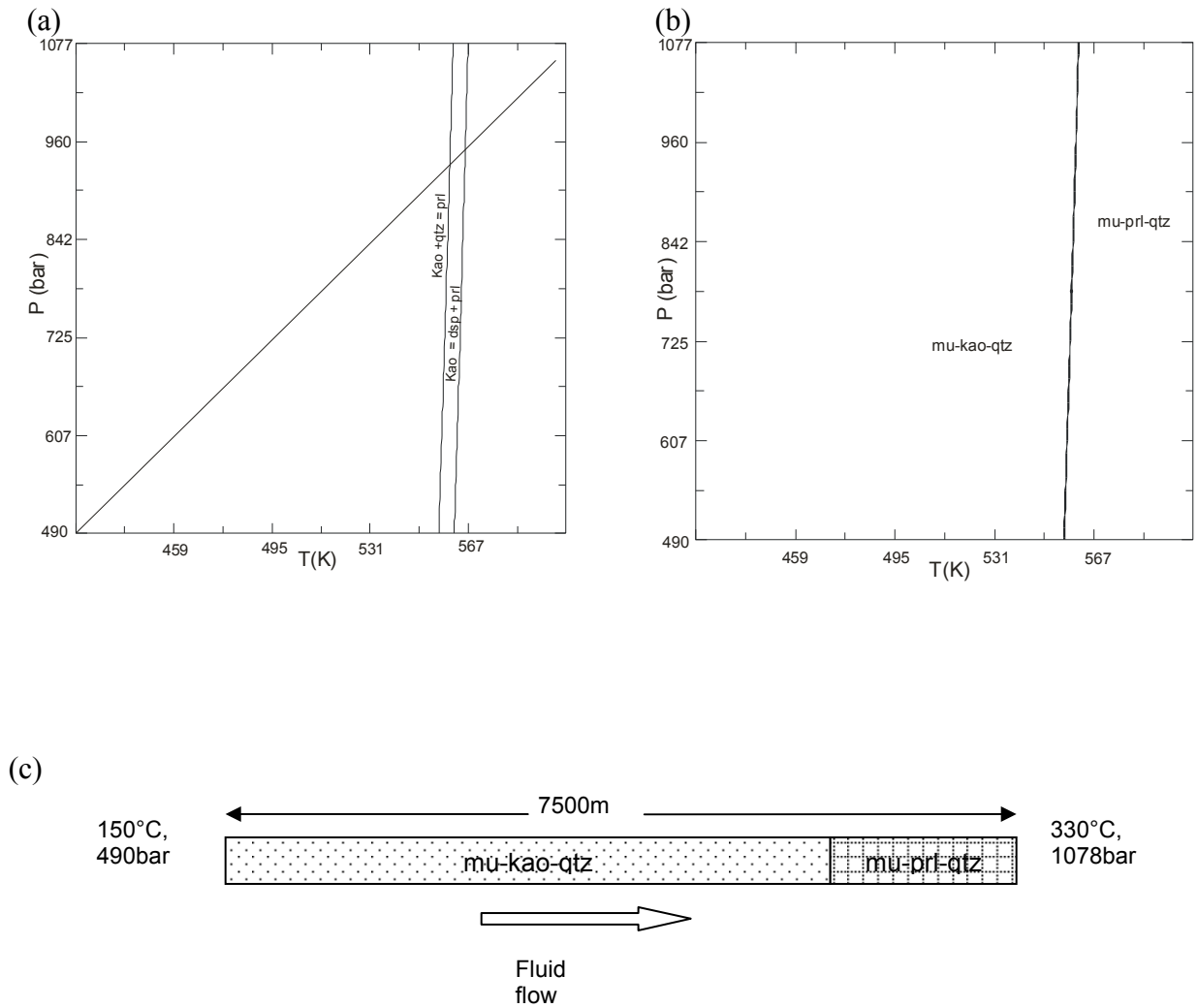


Figure 4.4. (a) Phase diagram for SiO₂ saturated KASH system. The diagonal line indicates the P-T gradient selected for the one-dimensional model grid. (b) Phase diagram calculated using Perplex for the bulk composition of unmetasomatized quartzite given in Table 4.2. (c) Schematic diagram of the model grid showing initial mineral zones, P-T conditions at the boundaries, and up-temperature flow.

Table 4.4. Initial fluid compositions distributed in mineral zones for different test cases, and the constraints used to buffer the aqueous species concentrations.

Component	Concentration (mol/kg w)						Constraint
	mu-kao-qtz zone T = 150 °C			mu-prl-qtz zone T = 300 °C			
	<i>Fluid I</i>	<i>Fluid II</i>	<i>Fluid III</i>	<i>Fluid I</i>	<i>Fluid II</i>	<i>Fluid III</i>	
H ⁺	1.565 × 10 ⁻⁵	7.812 × 10 ⁻⁵	1.964 × 10 ⁻⁵	2.083 × 10 ⁻⁴	9.802 × 10 ⁻⁴	2.370 × 10 ⁻⁴	Charge balance
Al ⁺³	4.132 × 10 ⁻¹³	1.888 × 10 ⁻¹⁰	5.520 × 10 ⁻¹²	1.263 × 10 ⁻¹²	7.480 × 10 ⁻¹⁰	2.267 × 10 ⁻¹¹	*
Cl ⁻	9.778 × 10 ⁻²	4.669 × 10 ⁻¹	8.887 × 10 ⁻¹	9.167 × 10 ⁻²	4.074 × 10 ⁻¹	7.384 × 10 ⁻¹	Total Cl concentration
K ⁺	1.979 × 10 ⁻²	9.675 × 10 ⁻²	2.734 × 10 ⁻²	1.900 × 10 ⁻²	8.828 × 10 ⁻²	2.103 × 10 ⁻²	Muscovite equilibrium
Na ⁺	7.797 × 10 ⁻²	3.700 × 10 ⁻¹	8.649 × 10 ⁻¹	7.246 × 10 ⁻²	3.181 × 10 ⁻¹	7.171 × 10 ⁻¹	Total Na concentration
SiO ₂ (aq)	2.094 × 10 ⁻³	2.094 × 10 ⁻³	2.090 × 10 ⁻³	1.254 × 10 ⁻²	1.254 × 10 ⁻²	1.250 × 10 ⁻²	Quartz equilibrium

* kaolinite equilibrium in mu-kao-qtz zone; pyrophyllite equilibrium in mu-prl-qtz zone

4.4 Results and discussion

Fluid-rock interaction simulations were carried out for flow both up-temperature and down-temperature for different fluid compositions. Initial trials with down-temperature flow (upwelling fluids) show that this always leads to precipitation of quartz. Quartz volume profiles at different time intervals are shown in Figure 4.5. Note that the step in the initial volume curve is due to the different initial volumes assigned to the two mineral zones (see discussion above). Quartz precipitation along down-temperature flow is not an unexpected result considering the temperature dependence of silica solubility, which decreases with decreasing temperature. Hence upwelling (cooling) fluids are oversaturated with respect to quartz and will precipitate quartz on ascent. A similar situation was observed in the modeling of quartz dissolution/precipitation in a basinal hydrothermal system by Bolton et al., (1999). Continued fluid flow in down-temperature direction leads to clogging up of the porosity with quartz, and cessation of fluid transport.

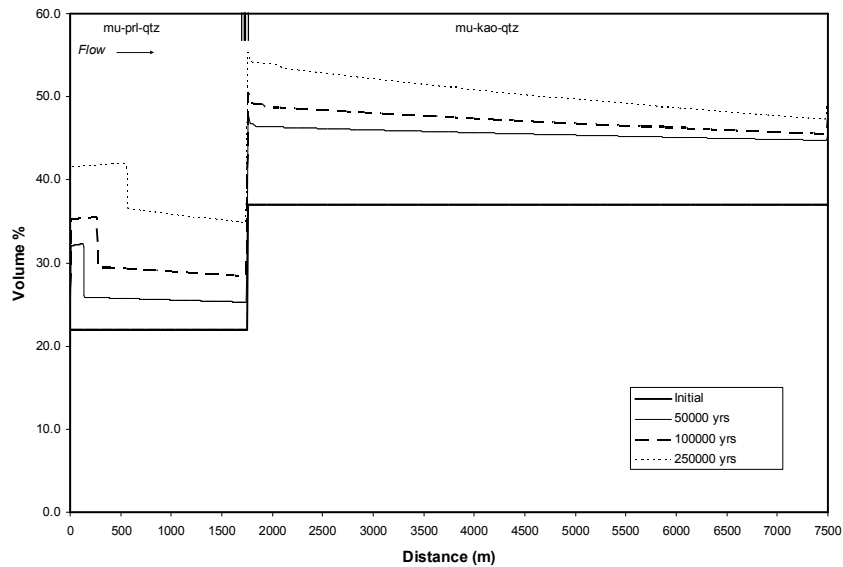


Figure 4.5. Change of quartz volume percentage along the model grid with time for a down-temperature flow. Note that the quartz precipitation front in mu-prl-qtz zone coincides with the dissolution front of initial feldspars. Orientation of the grid with respect to flow direction and initial mineral zones are also given.

Figure 4.6a shows the mineral paragenesis calculated using *Perple_X* for the bulk composition of the rock after 250000 years at 318 °C and 1038 bar. These P-T values correspond to those at a grid point chosen to represent the average mineralogical evolution of the system, and otherwise have no petrological significance. The starting mineral assemblage of mu-prl-qtz remains stable as the fluid-rock interaction proceeds. The bulk compositions of the rock calculated using the mineral modes at different time intervals for the same P-T conditions have been plotted in Figure 4.6b. The composition evolves towards a SiO₂-rich system, while at the same time Al₂O₃ is depleted. The observed mineralogical composition of the metasomatized quartzite is mu-prl-dsp which is devoid of quartz. It is poor in SiO₂ and rich in Al₂O₃ which is opposite to the calculated trend shown in Figure 4.6b. Therefore it can be concluded that reactions during a down-temperature flow, and hence discharge, cannot produce the pipestone deposits found in several places in the Lake Superior area.

In the following part we discuss the results obtained from fluid-rock interaction simulations carried out for up-temperature flow as will be present in the recharge area. Such a flow could be set up in a groundwater recharge zones due to topography or due to recharge area of convection cells generated as a result of igneous intrusions like the Wolf River batholith.

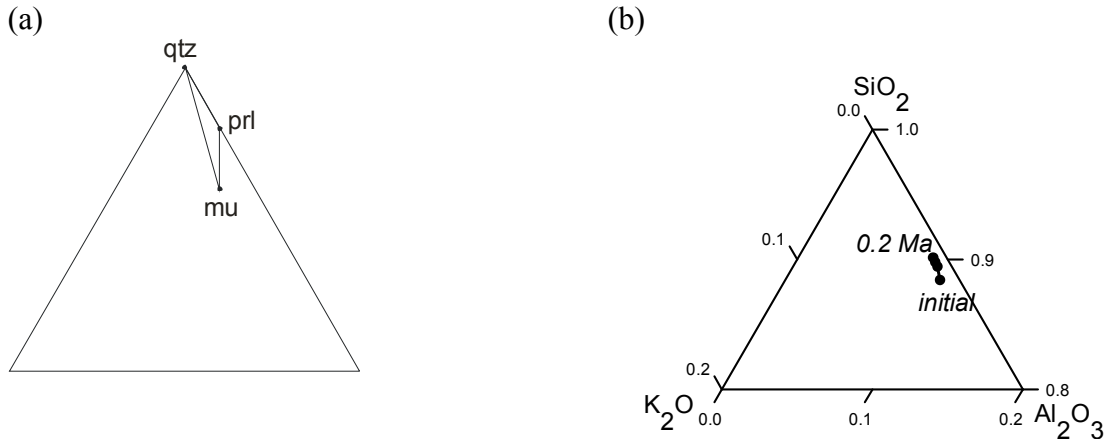


Figure 4.6. (a) Stable mineral assemblage calculated using the bulk composition at $x = 500$ m after 250000 years (b) Ternary plot showing the representative compositional evolution of the system calculated using the bulk composition at $x = 500$ m at different time intervals for down-temperature flow.

Several initial fluid compositions were tested with varying Cl and K concentrations (Table 4.4). Generally, fluids with total Cl concentrations exceeding 0.5 molal and rich in Na do not reproduce the alteration observed in pipestones. The solution becomes

oversaturated with respect to paragonite due to higher Na concentration associated with the increased salinity. As fluid-rock interaction proceeds, paragonite precipitates, replacing muscovite in the initial mu-prl-qtz zone. A snap shot of the mineral abundances along the model domain after 1 Ma is shown in Figure 4.7a. The composition of the system has evolved to a $\text{Na}_2\text{O} + \text{Al}_2\text{O}_3$ -rich one, with low SiO_2 percentage. The ternary composition diagram calculated using the bulk composition of the rock shows that paragonite-pyrophyllite-diaspore is the stable mineral assemblage at 318 °C and 1038 bar (Fig. 4.7b). Thus Na-rich, high salinity fluids can be ruled out as possible sources for the observed metasomatism of quartzites. Fluid I in Table 4.4 gives the composition of the fluid that best approximated the metasomatic process in fluid-rock interaction simulations, and the results presented in following sections have been obtained using it as the initial fluid.

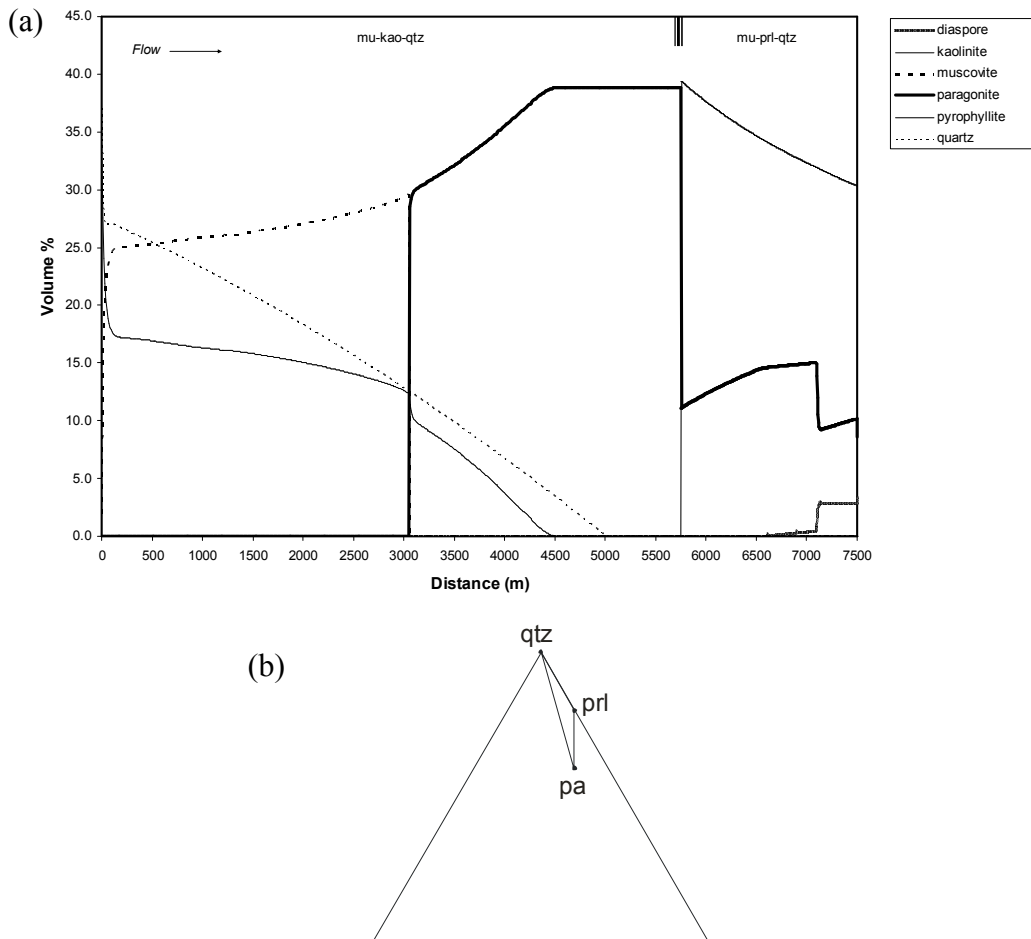


Figure 4.7. (a) Mineral volume percentages along the model grid after 1 Ma when a high salinity fluid (Fluid III; Table 4) is used. (b) Stable mineral assemblage calculated using the bulk composition at $x = 7000$ m.

Due to fluid flow quartz in the qtz-prl-mu zone starts to dissolve and the dissolution front migrates upstream. Figure 4.8 shows the change of quartz abundance along the one-dimensional model domain with time. After 1 Ma quartz has been completely dissolved in this zone. While the system is devoid of quartz, muscovite and diasporite form at a slower pace (Fig 4.9). Both kaolinite and pyrophyllite amounts along the grid are decreasing with time as fluid-rock interaction proceeds. This takes place due to the reactions with a K-rich fluid that would explain the formation of muscovite by the following reactions.

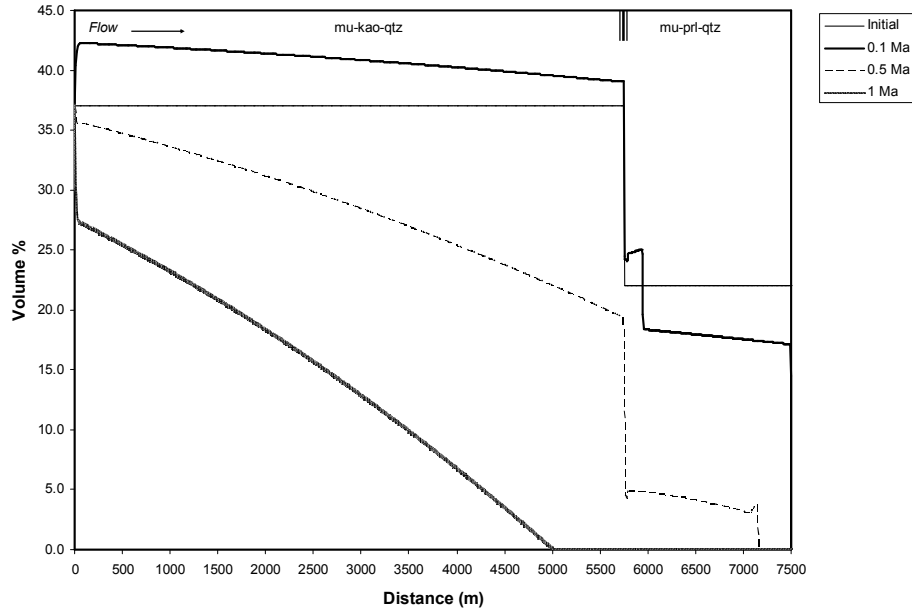
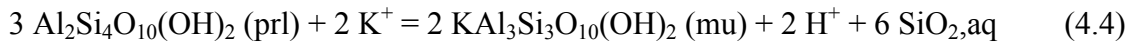
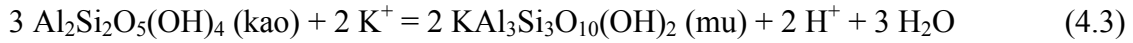


Figure 4.8. Change of quartz volume along the model grid with time. The increase in quartz precipitation in first two time intervals is due to the initial feldspar dissolution reactions. Quartz starts to dissolve when feldspars have completely been removed from the system.

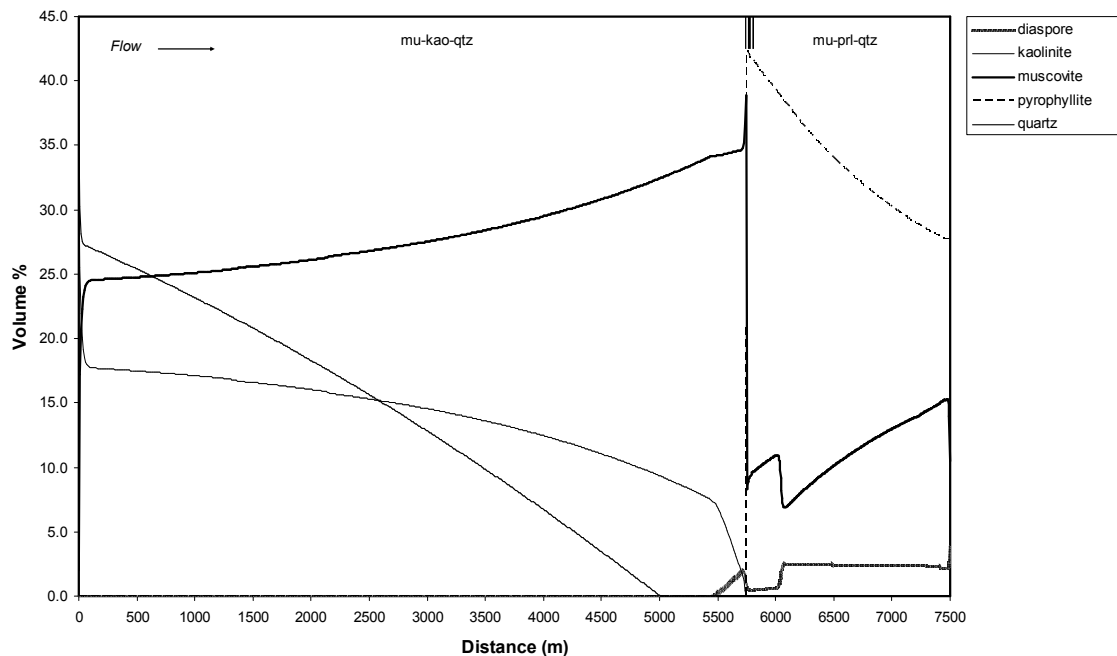


Figure 4.9. A representative mineral abundance profile along the model grid as fluid-rock interaction proceeds under an up-temperature flow.

The evolution of the bulk composition of the system along the grid is shown in Figure 4.10. SiO_2 is depleted with time, whereas K_2O and Al_2O_3 are enriched. This process is more pronounced towards higher temperatures in the model domain. It can be seen that K_2O mole fraction increases with time resulting in muscovite formation. The trends in Figure 4.10 are summarized on the ternary plot in Figure 4.11 as calculated using *Perple_X* for the bulk composition of the rock at 318 °C and 1038 bar. It shows the path of the representative compositional evolution of the system. As illustrated in Figure 4.11 the composition of the system evolves from a highly silica-rich to a silica-deficient system while Al_2O_3 and K_2O increase with time. Whole-rock analyses of metasomatised quartzites show that they are lower in SiO_2 and higher in Al_2O_3 and K_2O content when compared to the unaltered protolith (Table 4.2). Thus our simulations reproduced the observed compositional changes during metasomatism of the paleosol due to interaction

with a fluid rich in K. Observed metamorphic assemblages illustrated in Figure 4.2 are in close agreement with the simulation results (Fig. 4.12). Quartz and muscovite are stable over the whole pressure-temperature range of the model (150-330°C, 490-980bar) while kaolinite restricts to temperatures below 288°C. Pyrophyllite and diasporite are stable up to 345°C that slightly exceeds the temperatures related to the dimensions of the model domain (Fig. 4.2). It is clearly the action of fluid that has led to dissolution of quartz and continued precipitation of muscovite. A noteworthy feature of the curves in Figures 4.9 and 4.10 is the sharp discontinuities which indicate increased mineral dissolution and precipitation. Close examination of these shows that they correspond to the isograds shown in Figure 4.4a ($kln + qtz \Rightarrow prl$, and $kln \Rightarrow prl + dsp$) when the relevant pressure and temperature are encountered along the model domain. At the isograds discontinuities in the slope of the concentration profiles exists due to phase changes, which results in near discontinuities in the $\partial C_j / \partial x$ term in Eqn. 4.1. The second derivative is close to singular. As a consequence, diffusion and dispersion result in a strong increase in mineral dissolution/precipitation in the vicinity of the isograd (Eugster and Baumgartner, 1989; Lasaga, 1998). Hence diffusion induced fluid-rock interaction is important in the vicinity of any isograd.

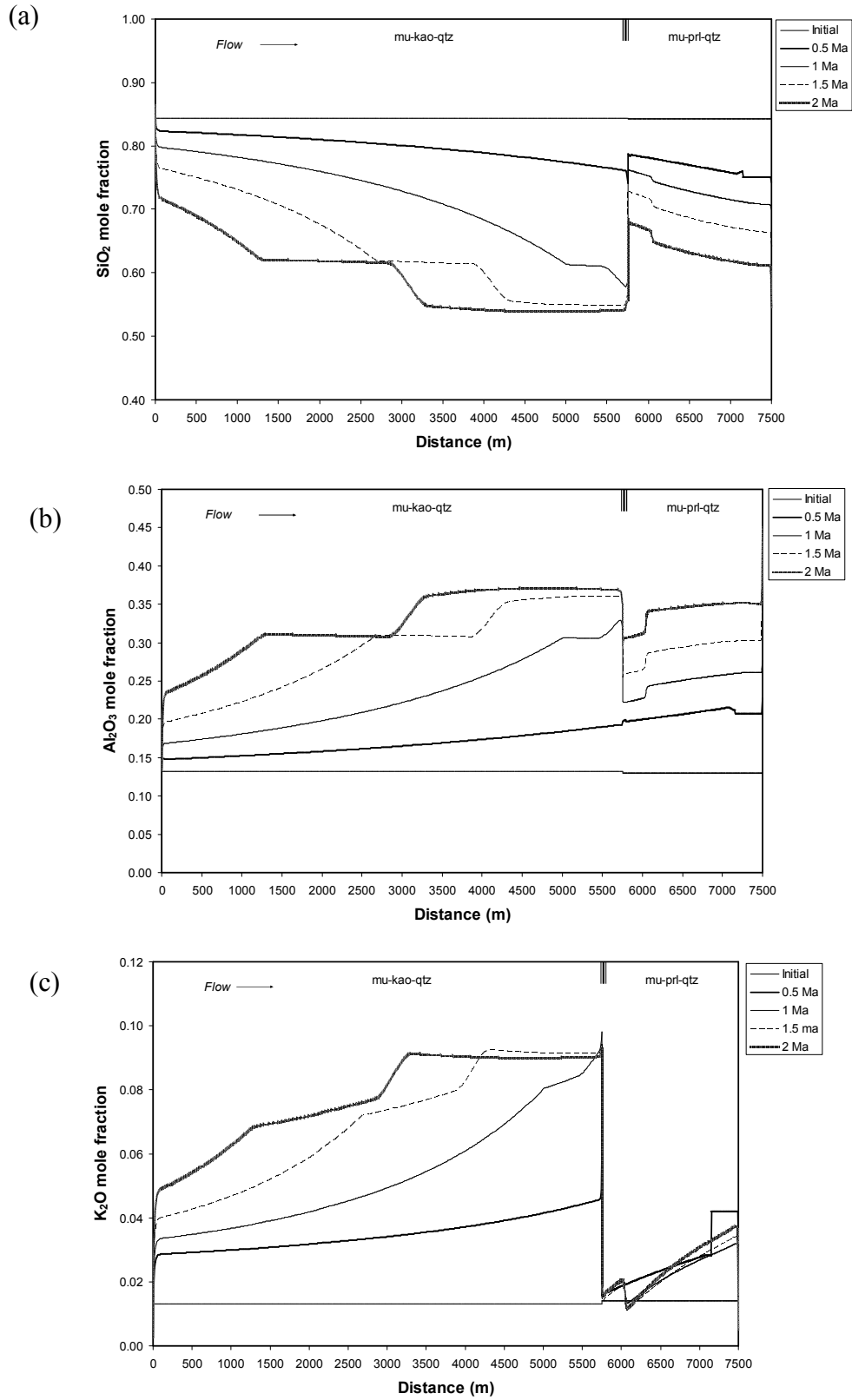


Figure 4.10. Change of oxide mole fractions along the grid (a) SiO₂ (b) Al₂O₃ (c) K₂O.

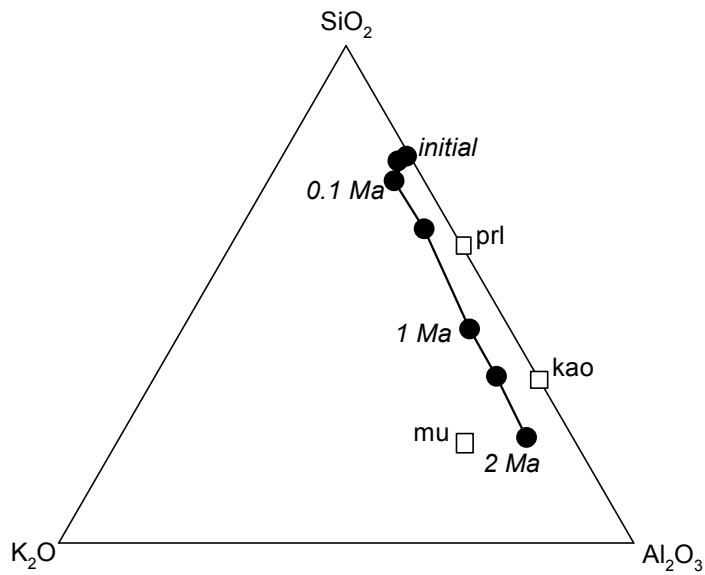


Figure 4.11. Ternary plot showing the representative compositional evolution of the system calculated using the bulk composition at $x = 7000$ m at different time intervals for up-temperature flow.

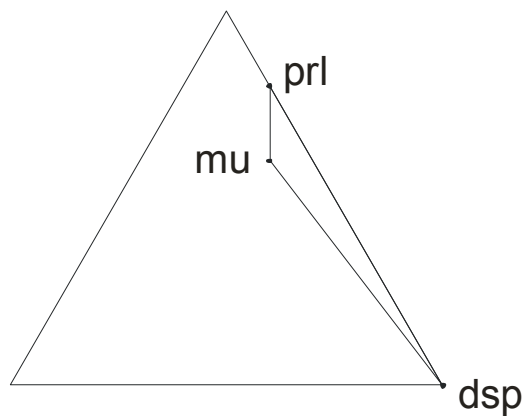


Figure 4.12. Stable mineral assemblage calculated using the bulk composition at $x = 7000$ m after 2 Ma.

4.5 Conclusion

Hydrothermal alteration of Paleoproterozoic sedimentary rocks belonging to the Baraboo Interval has been modeled with a reactive fluid transport modeling algorithm. Observed mineralogical transformations are successfully reproduced in an up-temperature flow system. The results show that fluids flowing along the permeable channel ways can react with the existing minerals to produce the observed rock compositions. Potassium has been brought into the system by hydrothermal fluids that results in K-metasomatism of quartzites as reflected in formation of muscovite. The source of hydrothermal fluids can be probably attributed to the post-metamorphic igneous activity in the region at ca. 1465 Ma that provided the thermal flux for regional scale fluid flow. Evidence for this is given by $^{40}\text{Ar}/^{39}\text{Ar}$ plateau ages of muscovite-bearing assemblages which are found to be in between 1467 ± 11 Ma and 1280 ± 13 Ma, where muscovite is believed to have grown or cooled below its closure temperature (Medaris et al., 2003). The basement rocks below the Baraboo Interval quartzites are extensively retrograded to low-grade mineral assemblages (Medaris and Dott, 2001), and this metamorphism has been related to the ~1630 Ma tectonothermal event that affected the Southern Lake Superior region based on $^{40}\text{Ar}/^{39}\text{Ar}$ biotite and hornblende and Rb-Sr whole-rock isochron ages. Our fluid-rock interaction simulation results support the view that hydrothermal fluids associated with igneous activity, particularly related to Wolf River batholith (~1465 Ma), could have played a significant role in later metasomatism.

References

- Anderson, J.L. and Cullers, R.L., 1978. Geochemistry and evolution of the Wolf River Batholith, a Late Precambrian rapakivi massif in north Wisconsin, U.S.A. *Precambrian Res.*, 7, 287-324.
- Bolton, E.W., Lasaga, A.C. and Rye, D.M., 1999. Long-term flow/chemistry feedback in a porous medium with heterogeneous permeability: Kinetic control of dissolution and precipitation. *Am. J. Sci.*, 299, 1-68.
- Connolly, J.A.D., 1990. Multivariable phase diagrams: An algorithm based on generalized thermodynamics. *Am. J. Sci.*, 290, 666-718.
- Connolly, J.A.D. and Petrini, K., 2002. An automated strategy for calculation of phase diagram sections and retrieval of rock properties as a function of physical conditions. *J. Met. Geol.* 20, 697-708.
- Dott, R.H., Jr., 1983. The Proterozoic quartzite enigma in the north-central U.S.-resolved by plate collision? In: Medaris, L.G., Jr., ed. Early Proterozoic geology of the Great Lakes region. *Geol. Soc. Am. Mem.* 160, 129-141.

- Eugster, H.P., and Baumgartner, L.P., 1989. Mineral solubilities and speciation in supercritical metamorphic fluids. In: Carmichaels, I.S.E., Eugster, H.P. (Eds), *Thermodynamic modeling of geological materials: Minerals, fluids and melts*. Mineralogical Society of America. *Reviews in Mineralogy*. 17, 367-403.
- Hauzenberger, C.A., Baumgartner, L.P. and Pak, T. M., 2001. Experimental study on the solubility of the "model"-pelite mineral assemblage albite + K-feldspar + andalusite + quartz in supercritical chloride-rich aqueous solutions at 0.2 GPa and 600 degrees C. *Geochim. Cosmochim. Acta*. 65(24), 4493-4507.
- Helgeson, H.C., Kirkham, D.H., 1974. Theoretical prediction of the thermodynamic behavior of aqueous electrolytes at high pressures and temperatures: II. Debye-Hückel parameters for activity coefficients and relative partial molar properties. *Am. J. Sci.* 274, 1199-1261.
- Holland, T. and Powell, R., 1991. A compensated-Reidlich-Kwong (CORK) equation for volumes and fugacities of CO₂ and H₂O in the range 1 bar to 50 kbar and 100-1600⁰C. *Contrib. Mineral. Petrol.* 109, 265-273.
- Holland, T. and Powell, R., 1991. A compensated-Reidlich-Kwong (CORK) equation for volumes and fugacities of CO₂ and H₂O in the range 1 bar to 50 kbar and 100-16000C. *Contrib. Mineral. Petrol.* 109, 265-273.
- Holland, T.J.B., and Powell, R., 1998. An internally-consistent thermodynamic data set for phases of petrological interest. *J. Met. Geol.* 16, 309-343.
- Holm, D., Schneider, D. and Coath, C.D., 1998. Age and deformation of Early Proterozoic quartzites in the southern Lake Superior region: Implications for extent of foreland deformation during final assembly of lauriantia. *Geology*, 26, 907-910.
- Johnson, JW, Oelkers, EH, and Helgeson, HC (1992). SUPCRT92: A software package for calculating the standard molal thermodynamic properties of minerals, gases, aqueous species, and reactions from 1 to 5000 bars and 0 to 1000 degrees C. *Computers & Geosciences*, 18(7), 899-947.
- Lasaga, A.C., 1998. *Kinetic theory in the earth sciences*. Princeton University Press. 728pp.
- Medaris, L.G., Jr., Singer, B.S., Dott, R.H., Jr., Naymark, A., Johnson, C.M., and Schott, R.C. 2003. Late Paleoproterozoic climate, tectonics, and metamorphism in the Southern Lake Superior region and Proto-North America: Evidence from Baraboo Interval quartzite. *J. Geol.* 111, 243-257.
- Medaris, L.G., Jr., Dott, R.H., Jr., 2001. Sedimentologic, tectonic and metamorphic history of the Baraboo Interval: new evidence from investigations in the Baraboo Range, Wisconsin. *Institute on Lake Superior Geology Proceedings*, 47th annual meeting (Madison, Wis.), 47, pt. 2:1-21.
- Oelkers, E.H., Helgeson, H.C., Shock, E.L., Sverjensky, D.A., Johnson, J.W., and Pokrovskii, V.A., (1995). Summary of the apparent partial standard partial molal

Gibbs free energies of formation of aqueous species, minerals and gases at pressures 1 to 5000 bars and temperatures 25 to 1000 degrees C. *J. Phys. Chem. Ref. Data* 24, 1401-1560.

Pak, T.M., Hauzenberger, C.A., and Baumgartner, 2003. Solubility of the assemblage albite+K-feldspar+andalusite+quartz in supercritical aqueous chloride solutions at 650 °C and 2 kbar. *Chemical Geology* (in press).

Roselle, G.T. and Baumgartner, L.P., 1995. Experimental determination of anorthite solubility and calcium speciation in supercritical chloride solutions at 2 kb from 400 to 600°C. *Geochim. Cosmochim. Acta* 59, 1539-1549.

Steeffel, C.I., 1993. 1DREACT User Manual.

Steeffel, C.I., Lasaga, A.C., 1994. A coupled model for transport of multiple chemical species and kinetic precipitation/dissolution reactions with applications to reactive flow in single phase hydrothermal system. *Am. J. Sci.* 294, 529-592.

Modeling Hydrothermal Alteration of Basalts in High-temperature Geothermal Systems in Iceland

ABSTRACT

Hydrothermal alteration of basalts in high-temperature areas in Iceland was modeled using a reactive fluid transport code, 1DREACT (Steeffel, 1993). Fresh water and saline water compositions of the geothermal fluid were used to see the effect of salinity on alteration. Different fluid compositions result in different mineral abundances, but the same alteration mineralogy is formed which is in agreement with analytical results. Feasibility of pseudo compound approach to include solid solutions was tested. It shows the capability of a first order approximation of the system. However, a rigorous treatment of the solid solutions in this complex system is not possible at present using this approach, since this would require a detailed knowledge of precipitation kinetics as a function of mineral composition.

5.1 Introduction

Numerical modeling of hydrothermal systems has been a widely addressed research field due to its relevance in characterizing the processes involved in ore formation, metasomatism and geothermal energy. Aqueous fluids are highly reactive at high temperatures, reaction rates are fast, and lead to intense alteration as is characteristic of most high temperature hydrothermal systems. Fluid-rock interaction models help to better understand the processes involved in mineralization. Numerical modeling of reactive flow in hydrothermal systems requires solving the governing kinetic dissolution-precipitation equations of multi-component reactions, including solid solutions, coupled with fluid flow under non-isothermal conditions. Solid solutions are abundant in hydrothermal systems. For better approximation of the processes, they must be included in reactive transport models. This chapter discusses the modeling of hydrothermal alteration of basalts incorporating solid solutions into fluid-rock interaction calculations, using as an example hydrothermal systems from Iceland.

Due to the position of Iceland on the Mid-Atlantic Ridge high temperature gradients drive prominent and wide-spread hydrothermal systems (Jacoby and Girardin, 1980). Moreover, the presence of glacier- and ocean-fed hydrothermal systems in Iceland provides a favourable situation to investigate the effect of salinity on fluid-rock interactions. The temperature/pressure range of the hydrothermal fluids in Iceland lend themselves for quantitative mineral-fluid calculations as the thermodynamic properties of the aqueous species are best known at relatively

low temperatures along the boiling curve up to near the critical point of water (Helgeson et al, 1981). The effect of boiling on the hydrothermal system is difficult to explore. On one hand, the onset of boiling requires that an equation of transport for two phase flow be solved, on the other hand, the solubility of anions and cations in the vapor phase is poorly. Hence, two-phase fluids are not considered here. The one-dimensional reactive fluid transport code, 1DREACT (Steefel, 1993) will be used to model the alteration of basalts in high-temperature hydrothermal systems of Iceland. Thermodynamic data for most of the low-temperature alteration minerals are scarce. Therefore modeling will be restricted to the higher temperatures of the alteration profile.

5.2 Icelandic geothermal systems and their hydrothermal alteration

Geology and hydrothermal activity

Iceland is a site of active volcanism, comprising plume-type as well as MAR (Mid-Atlantic Ridge)-type lavas. Recent volcanism has occurred in two types of zones, namely axial rift zone which represents the landward extension of MAR and flank zones where volcanism off the main rift axis has produced young volcanics that unconformably overlie older volcanics (Meyer, 1985; Fig. 5.1). The SW and NE axial rift zones are dominated by olivine tholeiites and tholeiites while the SE zone is transitional to alkali basalts from tholeiitic. The active volcanism generates extensive hydrothermal activity mainly related to Pliocene and Pleistocene basaltic rocks of the axial Neo volcanic rift zone. To a minor extent, hydrothermal activity also occurs within Tertiary plateau basalts to the east and to the west of the axial rift zone (Pálmason, 1974). Two types of hydrothermal terrains have been identified in Iceland: those where temperatures in excess of 200 °C are encountered in the upper 1000m and those where temperatures do not exceed 150°C in this depth range (Fridleifsson, 1979; Fig. 5.1). Springs within the western Tertiary basalts derive their waters from the mountainous areas of the north-western peninsulas and from the central highlands and icecaps. The latter source also contributes to the southern Neo volcanic zone. This latter segment is also supplied both locally and from the southern icecap. The only occurrences of a major component of seawater in the high temperature hydrothermal fields are on the Reykjanes Peninsula. Compositionally the geothermal waters in this region appear to be the result of seawater-basalt interactions at temperatures around 300 °C (Kristmannsdóttir, 1983) although isotope systematics point to a more complex origin (Ólafsson and Riley, 1978).

Hydrothermal alteration

Fluid-rock interaction in geothermal systems leads to intense alteration of the volcanic mineral assemblage. Simultaneously, the fluid chemistry changes due to mineral dissolution/precipitation that ultimately changes the porosity and permeability of the rock. An influential role in determining the nature of alteration mineralogy is played by the composition of the infiltrating water. A number of studies on alteration mineralogy of basalts in Icelandic hydrothermal systems have been carried out by Kristmannsdóttir (1975, 1978, 1982), Exley (1980), Mehegan et al.,

(1980), Fridleifsson (1983, 1984), and Franzson (1983). Arnórsson (1978, 1995) has described the chemistry of geothermal waters in many geothermal fields in Iceland and comparative alteration patterns therein. He further points out that the age of the geothermal system together with the internal structure of the rock to be the prime factor in determining the extent of alteration. Kristmannsdóttir (1978) observes that irrespective of the quantitative rate of alteration, the same main mineral phases to be formed at the same rock temperature in Icelandic geothermal areas. These main alteration phases can be classified into four groups based on the appearance of index minerals corresponding to each zone, namely, a smectite-zeolite zone, a mixed-layer clay mineral zone, a chlorite-epidote zone, and a chlorite-actinolite zone. Each hydrothermal mineral assemblage is stable over a particular temperature range and thus a depth distribution of alteration zones is observed (Fig. 5.2). The effect of the chemical composition of the circulating water has been investigated by Sveinbjörnsdóttir (1992). She proposes that equilibrium has been approached between the alteration minerals and their coexisting fluids. Despite having formed from reactions with circulating waters of markedly different compositions, the resultant major alteration mineral assemblages appear to be similar. However the chemical analysis has shown that the composition of the hydrothermal minerals is significantly different as a result of differences in chemical composition of the circulating fluids. Most of the secondary minerals form solid solutions (Ragnarsdóttir and Walther, 1984).

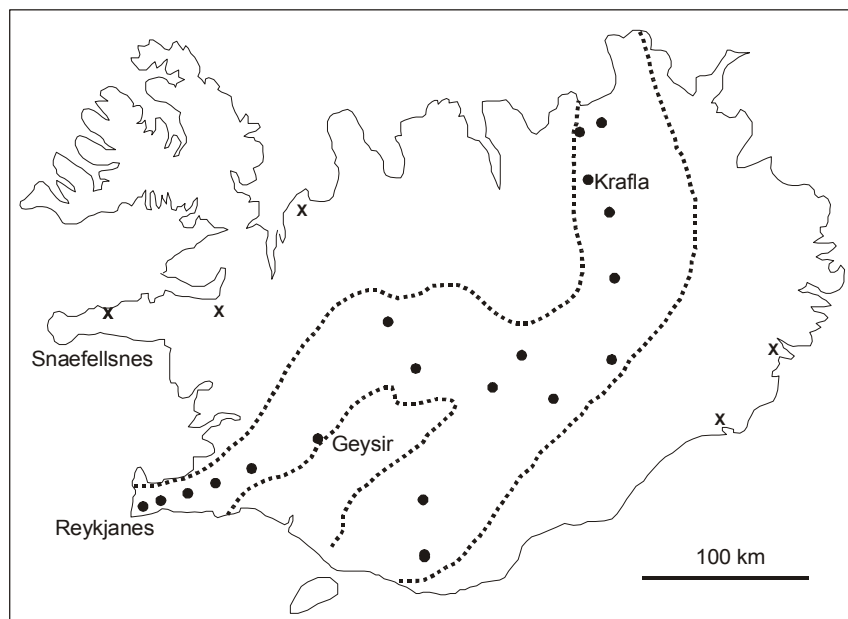


Figure 5.1. Active volcanic belts (delineated with thick broken lines) and high-temperature areas (dots) in Iceland. x indicates fossil geothermal systems now occurring in the flank zones of the central axial rift zone (from: Arnórsson, 1995).

Smectites	100° C
Zeolites	150° C
Clay minerals	200° C
Chlorite Epidote	250° C
Chlorite Actinolite	300° C

Figure 5.2. Alteration mineralogy in basalts from high-temperature areas in Iceland and correlating temperatures (from: Kristmannsdóttir, 1978).

5.3 Reactive fluid transport modeling

The coupled reaction and transport equation for the conservation of mass of a solute species can be expressed in the following form given by Steefel (1993).

$$\frac{\partial(\phi C_j)}{\partial t} + \nabla \cdot (u C_j - D \nabla C_j) = R_j \quad (j = 1, \dots, N_c) \quad (5.1)$$

where ϕ is the porosity, C_j is the total concentration of the j^{th} species, u is the Darcian fluid flux, D is the combined dispersion/diffusion coefficient and R_j is the total rate of the heterogeneous mineral-fluid reactions affecting the concentration of j^{th} species in solution. N_c is the total number of components. The total concentration is the sum of concentrations of species in the fluid phase for each component j . Equation 5.1, when implemented with a suitable numerical algorithm, provides a tool to characterize many of the processes that involve chemical reactions and fluid transport in geologic media.

For the fluid-rock interaction simulations the one dimensional multicomponent reactive fluid transport code 1DREACT (Steefel, 1993; Steefel and Lasaga, 1994) which is based on an integrated finite difference formulation of Eqn. 5.1 was used. It solves for aqueous species concentrations, calculates mineral precipitation/dissolution rates, saturation states and mineral

volumes under diffusion conditions or a fixed Darcian flux. It reads a thermodynamic database and requires initial fluid composition, mineral abundances and other physical parameters of the flow system.

5.4 Solid solutions in reactive flow models

Treatment of solid solutions in reactive fluid transport models requires that the composition of the solid is treated as a variable. Since many thermodynamic models of solid solutions are highly non-linear, this can seriously impact on the stability of the transport algorithm. A method to overcome these constraints and to improve the performance of the algorithm is to calculate phase equilibria in terms of pseudo compounds (see. e.g. Conolly, 1990) whose thermodynamic properties are used in reactive transport calculations. This approach has been described in detail in Chapter 3.

The high-temperature alteration mineralogy (~ 200 – 350 °C) of Icelandic basalts consists of amphibole, plagioclase, chlorite and epidote. All these minerals form solid solutions and it is necessary to incorporate their intermediate compositions in fluid-rock interaction calculations. However epidote was not included due to the complexity in solving Fe⁺³/Fe⁺² redox equilibrium, and uncertainties in determining the oxygen fugacity. The non-ideal mixing model of Newton et al., (1980) was used for plagioclase. Ideal mixing was used for amphiboles taking tremolite – ferroactinolite binary solution. A Bragg-Williams type model constructed by Holland et al., (1998) was used to calculate the activities of chlorite phases in clinocllore – daphnite binary solution. Most of the primary minerals in Icelandic basalts are also members of solid solutions. Thus the thermodynamic properties of these phases were calculated for olivine, ortho- and clinopyroxenes using ideal mixing models.

The thermodynamic database used in transport calculations contains logarithmic equilibrium constants (logK's) of reactions of aqueous species and minerals at different temperatures. They are written as hydrolysis reactions of one mole of mineral phase. To obtain this data, a series of dissociation reactions is included for each additional aqueous ionic species. Calculation of logK's of reactions that are included in the database is described in detail in Chapter 2. Once the logK's of reactions of end member components of solid solutions are calculated they can be used to calculate those of the intermediate phases. LogK of the dissolution reaction of an intermediate composition of a solid solution can be obtained from

$$\log K_{ss} = X_A \log K_A + X_B \log K_B + X_A \log a_A + X_B \log a_B \quad (5.2)$$

where K_{ss} , K_A and K_B are the equilibrium constants of the reactions of intermediate phase, end members A and B respectively. Log K_{ss} 's for all pseudo compounds of each solid solution are included in the thermodynamic database together with other mineral and aqueous species in the

system. The thermodynamic database contains $\log K$ values at temperature intervals of 37.5 °C from 150 °C to 375 °C along a hydrostatic pressure gradient of 98 bar/km. 1DREACT interpolates the $\log K$'s using a simple polynomial function. Table 5.1 lists the mineral hydrolysis and aqueous species dissociation reactions, along with the obtained $\log K$ values used in the models. P-T dependent parameters for the Debye-Huckel equation were calculated following Helgeson and Kirkham (1974), and were fitted to the relevant pressure and temperature range of the model using a third order polynomial fit. Density of water was calculated using the Perple_X program suite (Connolly and Pettrini, 2002) for a range of pressures and temperatures using the CORK equation of state of Holland and Powell (1991, 1998). A third order polynomial was introduced to the code to calculate water densities corresponding to the P-T conditions along the model grid.

5.5 Model parameters

One-dimensional grid

Most of the drill hole data in Icelandic hydrothermal systems come from the upper 2 km of the crust. In high-temperature fields, the lower thermal boundary layer may have temperatures in the range of 250 – 350 °C. As the model domain, the lower 1 km long one-dimensional, vertical section from a 2 km deep profile was selected. The temperature at the lower thermal boundary was taken as 300 °C and the pressure as 196 bar that corresponds to the hydrostatic pressure. Temperature and pressure were distributed from the bottom of the profile along the one-dimensional model grid assuming a temperature gradient of -100 °C/km and a hydrostatic pressure gradient of -98 bar/km (Fig. 5.3). The main petrologic character of distribution of basaltic rocks in Iceland is that the active volcanic zone consists of tholeiitic basalts while the flank zones consist of alkali basalts. Tholeiites are further classified into olivine-tholeiites and quartz-tholeiites. The composition of a representative ol-tholeiite from Reykjanes peninsula was selected as the initial unaltered rock for the model. Table 5.2 shows its chemical composition and calculated CIPW norms. Number of moles was calculated using the given weight percentages for each end member in all the minerals that form solid solutions. No thermodynamic data for glass is available, hence we used the CIPW norm as starting mode. The thermodynamic properties and mineral compositions of the basalts were used as initial mineral phases. For example, the CIPW norms for clinopyroxenes given in Table 5.2 yield a composition of ~70% diopside and ~30% hedenbergite. Thus Di70Hd30 pseudo compound was used as the initial cpx mineral phase. The volume of each primary mineral was calculated for the given weight percentages assuming only plagioclase, cpx, opx and olivine to be present. They were converted to volume percentages, and recalculated for 10% porosity, assuming the rock to have this porosity generated by fractures. The resulting mineral abundances were distributed along the model grid as the initial mineralogical composition of the basalt.

Table 5.1. Mineral and aqueous species reactions and their log*K*'s used in simulations.

Reaction	Log <i>K</i>					
	200°C	230°C	260°C	290°C	320°C	350°C
<i>Aqueous species</i>						
$\text{Al(OH)}_2^+ + 2\text{H}^+ = \text{Al}^{+3} + 2\text{H}_2\text{O}$	1.1686	0.6907	0.2351	-0.2051	-0.6263	-0.9999
$\text{Al(OH)}^{+2} + \text{H}^+ = \text{Al}^{+3} + \text{H}_2\text{O}$	3.5853	2.7593	1.9804	1.2321	0.5169	-0.1222
$\text{CaCl}^+ = \text{Ca}^{+2} + \text{Cl}^-$	-0.5085	-0.8417	-1.2174	-1.6535	-2.1819	-2.9203
$\text{CaCl}_2(\text{aq}) = \text{Ca}^{+2} + 2\text{Cl}^-$	-0.8577	-1.3899	-2.0139	-2.7638	-3.7054	-5.0818
$\text{FeCl}^+ = \text{Fe}^{+2} + \text{Cl}^-$	-1.0665	-1.3938	-1.7634	-2.1926	-2.7117	-3.4338
$\text{FeCl}_2(\text{aq}) = \text{Fe}^{+2} + 2\text{Cl}^-$	0.2244	-0.3726	-1.0538	-1.8546	-2.8385	-4.2394
$\text{HCl}(\text{aq}) = \text{H}^+ + \text{Cl}^-$	0.1464	-0.1368	-0.4796	-0.9061	-1.4745	-2.3981
$\text{HSiO}_3^- + \text{H}^+ = \text{SiO}_2(\text{aq}) + \text{H}_2\text{O}$	8.7908	8.8740	9.0237	9.2457	9.5601	10.0583
$\text{MgCl}^+ = \text{Mg}^{+2} + \text{Cl}^-$	-1.1136	-1.4720	-1.8745	-2.3377	-2.8934	-3.6593
$\text{NaCl}(\text{aq}) = \text{Na}^+ + \text{Cl}^-$	-0.0697	-0.2762	-0.5177	-0.8122	-1.1967	-1.8030
$\text{NaAlO}_2(\text{aq}) + 4\text{H}^+ = \text{Na}^+ + \text{Al}^{+3} + 2\text{H}_2\text{O}$	10.8653	9.4714	8.1775	6.9484	5.7721	4.6671
$\text{NaHSiO}_3(\text{aq}) + \text{H}^+ = \text{Na}^+ + \text{SiO}_2(\text{aq}) + \text{H}_2\text{O}$	7.6342	7.6643	7.7144	7.7722	7.8232	7.8295
$\text{H}^+ + \text{OH}^- = \text{H}_2\text{O}$	11.2310	11.1279	11.1040	11.1671	11.3390	11.7231
<i>Minerals</i>						
$\text{Albite} + 4\text{H}^+ = \text{Na}^+ + \text{Al}^{+3} + 3\text{SiO}_2(\text{aq}) + 2\text{H}_2\text{O}$	-2.7899	-3.3805	-3.9462	-4.5166	-5.1058	-5.7308
$\text{Anorthite} + 8\text{H}^+ = \text{Ca}^{+2} + 2\text{Al}^{+3} + 2\text{SiO}_2(\text{aq}) + 4\text{H}_2\text{O}$	3.5549	1.2794	-0.8571	-2.9170	-4.9196	-6.8183
$\text{Clinocllore} + 16\text{H}^+ = 5\text{Mg}^{+2} + 2.0\text{Al}^{+3} + 3.0\text{SiO}_2(\text{aq}) + 12.0\text{H}_2\text{O}$	22.2681	18.3970	14.8055	11.3550	7.9961	4.7640
$\text{Clinozoisite} + 13\text{H}^+ = 2\text{Ca}^{+2} + 3\text{Al}^{+3} + 3\text{SiO}_2(\text{aq}) + 7\text{H}_2\text{O}$	8.6209	5.1766	1.9426	-1.1820	-4.2282	-7.1353
$\text{Daphnite} + 16\text{H}^+ = 5\text{Fe}^{+2} + 2.0\text{Al}^{+3} + 3.0\text{SiO}_2(\text{aq}) + 12.0\text{H}_2\text{O}$	13.0772	9.6752	6.4838	3.3755	0.3058	-2.7094
$\text{Di70Hd30} + 4\text{H}^+ = \text{Ca}^{+2} + 0.7\text{Mg}^{+2} + 0.3\text{Fe}^{+2} + 2\text{SiO}_2(\text{aq}) + 2\text{H}_2\text{O}$	10.4545	9.4394	8.5031	7.6060	6.7192	5.7880
$\text{En70Fs30} + 4\text{H}^+ = 1.4\text{Mg}^{+2} + 0.6\text{Fe}^{+2} + 2\text{SiO}_2(\text{aq}) + 2\text{H}_2\text{O}$	9.7820	8.6208	7.5554	6.5443	5.5605	4.5598
$\text{Ferroactinolite} + 14\text{H}^+ = 2.0\text{Ca}^{+2} + 5\text{Fe}^{+2} + 2.0\text{Al}^{+3} + 8.0\text{SiO}_2(\text{aq}) + 8.0\text{H}_2\text{O}$	24.3264	21.3471	18.5780	15.8888	13.1750	10.2480
$\text{Fo70Fa30} + 4\text{H}^+ = 1.4\text{Mg}^{+2} + 0.6\text{Fe}^{+2} + \text{SiO}_2(\text{aq}) + 2\text{H}_2\text{O}$	12.6203	11.2800	10.0547	8.9027	7.7988	6.7178
$\text{Quartz} = \text{SiO}_2(\text{aq})$	-2.4516	-2.3054	-2.1746	-2.0592	-1.9628	-1.9026
$\text{Tremolite} + 14\text{H}^+ = 2.0\text{Ca}^{+2} + 5\text{Mg}^{+2} + 2.0\text{Al}^{+3} + 8.0\text{SiO}_2(\text{aq}) + 8.0\text{H}_2\text{O}$	31.8790	28.6290	25.6251	22.7469	19.8781	16.8531
$\text{Ab90An10} + 4.4\text{H}^+ = 0.90\text{Na}^+ + 0.10\text{Ca}^{+2} + 1.10\text{Al}^{+3} + 2.90\text{SiO}_2(\text{aq}) + 2.2\text{H}_2\text{O}$	-1.8869	-2.6928	-3.4572	-4.2120	-4.9745	-5.7541
$\text{Ab80An20} + 4.8\text{H}^+ = 0.80\text{Na}^+ + 0.20\text{Ca}^{+2} + 1.20\text{Al}^{+3} + 2.80\text{SiO}_2(\text{aq}) + 2.4\text{H}_2\text{O}$	-1.3001	-2.2682	-3.1842	-4.0831	-4.9826	-5.8859

Reaction	LogK					
	200°C	230°C	260°C	290°C	320°C	350°C
Ab70An30 + 5.2H ⁺ = 0.70Na ⁺ + 0.30Ca ⁺² + 1.30Al ⁺³ + 2.70SiO ₂ (aq) + 2.6H ₂ O	-0.6774	-1.8098	-2.8792	-3.9240	-4.9621	-5.9904
Ab60An40 + 5.6H ⁺ = 0.60Na ⁺ + 0.40Ca ⁺² + 1.40Al ⁺³ + 2.60SiO ₂ (aq) + 2.8H ₂ O	-0.0384	-1.3362	-2.5598	-3.7513	-4.9286	-6.0826
Ab50An50 + 6.0H ⁺ = 0.50Na ⁺ + 0.50Ca ⁺² + 1.50Al ⁺³ + 2.50SiO ₂ (aq) + 3.0H ₂ O	0.6017	-0.8614	-2.2394	-3.5776	-4.8942	-6.1739
Ab40An60 + 6.4H ⁺ = 0.40Na ⁺ + 0.60Ca ⁺² + 1.60Al ⁺³ + 2.40SiO ₂ (aq) + 3.2H ₂ O	1.2304	-0.3974	-1.9291	-3.4135	-4.8689	-6.2738
Ab30An70 + 6.8H ⁺ = 0.30Na ⁺ + 0.70Ca ⁺² + 1.70Al ⁺³ + 2.30SiO ₂ (aq) + 3.4H ₂ O	1.8374	0.0461	-1.6381	-3.2676	-4.8609	-6.3902
Ab20An80 + 7.2H ⁺ = 0.20Na ⁺ + 0.80Ca ⁺² + 1.80Al ⁺³ + 2.20SiO ₂ (aq) + 3.6H ₂ O	2.4161	0.4630	-1.3723	-3.1455	-4.8756	-6.5283
Ab10An90 + 7.6H ⁺ = 0.10Na ⁺ + 0.90Ca ⁺² + 1.90Al ⁺³ + 2.10SiO ₂ (aq) + 3.8H ₂ O	2.9681	0.8549	-1.1301	-3.0458	-4.9114	-6.6864
Da10Ch90 + 16H ⁺ = 4.5Mg ⁺² + 0.5Fe ⁺² + 2.0Al ⁺³ + 3.0SiO ₂ (aq) + 12.0H ₂ O	20.6705	16.8446	13.2917	9.8742	6.5430	3.3315
Da20Ch80 + 16H ⁺ = 4.0Mg ⁺² + 1.0Fe ⁺² + 2.0Al ⁺³ + 3.0SiO ₂ (aq) + 12.0H ₂ O	19.3976	15.6171	12.1027	8.7182	5.4148	2.2239
Da30Ch70 + 16H ⁺ = 3.5Mg ⁺² + 1.5Fe ⁺² + 2.0Al ⁺³ + 3.0SiO ₂ (aq) + 12.0H ₂ O	18.2652	14.5300	11.0542	7.7026	4.4270	1.2568
Da40Ch60 + 16H ⁺ = 3.0Mg ⁺² + 2.0Fe ⁺² + 2.0Al ⁺³ + 3.0SiO ₂ (aq) + 12.0H ₂ O	17.2373	13.5474	10.1103	6.7916	3.5439	0.3943
Da50Ch50 + 16H ⁺ = 2.5Mg ⁺² + 2.5Fe ⁺² + 2.0Al ⁺³ + 3.0SiO ₂ (aq) + 12.0H ₂ O	16.3001	12.6556	9.2571	5.9715	2.7516	-0.3772
Da60Ch40 + 16H ⁺ = 2.0Mg ⁺² + 3.0Fe ⁺² + 2.0Al ⁺³ + 3.0SiO ₂ (aq) + 12.0H ₂ O	15.4499	11.8509	8.4911	5.2385	2.0464	-1.0617
Da70Ch30 + 16H ⁺ = 1.5Mg ⁺² + 3.5Fe ⁺² + 2.0Al ⁺³ + 3.0SiO ₂ (aq) + 12.0H ₂ O	14.6906	11.1370	7.8159	4.5963	1.4321	-1.6552
Da80Ch20 + 16H ⁺ = 1.0Mg ⁺² + 4.0Fe ⁺² + 2.0Al ⁺³ + 3.0SiO ₂ (aq) + 12.0H ₂ O	14.0357	10.5275	7.2000	4.0587	0.9223	-2.1442
Da90Ch10 + 16H ⁺ = 0.5Mg ⁺² + 4.5Fe ⁺² + 2.0Al ⁺³ + 3.0SiO ₂ (aq) + 12.0H ₂ O	13.5213	10.0586	6.8149	3.6615	0.5531	-2.4927
Ft10Tr90 + 14H ⁺ = 2.0Ca ⁺² + 4.5Mg ⁺² + 0.5Fe ⁺² + 2.0Al ⁺³ + 8.0SiO ₂ (aq) + 8.0H ₂ O	30.9825	27.7596	24.7792	21.9199	19.0666	16.0514
Ft20Tr80 + 14H ⁺ = 2.0Ca ⁺² + 4.0Mg ⁺² + 1.0Fe ⁺² + 2.0Al ⁺³ + 8.0SiO ₂ (aq) + 8.0H ₂ O	30.1511	26.9553	23.9983	21.1580	18.3202	15.3148
Ft30Tr70 + 14H ⁺ = 2.0Ca ⁺² + 3.5Mg ⁺² + 1.5Fe ⁺² + 2.0Al ⁺³ + 8.0SiO ₂ (aq) + 8.0H ₂ O	29.3479	26.1792	23.2457	20.4242	17.6019	14.6063
Ft40Tr60 + 14H ⁺ = 2.0Ca ⁺² + 3.0Mg ⁺² + 2.0Fe ⁺² + 2.0Al ⁺³ + 8.0SiO ₂ (aq) + 8.0H ₂ O	28.5657	25.4240	22.5140	19.7114	16.9046	13.9188
Ft50Tr50 + 14H ⁺ = 2.0Ca ⁺² + 2.5Mg ⁺² + 2.5Fe ⁺² + 2.0Al ⁺³ + 8.0SiO ₂ (aq) + 8.0H ₂ O	27.8017	24.6870	21.8005	19.0168	16.2256	13.2495
Ft60Tr40 + 14H ⁺ = 2.0Ca ⁺² + 2.0Mg ⁺² + 3.0Fe ⁺² + 2.0Al ⁺³ + 8.0SiO ₂ (aq) + 8.0H ₂ O	27.0551	23.9676	21.1046	18.3397	15.5640	12.5978
Ft70Tr30 + 14H ⁺ = 2.0Ca ⁺² + 1.5Mg ⁺² + 3.5Fe ⁺² + 2.0Al ⁺³ + 8.0SiO ₂ (aq) + 8.0H ₂ O	26.3269	23.2664	20.4268	17.6809	14.9207	11.9642
Ft80Tr20 + 14H ⁺ = 2.0Ca ⁺² + 1.0Mg ⁺² + 4.0Fe ⁺² + 2.0Al ⁺³ + 8.0SiO ₂ (aq) + 8.0H ₂ O	25.6196	22.5862	19.7701	17.0431	14.2983	11.3517
Ft90Tr10 + 14H ⁺ = 2.0Ca ⁺² + 0.5Mg ⁺² + 4.5Fe ⁺² + 2.0Al ⁺³ + 8.0SiO ₂ (aq) + 8.0H ₂ O	24.9405	21.9341	19.1415	16.4334	13.7042	10.7673

*Pseudo compounds have been named indicating mole percent of each endmember. Ab: albite, An: anorthite, Da: daphnite, Ch: clinocllore
Ft: ferroactinolite, Tr: tremolite, Fo: forsterite, Fa: fayalite, Di: diopside, Hd: hedenbergite, En: enstatite, Fs: ferrosilite*

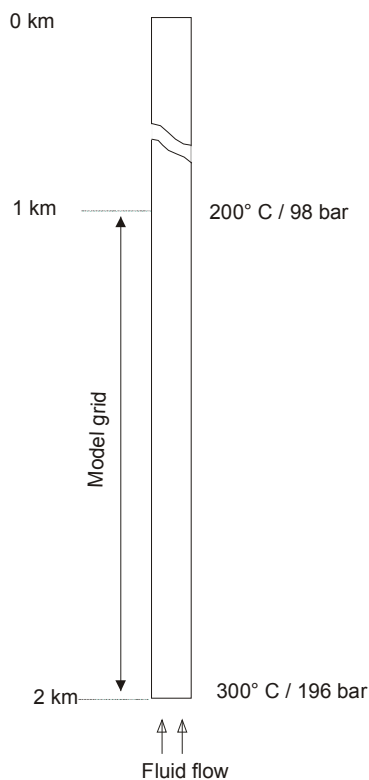


Figure 5.3. Schematic diagram of the model grid showing the depth profile, P-T conditions at the boundaries and flow direction.

The reactive surface area of primary minerals was assumed to be 5 m^2 per m^3 of rock, and that of secondary minerals to be 0.01 m^2 per m^3 of rock. The flow rate of migrating fluids was set to $150.0 \text{ m}^3 \text{ m}^{-2} \text{ yr}^{-1}$. The longitudinal dispersivity was taken as 10 m making the combined dispersion/diffusion coefficient for all solute species $3.17 \times 10^{-6} \text{ m}^2 \text{ s}^{-1}$. These flow parameters yield a reasonable grid Peclet number which is necessary for the numerical stability in simulations. A value of $1.0 \times 10^{-10} \text{ mole m}^{-2} \text{ s}^{-1}$ was assigned as the dissolution/precipitation rate for all mineral phases at all temperatures considered in the model. This value is likely fast enough to adequately describe the reaction rates at high temperatures. It is recognized that the choice of these parameters is quite arbitrary, since not much is known about actual mineral surface areas in these fractured rocks. See discussions of results for a discussion of consequences of the parameter choices.

Initial fluid composition

Geothermal fluid in Svartsengi is rich in Na and Cl indicating its sea water origin while Krafla geothermal water points to a meteoric origin (Table 5.3). These two different fluid compositions were used in fluid-rock interaction simulations to see the effect of salinity on hydrothermal alteration. For the chemical speciation calculations, the equilibrium geochemical speciation model SOLUB (Roselle and Baumgartner, 1986) was used. Fluid compositions were calculated

for the P-T conditions at the two ends of the model grid taking the total aqueous species concentrations given in Table 5.3.

Table 5.2. Average chemical composition of tholeiitic basalt from Reykjanes Peninsula, Iceland.

	Wt %
SiO ₂	48.03
TiO ₂	1.24
Al ₂ O ₃	15.68
Fe ₂ O ₃	1.20
FeO	9.07
MnO	0.18
MgO	9.82
CaO	12.54
Na ₂ O	1.79
K ₂ O	0.10
P ₂ O ₅	0.09
Sum	99.74
<i>Modes (wt%)</i>	
Qtz	
Or	0.59
Ab	15.15
An	34.45
Di	14.74
Hd	7.34
En	7.13
Fs	4.07
Fo	7.36
Fa	4.63

From: Jakobsson et al., (1978)

Table 5.3. Chemical composition of fluids from Svartsengi and Krafla geothermal fields, Iceland.

Component	Concentration (ppm)	
	<i>Svartsengi</i> ^(a)	<i>Krafla</i> ^(b)
Na	8037	193.9
K	1245	29
Ca	1343	2.54
Mg	1.62	0.064
Al	0.07	0.12
SiO ₂	534	575.5
Cl	17010	28
pH	7.53	9.02

^(a) ref. Ragnarsdóttir and Walther (1984)
^(b) ref. Sveinbjörnsdóttir (1992)

For the speciation calculations it was assumed that the fluid was in equilibrium with the secondary minerals. Hence in SOLUB calculations quartz, tremolite and daphnite were used to constrain the equilibrium concentrations of $\text{SiO}_2(\text{aq})$, Mg^{+2} and Fe^{+2} respectively, while Na^+ , Ca^{+2} , Al^{+3} and Cl^- were constrained by the total concentration given in Table 5.3. The resulting aqueous species concentrations were used as initial input for the transport calculations. 1DREACT calculates the aqueous species concentrations using mass and charge balance equations, and mineral equilibrium constraints. Table 5.4 gives a summary of the initial fluid composition and the constraints for each aqueous species used in simulations.

Table 5.4. Initial fluid compositions at the model boundaries, and the constraints used to buffer the aqueous species concentrations.

Component	Concentration (mol/kg w)				Constraint
	Fluid inlet T = 300 °C		Fluid outlet T = 200 °C		
	Fluid I	Fluid II	Fluid I	Fluid II	
H^+	7.130×10^{-05}	1.108×10^{-09}	1.680×10^{-05}	1.075×10^{-09}	Charge balance
$\text{Al}(\text{OH})_2^+$	2.565×10^{-06}	4.448×10^{-06}	2.551×10^{-06}	4.448×10^{-06}	Total Al concentration
Ca^{+2}	1.870×10^{-02}	6.400×10^{-05}	3.010×10^{-02}	6.487×10^{-05}	Tremolite equilibrium
Cl^-	3.408×10^{-01}	7.646×10^{-04}	4.273×10^{-01}	7.843×10^{-04}	Total Cl concentration
Fe^{+2}	2.932×10^{-06}	1.764×10^{-18}	1.048×10^{-06}	2.502×10^{-17}	Total Fe concentration
Mg^{+2}	9.908×10^{-03}	5.010×10^{-16}	2.311×10^{-02}	1.105×10^{-13}	Clinocllore equilibrium
Na^+	2.534×10^{-01}	7.422×10^{-03}	3.097×10^{-01}	7.831×10^{-03}	Total Na concentration
$\text{SiO}_2(\text{aq})$	8.725×10^{-03}	8.725×10^{-03}	3.534×10^{-03}	3.534×10^{-03}	Quartz equilibrium

Fluid I : Saline water from Svartsengi
Fluid II : Fresh water from Krafla

5.6 Results and discussion

Reactions taking place at the higher temperature part of the alteration profile (Fig. 5.2) between the discharging geothermal fluids and basalts were modeled. Both fresh water and saline water compositions, from Krafla and Svartsengi geothermal fields respectively, were tested in different simulations. Intense fluid-rock interaction starts as the fluid enters the model domain. Existing minerals dissolve while new secondary phases precipitate. Since the fluid is far from equilibrium with the starting minerals of the model, and due to the higher temperature gradient most of the mineral dissolution-precipitation reactions take place in the vicinity of the fluid inlet. This leads to significant increase or decrease in porosity. Since the reactions are largely affected by fluid composition, pattern of mineral dissolution-precipitation is significantly different when fresh water and saline water compositions are used in the simulations. Figure 5.4 shows the porosity changes along the model grid with time after reactions with the two types of fluid. Porosity

decreases with time along the whole model domain due to precipitation of secondary phases when saline fluids are present. This porosity change is comparatively large at the fluid inlet due to the increased reactions brought about by the inlet fluid composition calculated to be in disequilibrium with the minerals. Reactions with a fresh water composition result in a slightly different trend. There is an increase of the porosity with time close to the fluid inlet due to primary mineral dissolution. Further down stream this pattern reverses, and as in the previous case porosity decreases with the precipitation of secondary phases. Since all other parameters in both simulations were kept identical, the effect of fluid composition on the fluid-rock reactions in this system can be seen in this example.

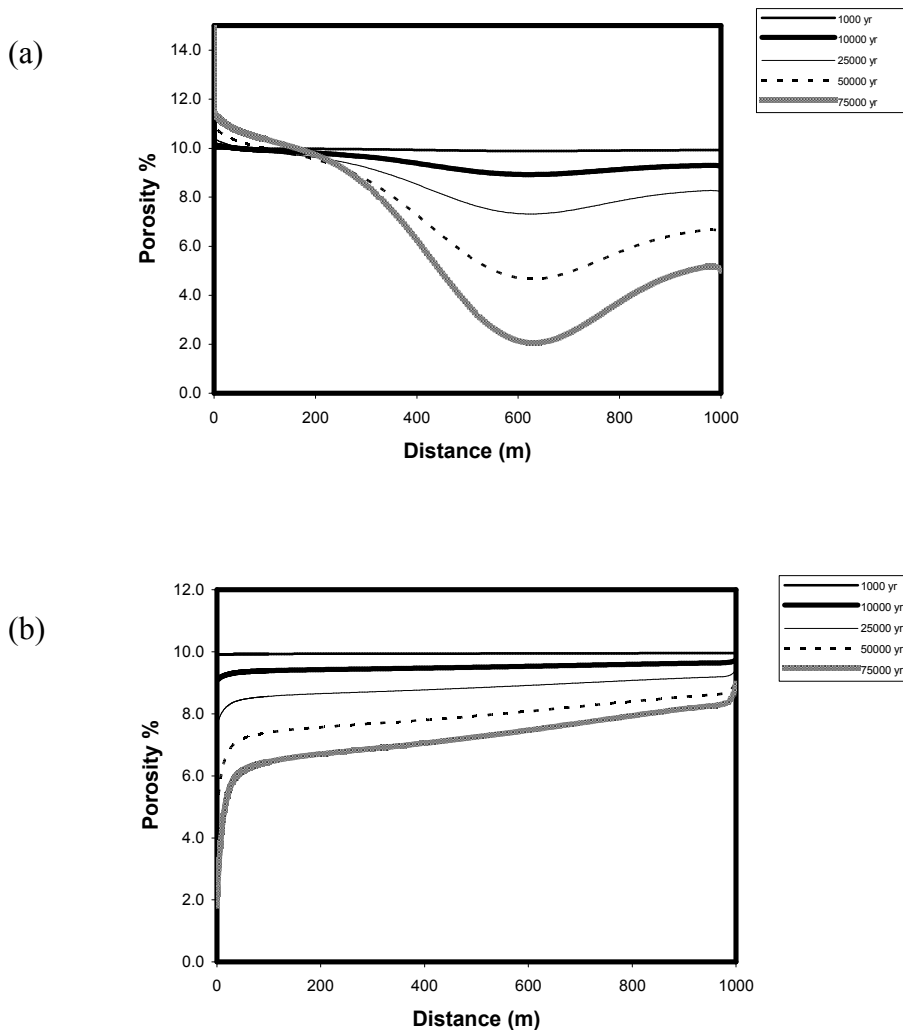


Figure 5.4. Evolution of porosity along the model grid after fluid-rock interactions with (a) fresh water composition from Krafla (b) sea water composition from Svartsengi.

Changes of the initial mineral volumes due to the reactions with both types of fluid after 75000 years with initial mineral volumes are shown in Figure 5.5. They show different dissolution-

precipitation patterns along the model grid. Most of the pseudo compounds of solid solutions considered in the simulations form as the secondary phases in different proportions and patterns.

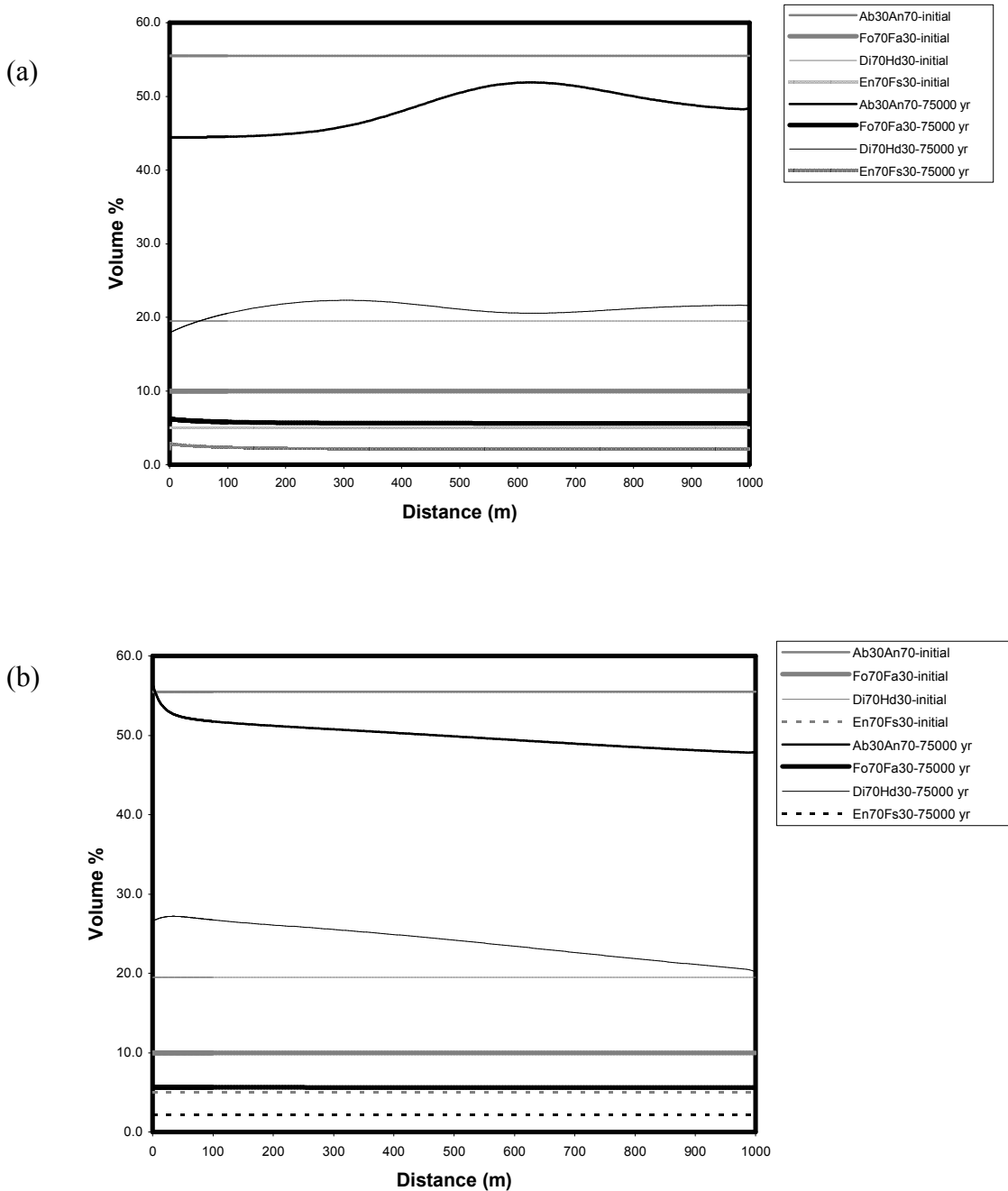


Figure 5.5. Change of initial mineral volumes with time after fluid-rock interactions with (a) fresh water composition from Krafla (b) sea water composition from Svartsengi.

As shown in Figures 5.6-5.8, their distribution along the model domain is largely affected by the fluid composition. More amphiboles precipitate towards higher temperatures. Lower temperature regions of the model are dominated by chlorite. The coprecipitation of several pseudo compounds

of each solid solution is an artifact of the use of pseudocomponents. Since all these pseudocomponents are supersaturated along the model domain, they precipitate.

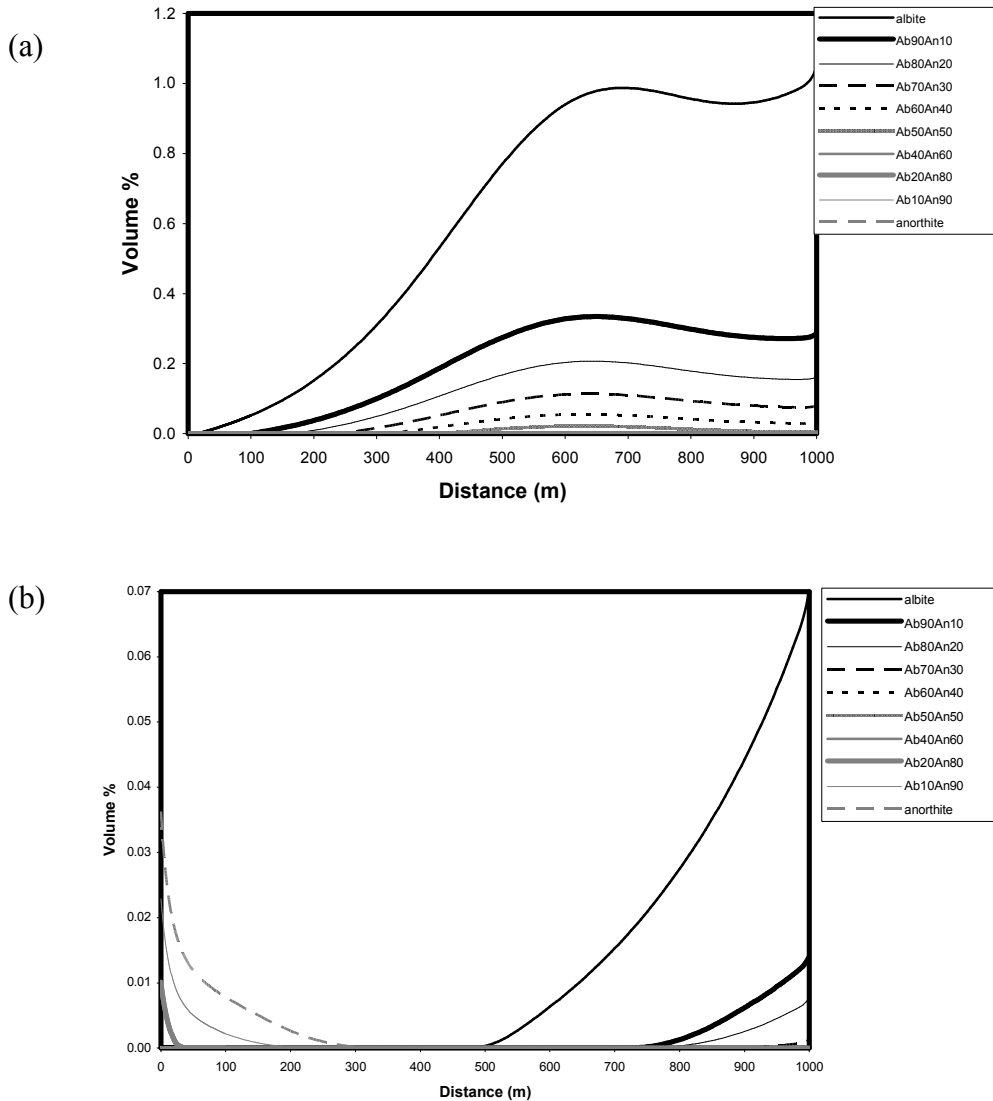


Figure 5.6. Distribution of plagioclase pseudo compounds after 75000 years. (a) fresh water composition from Krafla (b) sea water composition from Svartsengi. Initial Ab30An70 phase has not been plotted.

In nature, subtle differences in nucleation and growth kinetics will typically prevent more than one solid-solution composition from precipitating, though slight composition variations can be found. Hence the results obtained point towards the need of kinetic data that span the whole range of solid solution compositions. Similar conclusions were reached for diffusion limited crystallization of minerals in melts (e.g. Lasaga, 1982). Experimental investigations (Kirkpatrick et al., 1979) and theoretical considerations (Lasaga, 1982) on plagioclase crystal growth have shown that each intermediate phase of the solid solution has a different growth rate.

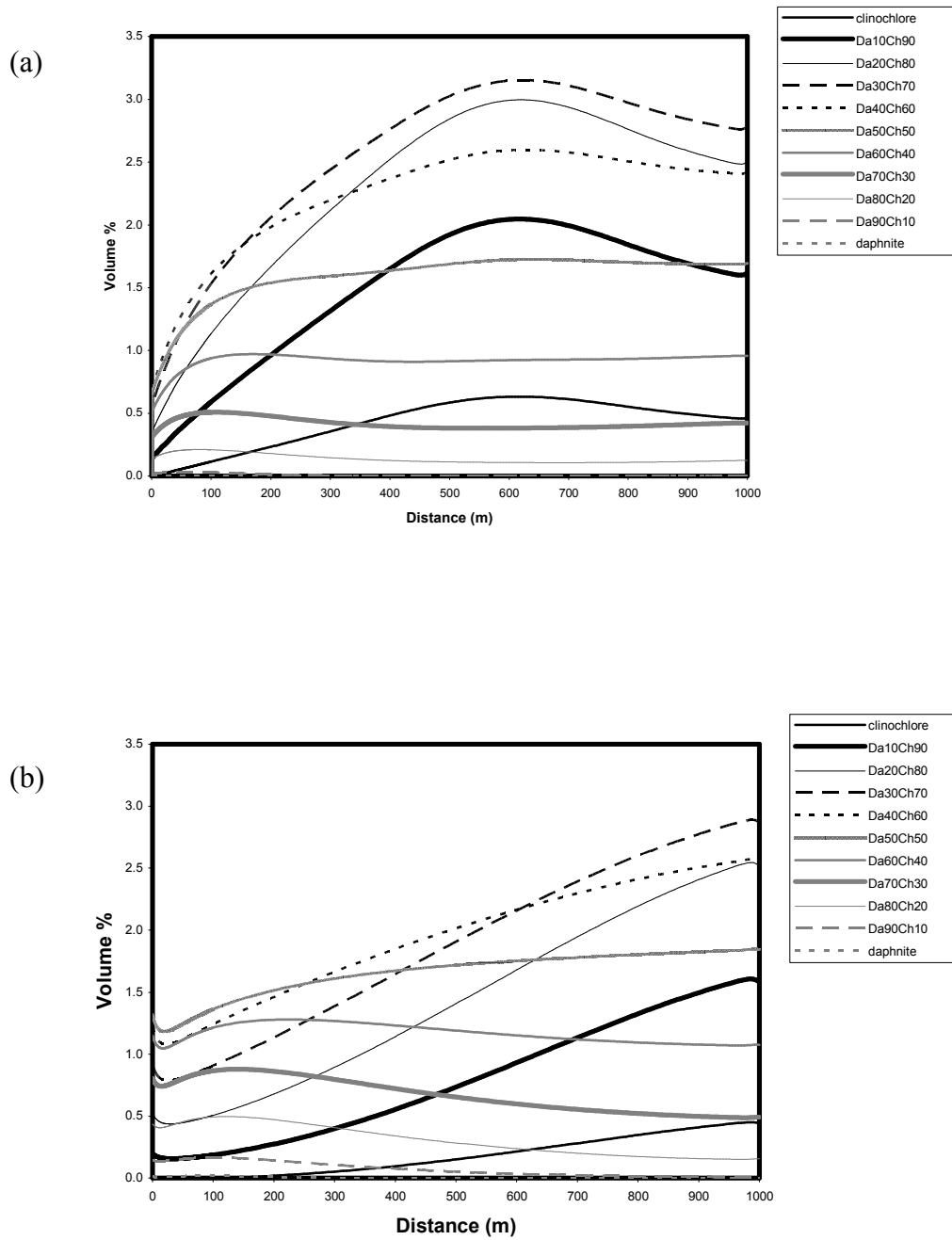


Figure 5.7. Distribution of chlorite pseudo compounds after 75000 years. (a) fresh water composition from Krafla (b) sea water composition from Svartsengi.

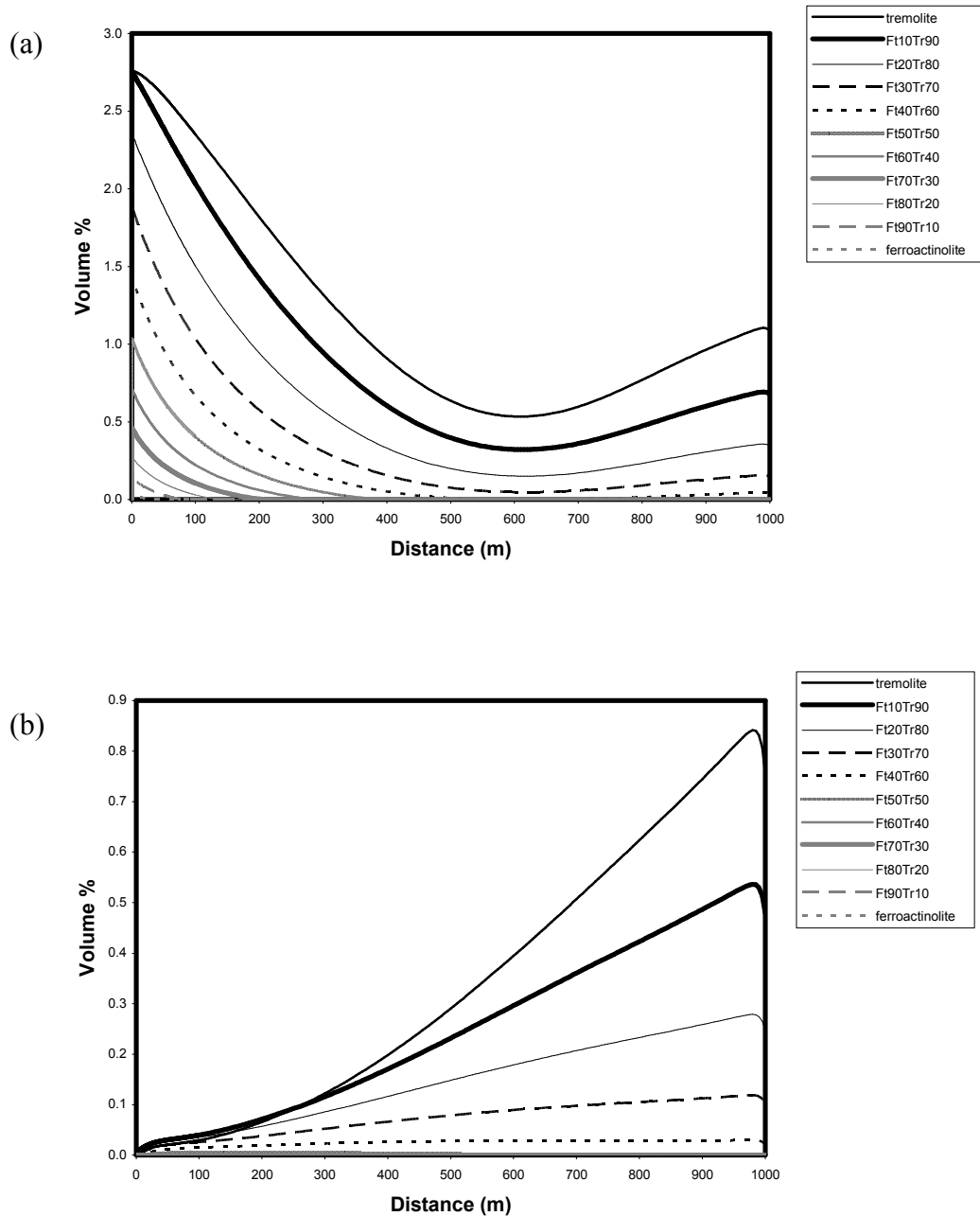


Figure 5.8. Distribution of amphibole pseudo compounds after 75000 years. (a) fresh water composition from Krafla (b) sea water composition from Svartsengi.

Figure 5.9 shows one of the compositional relations between an altered basalt from Svartsengi and a fresh tholeiite. Labrodoritic composition of initial plagioclase moves toward more albitic compositions. Simulation results show that Ab30An70 pseudo compound phase which was used as starting plagioclase composition is replaced by other albite-rich pseudo compounds (Figs. 5.5 & 5.6). Minor amounts of clinozoisite and quartz also precipitate. Since epidote was not included

in calculations (because Fe^{3+} was not considered in the model), clinozoisite is obtained, rather than epidote.

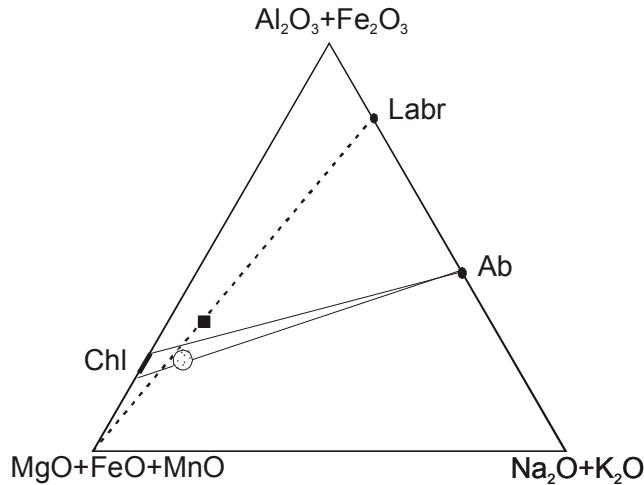


Figure 5.9. Ternary oxide diagram showing composition relations of primary and secondary minerals. Broken line is the tie-line for primary assemblage. Filled square indicates the composition of unaltered tholeiite and hatched circle indicates that of an altered rock (from: Ragnarsdóttir and Walther, 1984).

As shown by Sveinbjörnsdóttir (1992), compositions of geothermal minerals from Karfla and Svartsengi are markedly different as affected by different fluid compositions. Fluid-rock interaction calculations show that the composition of the secondary amphiboles resulted by the reactions with geothermal fluid from Karfla spans a wide range (Fig. 5.8a). All the pseudo compounds used in tremolite-ferroactinolite binary solid precipitated. Reactions with the saline fluid from Svartsengi do not form the whole compositional range. However all pseudo compounds of chlorite-daphnite binary solid solution precipitate in both instances. Because amphiboles and chlorites form more complex solid solutions in natural systems rather than the simple binary solutions used here, direct correspondence of the simulation results to the laboratory analyses of the altered basalts is not possible. Albitic compositions for secondary plagioclases resulted by fluid-rock interaction calculations are in agreement with analytical results.

Formation of Fe- and Mg-rich phases is reflected in the aqueous species concentration profiles (Figs. 5.10 & 5.11). Fe and Mg are taken up by the precipitating phases, decreasing their concentrations in the aqueous phase. There is a slight increase in Ca in the solution probably due to the dissolution of anorthite-rich plagioclase. Na and Cl in both fluids are conserved and there are no significant pH changes.

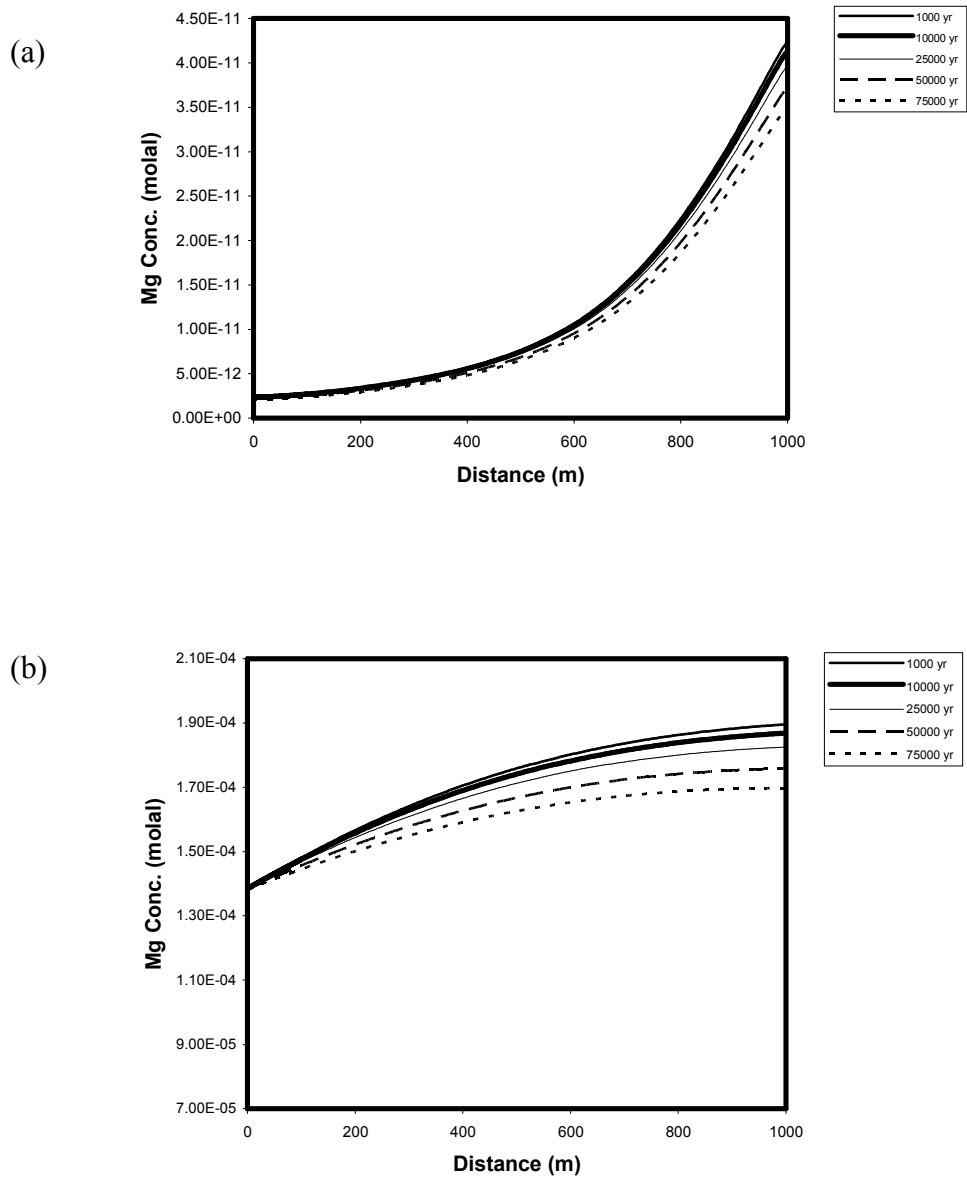


Figure 5.10. Change of total Mg concentration with time (a) fresh water composition from Krafla (b) sea water composition from Svartsengi.

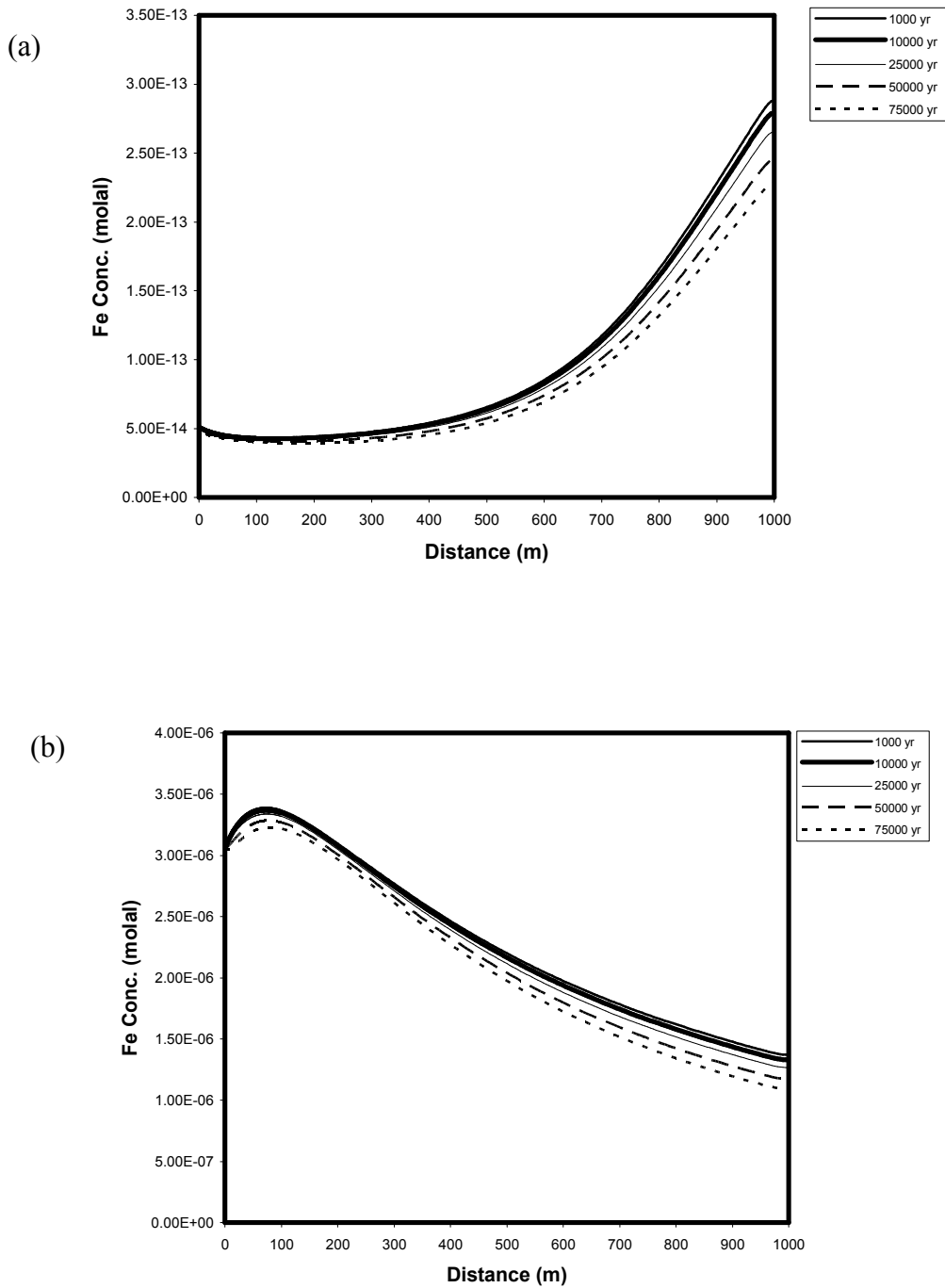


Figure 5.11. Change of total Fe concentration with time (a) fresh water composition from Krafla (b) sea water composition from Svartsengi.

5.7 Conclusions

Hydrothermal alteration of basalts in high-temperature areas in Iceland was modeled. Fresh water and saline water compositions of the geothermal fluids reacting with basalts result in different mineral abundances along the model grid. However the alteration mineralogy remains the same

to a large extent which is in agreement with field observations. Since solid solutions are abundant in hydrothermal systems, they were included in reactive transport calculations using the pseudo compound approach (see Chapter 3). Simplifications were made choosing only binary solid solutions, and no iron redox reactions were included. Hence the results are clearly preliminary, nevertheless the success obtained is encouraging. It is emphasized that pseudo compound approach for solid solutions in modeling reactive transport in hydrothermal systems is promising. A rigorous treatment needs reliable thermodynamic and kinetic data for all intermediate compositions of the solid solutions.

References

- Arnórsson, S., 1978. Major element chemistry of geothermal sea-water at Reykjanes and Svartsengi, Iceland. *Min. Mag.*, 42, 209-220.
- Arnórsson, S., 1995. Geothermal systems in Iceland: Structure and conceptual models – I. High-temperature areas. *Geothermics*, 24, 561-602.
- Baumgartner, L.P., Ferry, J.M., 1991. A model for coupled fluid-flow and mixed-volatile mineral reactions with applications to regional metamorphism. *Contrib. Mineral. Petrol.* (106), 273-285.
- Connolly, J.A.D., 1990. Multivariable phase diagrams: An algorithm based on generalized thermodynamics. *Am. J. Sci.*, 290, 666-718.
- Connolly, J.A.D. and Petriani, K., 2002. An automated strategy for calculation of phase diagram sections and retrieval of rock properties as a function of physical conditions. *J. Met. Geol.* 20, 697-708.
- Exley, R.A., 1980. Electron microprobe studies of Iceland research drilling project high-temperature hydrothermal mineral chemistry. *J. Geophys. Res.* 87, 6547-6557.
- Franzson, H., 1983. The Svartsengi high-temperature field: subsurface geology and alteration. *Trans. Geotherm. Resour. Counc.* 7, 141-145.
- Helgeson, H.C., Kirkham, D.H., Flowers, G.C., 1981. Theoretical prediction of the thermodynamic behaviour of aqueous electrolytes at high pressures and temperatures: IV. Calculation of activity coefficients and osmotic coefficients and apparent molal and standard and relative molal properties to 600°C and 5kb. *Am. J. Sci.*, 281, 1249-1493.
- Holland, T. and Powell, R., 1991. A compensated-Reidlich-Kwong (CORK) equation for volumes and fugacities of CO₂ and H₂O in the range 1 bar to 50 kbar and 100-16000C. *Contrib. Mineral. Petrol.* 109, 265-273.
- Holland, T.J.B., and Powell, R., 1998. An internally-consistent thermodynamic data set for phases of petrological interest. *J. Met. Geol.* 16, 309-343.
- Jacoby, W.R., Girardin, N., 1980. The evolution of the lithosphere at the southeast flank of Reykjanes Ridge from surface wave data. *J. Geophys.*, 47, 271-277.

- Kirkpatrick, R.J., Klein, L., Uhlmann, D.R. and Hays, J.F., 1979. Rates and processes of crystal growth in the system anorthite-albite. *J. Geophys. Res.* 84 (B7), 3671-3676.
- Kristmannsdóttir, H., 1975. Hydrothermal alteration of basaltic rocks in Icelandic geothermal areas. In: 2nd UN Symp. Develop. Use of Geothermal resources. San Francisco, CA, 1, 441-445.
- Kristmannsdóttir, H., 1978. Alteration of basaltic rock by hydrothermal activity at 100-300⁰C. In: Mortland, M.M., Farmer, V.C. ed, *Intl. Clay Conference 1978*. Elsevier, Amsterdam, 359-367.
- Kristmannsdóttir, H., 1983. Chemical evidence from Icelandic geothermal systems as compared to submerged geothermal systems. In: Rona, P.A., Bostrom, K., Laubier, L., Smith, K.L.Jr., eds., *Hydrothermal processes at seafloor spreading centers*. Plenum Press, New York, 291-320.
- Lasaga, A.C., 1982. Toward a master equation in crystal growth. *Am. J. Sci.* 282, 1264-1288.
- Lasaga, A.C., 1998. *Kinetic theory in the earth sciences*. Princeton University Press, p728.
- Meyer, P.S., Sigurdsson, H., Schilling, J., 1985. Petrological and geochemical variations along Iceland's neovolcanic zones. *J. Geophys. Res.* 90 (B12), 10043-10072.
- Mehegan, J.M., Robinson, P.T., Delaney, J.R. 1980. Secondary mineralisation and hydrothermal alteration in the Reydarfjordur drill core, eastern Iceland. *J. Geophys. Res.* 87, 6511-6524.
- Ólafsson, J. and Riley, J.P., 1978. Geochemical studies on the thermal brine from Reykjanes (Iceland). *Chem. Geology*, 21, 219-237.
- Pálmason, G., 1974. Heat flow and hydrothermal activity in Iceland. In: Kristjánsson, L., ed., *Geodynamics of Iceland and the North Atlantic area*. D. Reidel, Dordrecht, 297-306.
- Ragnarsdóttir, K.V., Walther, J.V., 1984. Description and interpretation of the composition of fluid and alteration mineralogy in the geothermal system at Svartsengi, Iceland. *Geochim. Cosmochim. Acta* 48, 1535-1553.
- Roselle, G.T. and Baumgartner, L.P., 1995. Experimental determination of anorthite solubility and calcium speciation in supercritical chloride solutions at 2 kb from 400 to 600⁰C. *Geochim. Cosmochim. Acta* 59, 1539-1549.
- Steeffel, C.I., 1993. *1DREACT User Manual*.
- Steeffel, C.I., Lasaga, A.C., 1994. A coupled model for transport of multiple chemical species and kinetic precipitation/dissolution reactions with applications to reactive flow in single phase hydrothermal system. *Am. J. Sci.* 294, 529-592.
- Sveinbjörnsdóttir, Á.E., 1992. Composition of geothermal minerals from saline and dilute fluids – Krafla and Reykjanes, Iceland. *Lithos* 27, 301-315.

Application of Reactive Fluid Transport Modeling to Groundwater Contaminant Treatment: Excess Nitrate Removal by Pyrite Oxidation

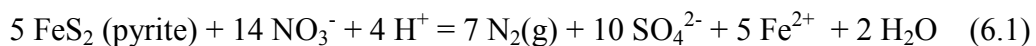
ABSTRACT

The use of permeable reactive barriers has been shown to be an efficient method to remove groundwater contaminants in some cases. For such installations to be cost effective, it is important to predict their performance prior to implementation. Reactive fluid transport models can provide valuable information in this regard. The case of a nitrate removal from groundwater was modeled by reducing it to nitrogen through oxidation by an iron-bearing minerals, pyrite. A one-dimensional reactive transport code, 1DREACT (Steeffel, 1993) was used to simulate the pyrite oxidation reaction taking place in a hypothetical denitrification wall. Simulations show that nitrate concentration in groundwater can be lowered by a factor of 3 within a week. Although sulphate concentration increases due to dissolution of pyrite, it can be maintained to values below the recommended level for drinking water. Fluid flow rate and pyrite reactive surface area are the major factors that control the efficiency of nitrate removal.

6.1 Introduction

Numerous studies have demonstrated the potential of reactive fluid transport models to assess the physical, geochemical and biological processes involved in contaminated groundwater transport and treatment (Baveye and Valocchi, 1989; Hunter et al., 1998; Rosqvist and Destouni, 2000; MacQuarrie and Sudicky, 2001; Liedl and Ptak, 2003). They couple the hydrological properties of the subsurface with geochemical reactions occurring between the fluid and the minerals of the aquifers. Hence proposed scenarios of groundwater remediation can be cost efficiently modeled, in order to design optimized rectifying measures for contaminated aquifers. The necessity for such exercises is becoming significant with the ever increasing threats for groundwater quality. Industries, agriculture and waste disposal are the main contributors for groundwater contamination. The types of pollutants are wide and varied, and so is their behaviour in aquifers.

Among many groundwater contaminants, nitrate (NO_3^-) is a common solute that propagates into aquifers from agricultural lands as it is a major component in fertilizers and manure. Also domestic and urban sewage are responsible for extensive release of nitrate into groundwater systems. Although nitrate is found naturally at moderate concentrations in most of the aquatic systems, its enrichment in subsurface water bodies poses a threat to drinking water supplies due to its carcinogenic nature. The maximum admissible NO_3^- concentration in drinking water is 50 mg/l while the recommended level is 25 mg/l according to World Health Organization (WHO) standards (Appelo and Postma, 1999). In aquatic systems nitrate does not form any mineral that can be precipitated. Nor is it adsorbed onto any aquifer material as far as it is known today. Therefore the only means for its removal from groundwater is by reduction. Several methods are being employed in nitrate removal from groundwater. Organic matter has the potential for reducing NO_3^- to N_2 in a bacterially catalyzed reaction. This denitrification process is commonly used in field scale implementations (eg. Schipper and others, 2004). Jørgensen and others (2004) give a detailed account on the natural denitrification by bacteria mediated reactions in saturated aquifers consisting of organic-rich clays. The second process of NO_3^- reduction in aquifers is by ferrous to ferric oxidation of iron. A typical source of Fe^{2+} in an aquifer can be Fe(II)-bearing minerals (Appelo and Postma, 1999). A well known process of NO_3^- removal is by pyrite oxidation (Postma and others, 1991) and will be the subject of the following discussion. This involves oxidation of both Fe(II) and sulfur and can be described by the following reaction (Appelo and Postma, 1999).



It is apparent that introducing pyrite into the flow path might help lower the NO_3^- concentration by reducing it to nitrogen. Postma et al., (1991) have illustrated the expected increase in SO_4^{2-} and Fe^{2+} with field examples. However if SO_4^{2-} and Fe^{2+} concentrations in the solution can still be maintained below the maximum admissible levels for drinking water, this process may successfully be employed for NO_3^- removal by installing a pyrite-bearing zone across the flow path in the form of a denitrification wall. Permeable reactive barriers have been in use and reported to be efficiently removing NO_3^- from groundwater, in some cases in excess of 90% (Robertson and Cherry, 1995; Robertson and others, 2000; Schipper and Vojvodic-Vokovic, 2000). This chapter discusses the simulation of the above geochemical reaction using the reactive fluid transport code 1DREACT (Steeffel, 1993) in order to design an optimum condition under which the NO_3^- concentration could be minimized. The reaction in Eqn. 6.1 is best known to take place under anoxic conditions and particularly mediated by microbial activity.

However the simulations will be carried out considering only the geochemical aspects as provisions to accommodate microbial reactions are not available in the present code.

6.2 Reactive fluid transport modeling

The coupled reaction and transport equation for the conservation of mass of a solute species can be expressed as (Steefel, 1993),

$$\frac{\partial(\phi C_j)}{\partial t} + \nabla \cdot (u C_j - D \nabla C_j) = R_j \quad (j = 1, \dots, N_c) \quad (6.2)$$

where ϕ is the porosity, C_j is the total concentration of the j^{th} species, u is the Darcian fluid flux, D is the combined dispersion/diffusion coefficient and R_j is the total rate of the heterogeneous mineral-fluid reactions affecting the concentration of j^{th} species in solution. N_c is the total number of components. The total concentration is the sum of concentrations of species in the fluid phase for each component j . Equation 6.2, when implemented with a suitable numerical algorithm, provides a tool to describe many of the processes that involve chemical reactions and fluid transport in geologic media.

Fluid-rock interaction simulations are carried out using the one dimensional multicomponent reactive fluid transport code, 1DREACT (Steefel, 1993; Steefel and Lasaga, 1994) which is based on an integrated finite difference formulation of Eqn. 6.2 that solves for aqueous species concentrations, calculates mineral precipitation/dissolution rates, saturation states, and mineral volumes for systems with diffusion and infiltration. It requires a thermodynamic database, initial fluid composition, mineral abundances and the physical transport parameters of the flow system.

6.3 Model parameters

A 2 m long one-dimensional section of a hypothetical aquifer which consists of sandy-clayey material was taken as the model domain. Mineral volume percentages were assigned (25% kaolinite, 40% quartz) such that a high porosity (35%) is allowed. A permeable reactive barrier zone consisting of pyrite (15%) together with other aquifer material (10% kaolinite, 40% quartz) was introduced into the flow path (Fig. 6.1). The grid was discretized into 1 cm segments for transport calculations. The initial composition of the water entering the model domain was taken to be in the range of solute concentrations of the influent solution used by Jørgensen and others (2004) in their experiments on nitrate removal by organic matter (Table 6.1). Additionally a concentration of NO_3^- (70 mg/l) was introduced. Initial chemical speciation of the water

flowing into the pyrite barrier zone and that of the water leaving it after reacting with pyrite were calculated using the geochemical model PHREEQC (Parkhurst and Appelo, 1999). These compositions were used to initialize the model grid as shown in Table 6.2 for the transport calculations with 1DREACT.

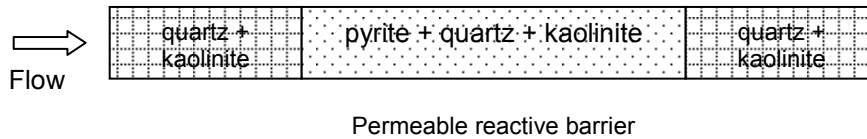


Figure 6.1. One-dimensional model grid. Pyrite-bearing zone acts as a permeable reactive barrier.

Table 6.1. Chemical composition of the groundwater used in simulations.

Component	Concentration (ppm)
Na	60
K	5
Ca	95
Mg	23
NO ₃ ⁻	70*
SO ₄ ⁻²	20
HCO ₃ ⁻	380
pH	7.8
* introduced concentration	

Dispersivity of the medium was taken as 0.03 m while a value of $1 \times 10^{-9} \text{ m}^2\text{s}^{-1}$ was assigned for the diffusion coefficient for all solute species. Dissolution/precipitation rates of minerals and the activation energies used in the simulations are given in Table 6.3. For those minerals where experimental data are not available the reaction rates were assumed to be $1 \times 10^{-9} \text{ moles m}^{-2}\text{s}^{-1}$ at 25 °C. The thermodynamic database used by 1DREACT for mineral-fluid reaction calculations contains logK's of hydrolysis reactions of minerals and aqueous complexes. LogK of the reaction in Eqn. 6.1 as written for one mole of reacting pyrite at 25 °C was calculated (211.027) using SUPCRT92 (Johnson et al., 1992)

and included in the thermodynamic database. Simulations were carried out for different mineral surface area, length of the reactive barrier zone and flow rates.

Table 6.2. Initial fluid compositions distributed along the model grid, and the constraints used to buffer the aqueous species concentrations.

Component	Concentration (mol/kg w)		
	Fluid inlet	Fluid outlet	Constraint
H ⁺	1.747 × 10 ⁻⁰⁸	8.445 × 10 ⁻⁰⁹	Charge balance
Al(OH) ₄ ⁻	1.000 × 10 ⁻¹²	1.900 × 10 ⁻⁰⁷	Total Al concentration
Ca ⁺²	2.167 × 10 ⁻⁰³	2.035 × 10 ⁻⁰³	Total Ca concentration
Fe ⁺²	1.000 × 10 ⁻¹²	1.874 × 10 ⁻⁰⁴	Total Fe concentration
HCO ₃ ⁻	7.238 × 10 ⁻⁰³	7.095 × 10 ⁻⁰³	Total C concentration
K ⁺	1.279 × 10 ⁻⁰⁴	1.275 × 10 ⁻⁰⁴	Total K concentration
Mg ⁺²	8.734 × 10 ⁻⁰⁴	8.192 × 10 ⁻⁰⁴	Total Mg concentration
Na ⁺	2.601 × 10 ⁻⁰³	2.595 × 10 ⁻⁰³	Total Na concentration
NO ₃ ⁻	1.130 × 10 ⁻⁰³	1.000 × 10 ⁻¹⁰	Total N(V) concentration
SO ₄ ⁻²	1.633 × 10 ⁻⁰⁴	8.011 × 10 ⁻⁰⁴	Total S(VI) concentration
SiO ₂ (aq)	1.000 × 10 ⁻⁰⁵	1.000 × 10 ⁻⁰⁵	Total SiO ₂ concentration
N ₂ (g)	1.000 × 10 ⁻¹⁵	1.000 × 10 ⁻¹⁰	Total N(III) concentration

Table 6.3. Reaction rates and activation energies of minerals used in simulations.

Mineral	Reaction rate at 25°C (mol/m ² /s)	Activation energy (kcal/mol)	Comments
Calcite	1.0000 × 10 ⁻⁰⁹	15.0	Assumed value
Gibbsite	3.5481 × 10 ⁻¹²	15.0	Data from Lasaga (1998)
Gypsum	1.0000 × 10 ⁻⁰⁹	15.0	Assumed value
Kaolinite	5.2480 × 10 ⁻¹⁴	16.0	Data from Lasaga (1998)
Pyrite	1.0000 × 10 ⁻⁰⁹	15.0	Assumed value
Quartz	4.0738 × 10 ⁻¹⁴	17.0	Data from Lasaga (1998)

6.4 Results and discussion

Since the reaction in Eqn. 6.1 is known to take place under anoxic conditions, reactive fluid flow modeling was carried out in the saturated zone of the aquifer. Figure 6.2 shows the change in NO₃⁻ concentration along the model grid after one week. When an average groundwater flow rate of 150 m yr⁻¹ and a 2.0 m long pyrite zone with silt-sized particles

were used, the system approached the steady state in one week. NO_3^- concentration was lowered to about 20 ppm in the effluent solution, which is a significant decrease from the initial ~ 70 ppm (70 mg/l). With higher flow rates the system approaches steady state in one week, but the decrease in NO_3^- concentration is small (Fig. 6.3).

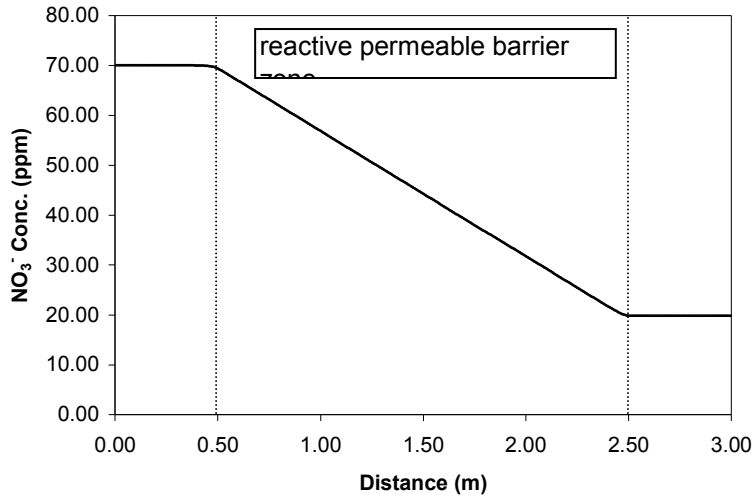


Figure 6.2. Change of NO_3^- concentration along the model grid when a flow rate of 150 m yr^{-1} is used.

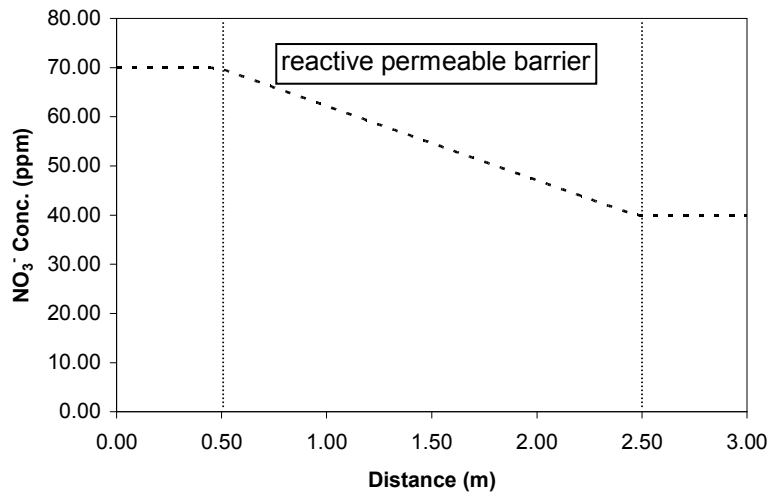


Figure 6.3. Change of NO_3^- concentration along the model grid when a flow rate of 250 m yr^{-1} is used.

Change of SO_4^{-2} concentration along the grid is shown in Figure 6.4. It can be observed that SO_4^{-2} concentration in the effluent has almost the inverse relation to NO_3^- concentration as 2.8 moles of NO_3^- are consumed to produce 2 moles of SO_4^{-2} . Since Ca^{+2} in the water is continuously being removed by precipitation of minor amount of calcite (Fig. 6.5), SO_4^{-2} remains in the aqueous phase due to unavailability of cations to form a precipitate. However, the steady state concentration of SO_4^{-2} , as shown in Figure 6.4, is 63 ppm which is reasonable and clearly below the maximum permissible level for drinking water (250 mg/l according to WHO standards). Major concentration changes in aqueous species after passing the denitrification wall can be observed in NO_3^- , SO_4^{-2} , Ca^{+2} , HCO_3^- and Fe^{+2} (Fig. 6.6). Slight decrease in pH (Fig. 6.7) can be attributed to the addition of H^+ by the reaction between Ca^{+2} and HCO_3^- to form calcite.

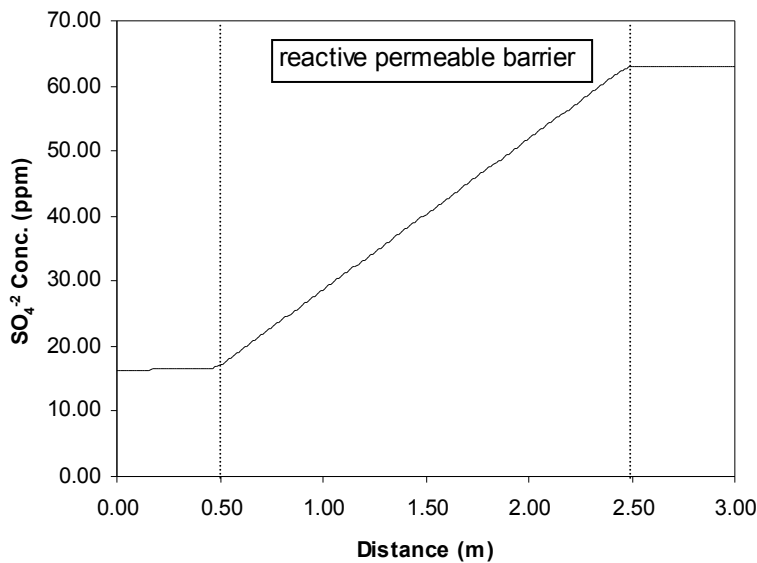


Figure 6.4. Change of SO_4^{-2} concentration along the model grid.

Reactive surface areas of minerals control the kinetics of mineral-fluid interactions. Therefore tests were carried out changing the pyrite reactive surface areas in order to determine their influence on NO_3^- removal. However, mineral reactive surface areas are not well known (Steeffel and Van Cappellen, 1990). Effective reactive surface area can be much less than that of experimentally estimated values as constrained by the connectivity of pore spaces. Assuming fine sand to silt sized spherical grains, surface areas of pyrite were approximated to be in the range of 300 - 700 m^2 per 1 m^3 of the medium. Figure 6.8 shows the effect of pyrite reactive surface area on the efficiency of NO_3^- removal. As expected, larger reactive surface areas, hence finer particles lowered the NO_3^-

concentration significantly. Similar effect can be observed if the length of the pyrite zone is increased for a fixed mineral surface area.

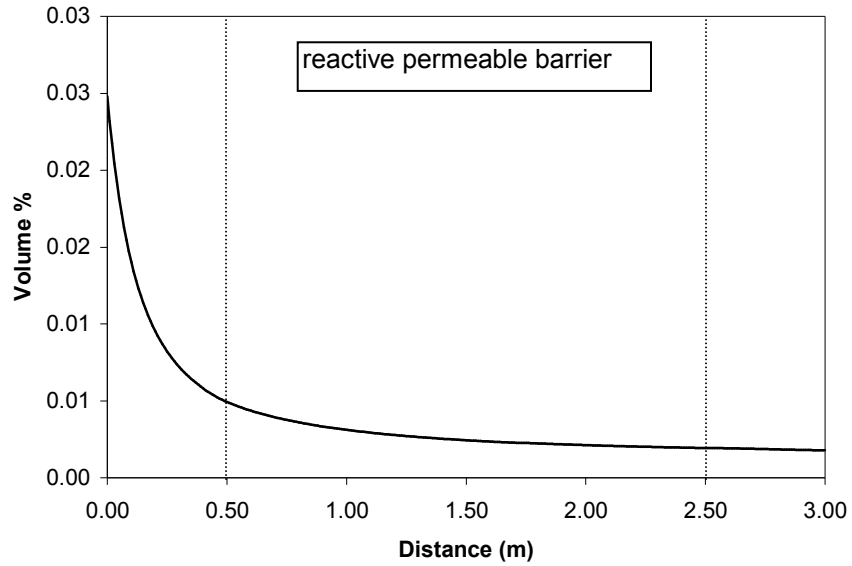


Figure 6.5. Calcite precipitation due to fluid-rock interaction.

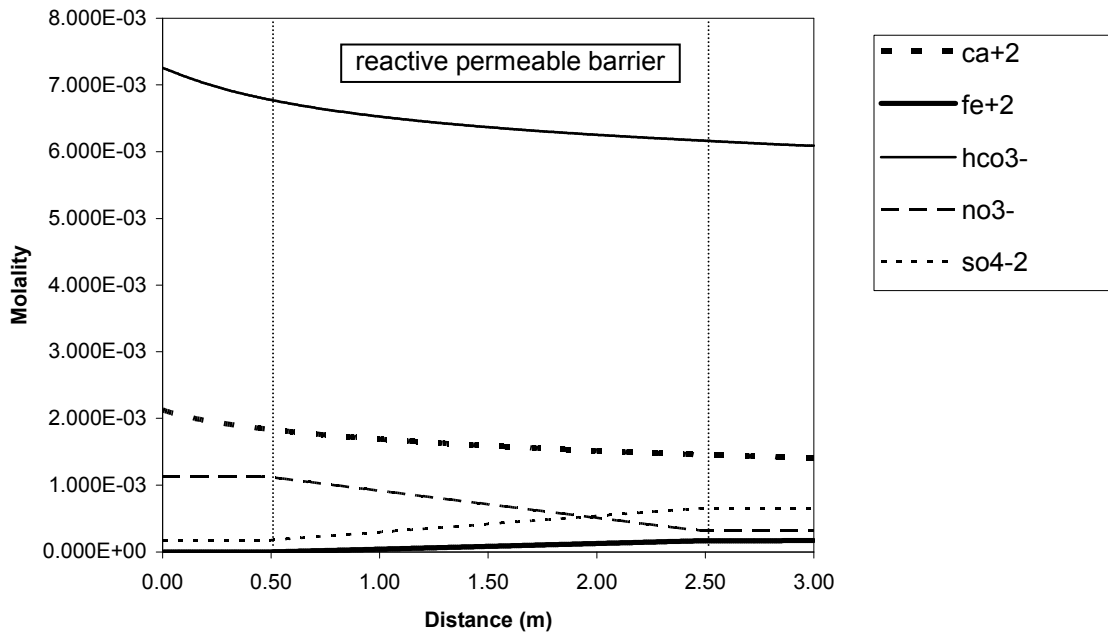


Figure 6.6. Aqueous species concentrations along the model grid.

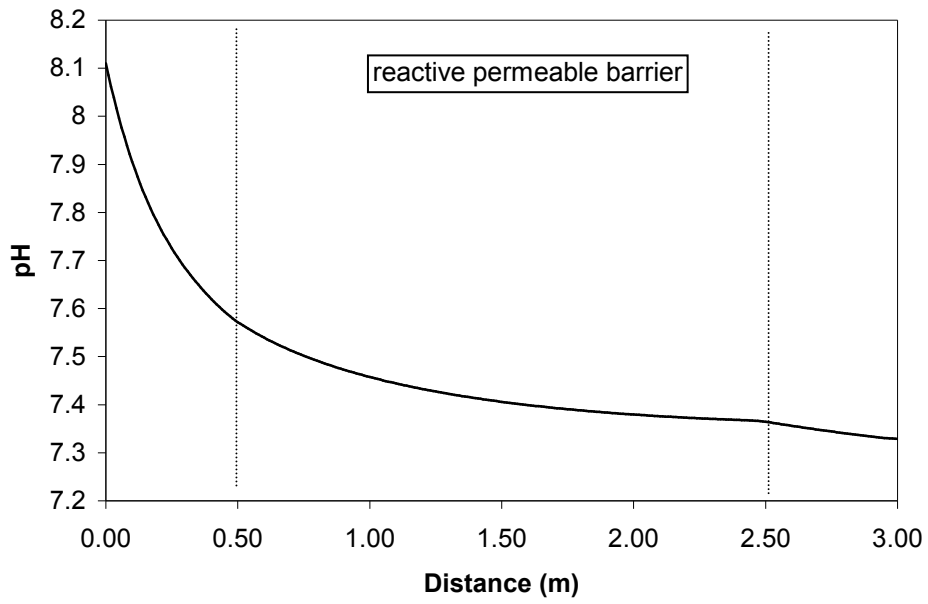


Figure 6.7. Change of pH along the model grid.

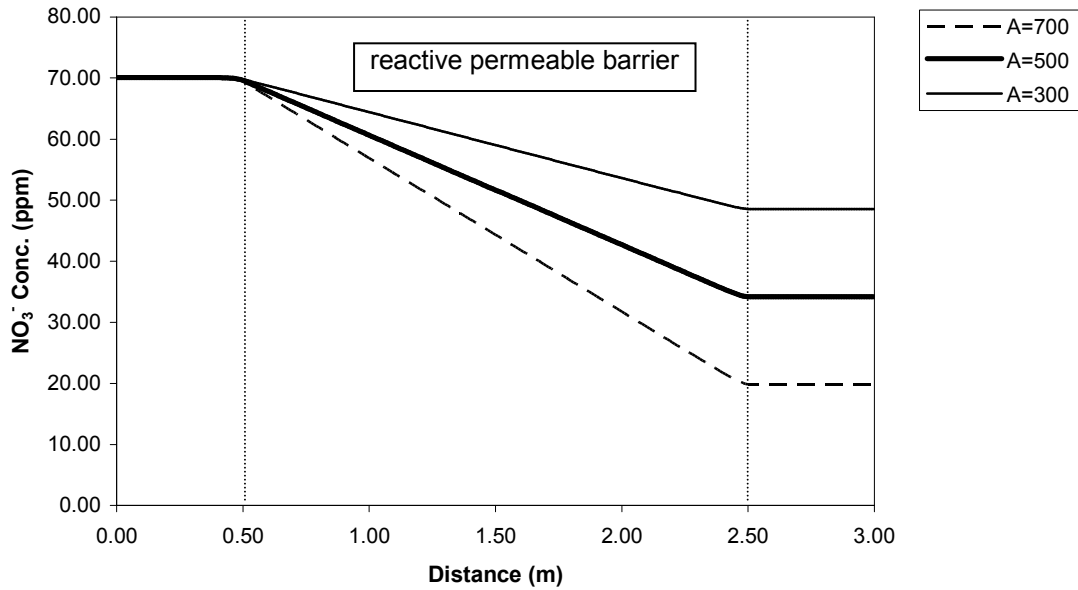


Figure 6.8. Effect of pyrite reactive surface area on NO₃⁻ removal.

6.5 Conclusion

Reactive fluid transport calculations have simulated the reduction of NO_3^- to $\text{N}_2(\text{g})$ by pyrite oxidation. Since this process takes place under anaerobic conditions, modeling was carried out in a subsurface environment using a permeable reactive barrier consisting of pyrite and sand. It is predicted that this setup is viable. Tests with different reactive surface areas and flow rates show the kinetic control on NO_3^- removal capacity. Flow rate was taken as a variable in simulations to show its effect on NO_3^- removal. However in groundwater environments it is dependent on the natural conditions, and can be considered as constant over short distances and short time periods. Therefore when pyrite-bearing permeable reactive barriers are installed in the groundwater flow paths in aquifers, efficiency of denitrification is controlled by the reactive surface area of pyrite and the length of the reacting zone. Increase in SO_4^{2-} concentration due to dissolution of pyrite can be maintained below the permissible levels for drinking water.

References

- Appelo, C.A.J. and Postma, D., 1999. *Geochemistry, Groundwater and Pollution*. A.A. Balkema, Rotterdam, 536pp.
- Bayeve, P. and Valocchi, A., 1989. An evaluation of mathematical models of the transport of biologically reacting solutes in saturated soils and aquifers. *Water Resour. Res.* 25(6), 1413–1421.
- Hunter, K.S., Wang, Y., Van Cappellen, P., 1998. Kinetic modeling of microbially driven redox chemistry of subsurface environments: coupling transport, microbial metabolism and geochemistry. *J. Hydrol.* 209, 53–80.
- Johnson, J.W., Oelkers, E.H. and Helgeson, H.C., 1992. SUPCRT92: A software package for calculating the standard molal thermodynamic properties of minerals, gases, aqueous species, and reactions from 1 to 5000 bars and 0 to 1000 degrees C. *Computers & Geosciences*, 18(7), 899-947.
- Jørgensen, P.R., Urup, J., Helstrup, T., Jensen, M.B., Eiland, F. and Vinther, F.P., 2004. Transport and reduction of nitrate in clayey till underneath forest and arable land. *J. Contam. Hydrol.* 73, 207– 226.
- Lasaga, A.C., 1998. *Kinetic theory in the earth sciences*. Princeton University Press. 728pp.
- Liedl, R. and Ptak, T., 2003. Modelling of diffusion-limited retardation of contaminants in hydraulically and lithologically nonuniform media. *J. Contam. Hydrol.* 66, 239–259.

- MacQuarrie, K.T.B. and Sudicky, E.A., 2001. Multicomponent simulation of wastewater-derived nitrogen and carbon in shallow unconfined aquifers I. Model formulation and performance. *J. Contam. Hydrol.* 47, 53–84.
- Parkhurst, D.L. and Appelo, C.A.J., 1999. User's guide to PHREEQC (Version 2) - A computer program for speciation, batch-reaction, one-dimensional transport, and inverse geochemical calculations. USGS Water-Resources Investigations Report 99-4259, 312pp.
- Postma, D., Boesen, C., Kristiansen, H. and Larsen, F., 1991. Nitrate reduction in an unconfined sandy aquifer: Water chemistry, reduction processes, and geochemical modeling. *Water Resour. Res.* 27, 2027-2045.
- Robertson, W.D. and Cherry, J.A., 1995. In situ denitrification of septic-system nitrate using reactive porous media barriers: field trials. *Ground Water* 33, 99– 111.
- Robertson, W.D., Blowes, D.W., Ptacek, C.J. and Cherry, J.A., 2000. Long-term of in situ reactive barriers for nitrate remediation. *Ground Water* 38, 689– 695.
- Rosqvist, H. and Destouni G., 2000. Solute transport through preferential pathways in municipal solid waste. *J. Contam. Hydrol.* 46, 39–60.
- Schipper, L.A., Vojvodic-Vukovic, M., 2000. Rates of nitrate removal from groundwater and denitrification in a constructed denitrification wall. *Ecol. Eng.* 14, 269– 278.
- Schipper, L.A., Barkle, G.F., Hadfield, J.C., Vojvodic-Vukovic, M. and Burgess, C.P., 2004. Hydraulic constraints on the performance of a groundwater denitrification wall for nitrate removal from shallow groundwater. *J. Contam. Hydrol.* 69, 263– 279.
- Steeffel, C.I., 1993. 1DREACT User Manual.
- Steeffel, C.I., Van Cappellen, P., 1990. A new kinetic approach to modeling water-rock interaction: the role of nucleation, precursors, and Ostwald ripening. *Geochim. Cosmochim. Acta* 54, 2657-2677.